Klaus Dieter Kupper

A Low-Cost LoRa-Based Sensor Node for River Level Monitoring

Itajaí (SC), março de 2026

UNIVERSIDADE DO VALE DO ITAJAÍ
CURSO DE MESTRADO ACADÊMICO EM
COMPUTAÇÃO APLICADA

A LOW-COST LORA-BASED SENSOR NODE FOR RIVER LEVEL MONITORING

por

Klaus Dieter Kupper

Dissertação apresentada como requisito parcial à obtenção do grau de Mestre em Computação Aplicada.
Orientador: Prof. Jordan Passinato Sausen, Dr.

Itajaí (SC), março de 2026

“A Low-Cost LoRa-Based Sensor Node for River Level Monitoring”

“Klaus Dieter Kupper”

Esta Dissertação foi julgada adequada para obtenção do Título de Mestre em Computação Aplicada, Área de Concentração Computação Aplicada, e aprovada em sua forma final pelo Programa de Mestrado Acadêmico em Computação Aplicada da Universidade do Vale do Itajaí – UNIVALI.

Prof. Jordan Passinato Sausen, Dr.
Coordenador do Curso de Mestrado em Computação Aplicada

Apresentado perante a Banca Examinadora composta pelos Professores:

Profº. Dr. Jordan Passinato Sausen

Orientador (a)

Profº. Dr. Cesar Albenes Zeferino (UNIVALI)

Membro

Profº. Dr. Felipe Viel (UNIVALI)

Membro

Profº. Dr. Carlos Henrique Barriquello (UFSM)

Membro externo

Itajaí-SC, 26 de março de 2026.

This work is dedicated to my family, my colleagues, my teachers and my friends.

ACKNOWLEDGEMENTS

I would like to express my sincere gratitude to my advisor, Prof. Dr. Jordan Passinato Sausen, for his guidance, patience, and continuous support throughout this research. His expertise and insights were invaluable in shaping this work.

I extend my thanks to Prof. Dr. Mauricio de Campos, Prof. Dr. Felipe Viel, Prof. Dr. Carlos Henrique Barriquello, Prof. Dr. Julio Cesar Frantz, and Prof. Dr. Cesar Albenes Zeferino for their constructive feedback and suggestions.

I am grateful to the Universidade do Vale do Itajaí (UNIVALI) and the Masters in Applied Computing program for providing the academic environment and resources necessary for this research. Special thanks to the FAPESC-funded IoTec LAB for the LoRaWAN infrastructure that made the field deployment possible.

To my family, for their unconditional love, support, and encouragement throughout this journey. Your belief in me has been my greatest motivation. A special thanks to Cecilia for her dedicated help with proofreading and reviewing this work.

To my colleagues and friends, for the shared experiences, discussions, and support that made this academic journey more enriching and enjoyable.

Finally, I thank all who, directly or indirectly, contributed to the completion of this work.

"In the middle of every difficulty lies opportunity." (Albert Einstein)

RESUMO

A Low-Cost LoRa-Based Sensor Node for River Level Monitoring

Klaus Dieter Kupper

março / 2026

Orientador: Prof. Dr. Jordan Passinato Sausen
Área de Concentração: Computação Aplicada
Linha de Pesquisa: Sistemas Embarcados e Distribuídos
Palavras-chave: Rede de Sensores Sem Fio; LoRaWAN; Monitoramento do Nível de Rios; LiDAR; Sensores Ultrassônicos; ISO 4373; Monitoramento de Enchentes.
Número de páginas: 117

Este trabalho propõe e valida experimentalmente um nó sensor de baixo custo baseado em LoRa para o monitoramento escalável do nível de rios, apresentando a primeira comparação direta entre sensores ultrassônicos e LiDAR por meio de um pipeline completo de validação Lab-to-Bridge. Cinco sensores de distância sem contato foram avaliados em condições controladas e reais, no âmbito de uma iniciativa regional de monitoramento ambiental no Vale do Itajaí, Brasil. O estudo introduz três contribuições originais: (1) a identificação de um Efeito de Integração de Linha, pelo qual a geometria de feixe largo de um LiDAR alcança estabilidade de medição 8× superior à de um feixe pontual sobre superfícies aquáticas dinâmicas; (2) a primeira quantificação do impacto da radiação solar ambiente sobre medições LiDAR de baixo custo sobre água, revelando que a resiliência à luz solar depende do projeto óptico do sensor e não é uma limitação inerente ao LiDAR; e (3) a validação empírica de que a turbidez da água melhora a precisão do LiDAR, confirmando que condições de cheia favorecem o desempenho do monitoramento óptico. Duas configurações de sensores alcançaram conformidade com a Classe de Desempenho 3 da ISO 4373:2022 durante implantação em campo sob condições chuvosas e ensolaradas. A arquitetura de nó validada e o framework metodológico replicável apoiam a expansão de redes distribuídas de sensoriamento ambiental em afluentes com escassez de dados.

ABSTRACT

A Low-Cost LoRa-Based Sensor Node for River Level Monitoring

Klaus Dieter Kupper

março / 2026

Advisor: Prof. Dr. Jordan Passinato Sausen
Area of Concentration: Applied Computer Science
Research Line: Sistemas Embarcados e Distribuídos
Keywords: Wireless Sensor Network; LoRaWAN; River Level Monitoring; LiDAR; Ultrasonic Sensors; ISO 4373; Flood Monitoring.
Number of pages: 117

This work proposes and experimentally validates a low-cost LoRa-based sensor node for scalable river level monitoring, providing the first side-by-side comparison of ultrasonic and LiDAR sensors through a complete Lab-to-Bridge validation pipeline. Five non-contact distance sensors were evaluated under controlled and real-world conditions within a regional environmental monitoring initiative in the Vale do Itajaí, Brazil. The study introduces three novel contributions to the field: (1) the identification of a Line Integration Effect, whereby a wide line-beam LiDAR geometry achieves 8× greater measurement stability than a conventional spot-beam over dynamic water surfaces; (2) the first quantification of the impact of ambient solar radiation on low-cost LiDAR measurements over water, revealing that sunlight resilience is determined by sensor optical design rather than being an inherent LiDAR limitation; and (3) empirical validation that water turbidity improves LiDAR accuracy, confirming that flood conditions enhance rather than degrade optical monitoring performance. Two sensor configurations achieved ISO 4373:2022 Performance Class 3 compliance during field deployment under both rainy and sunny conditions. The validated node architecture and replicable methodological framework support the expansion of distributed environmental sensing networks in data-scarce tributaries.

LIST OF FIGURES

LIST OF TABLES

LIST OF ABBREVIATIONS AND ACRONYMS

ADR	Adaptive Data Rate
AI	Artificial Intelligence
API	Application Programming Interface
CSS	Chirp Spread Spectrum
GPIO	General Purpose Input/Output
I2C	Inter-Integrated Circuit
IoT	Internet of Things
IP67	Ingress Protection Rating 67
LiDAR	Light Detection and Ranging
LoRa	Long Range
LoRaWAN	Long Range Wide Area Network
MAC	Medium Access Control
MAE	Mean Absolute Error
MQTT	Message Queuing Telemetry Transport
OTAA	Over-The-Air Activation
PMU	Power Management Unit
RADAR	Radio Detection and Ranging
REST	Representational State Transfer
RMSE	Root Mean Square Error
SPAD	Single-Photon Avalanche Diode
TOF	Time Of Flight
TTN	The Things Network
UART	Universal Asynchronous Receiver-Transmitter
UAV	Unmanned Aerial Vehicle
WSN	Wireless Sensor Network

CONTENTS

1 INTRODUCTION

Floods, particularly flash floods, are among the most impactful natural disasters worldwide, causing substantial economic losses, infrastructure damage, and fatalities (Jonkman, 2005; Santos; Tornquist; Marimon, 2014). These events are characterized by their sudden onset and rapid development, often occurring at the outlet of small catchments in response to intense localized rainfall, with response times of only a few hours (Borga et al., 2014). Compounding the issue, climate change is intensifying the global hydrological cycle, leading to an increase in the frequency and severity of extreme weather events, including floods (Hall et al., 2014). This reinforces the need for improved flood monitoring, risk management strategies and alert systems to safeguard communities.

Flash floods and debris flows often escape conventional hydrometeorological monitoring due to their spatial and temporal unpredictability (Borga et al., 2014). Accurate and real-time data collection becomes essential to calibrate hydrological and hydrodynamic models such as rainfall–runoff systems (Lin et al., 2020), flood discharge and water supply volumes (Lo et al., 2015) which serve as the foundation for effective early warning systems (Iqbal et al., 2021). In addition to instrumental data, combining systematic flood observations with historical and documentary records has been highlighted as a valuable approach to better understand long-term flood regime dynamics, including the detection of flood-rich and flood-poor periods influenced by natural variability (Hall et al., 2014).

However, monitoring natural disasters presents substantial technical challenges. The vast scales involved, coupled with harsh environmental conditions and the need for real-time data, demand robust, cost-effective, and scalable technological solutions (Chen et al., 2013). In this context, Wireless Sensor Networks (WSNs) have emerged as a promising tool, offering significant advantages in terms of deployment flexibility, rapid response capabilities, and affordability compared to traditional monitoring infrastructures (Yellampalli, 2021). WSNs can enable spatially distributed sampling and continuous data collection, within the constraints of node power budgets, which are critical for disaster monitoring applications (Pule; Yahya; Chuma, 2017).

To further enhance WSN capabilities in remote and large-scale environments, Low Power Wide Area Networks (LPWAN) like LoRaWAN have gained prominence (Ferreira; Silvério; Viana, 2023). LoRaWAN is specifically designed for transmitting small amounts of data over long distances with extremely low power consumption, enabling sensor nodes to operate autonomously for up to 10 years (Pule; Yahya; Chuma, 2017). This makes it particularly suitable for hydrological monitoring systems in regions with limited infrastructure (Chen et al., 2013).

Among the sensing technologies available for water level measurement, non-contact methods are preferred for river monitoring due to their resistance to debris, biofouling, and mechanical wear. The principal non-contact alternatives are ultrasonic sensors, which measure the time of flight of acoustic pulses; LiDAR sensors, which use pulsed or modulated near-infrared laser light; and radar sensors, which operate at microwave frequencies. Ultrasonic and LiDAR sensors are available at low cost and are compatible with the power and data constraints of LoRaWAN nodes, whereas radar sensors remain substantially more expensive and are typically used in professional-grade hydrometric stations. This work therefore focuses on the comparative evaluation of ultrasonic and LiDAR technologies for integration into low-cost WSN nodes.

1.1 PROBLEM STATEMENT AND JUSTIFICATION

Two specific aspects of low-cost LiDAR behavior over water surfaces remain unquantified in the literature. First, although strong background light such as direct sunlight is a recognized noise source in SPAD-based LiDAR systems (Villa et al., 2021), and low-cost LiDAR experiments have been deliberately conducted indoors to avoid sunlight interference (Hama et al., 2022), no published work quantifies the effect of ambient solar radiation on LiDAR measurements over water, where the inherently low reflectivity (∼2% at normal incidence) creates marginal signal-to-noise conditions. Second, all existing LiDAR water-monitoring studies employ narrow spot-beam sensors; no study evaluates how wide line-beam geometry affects measurement stability over dynamic water surfaces.

More broadly, the literature lacks a side-by-side comparison of ultrasonic and LiDAR sensors under identical environmental stressors within a complete lab-to-field validation pipeline for river monitoring. Existing comparative studies address portions of the problem, for example Singh, Raghuwanshi, and Kumar (2018) review conventional versus optical liquid-level techniques, Tawalbeh et al. (2023) compare ultrasonic, short-range infrared, and pressure sensors, and Utepov et al. (2023) benchmark LiDAR alongside other time-of-flight sensors in sewer environments. But none of the studies subjects both acoustic and optical sensors to controlled and field stressors. Individual-technology studies evaluate either ultrasonic (Panagopoulos et al., 2021; Mohammed et al., 2019) or LiDAR (Paul; Buytaert; Sah, 2020; Tamari; Guerrero-Meza, 2016) sensors in isolation, while field deployments commit to a single technology without prior comparative validation (Kabi; Kamucha; Maina, 2023; Ragnoli et al., 2020).

This work addresses these gaps through a “Lab-to-Bridge” validation pipeline. Five non-contact distance sensors, two ultrasonic and three LiDAR, are first characterized under different environmental stressors. The validated sensors are then integrated into functional LoRaWAN-connected WSN nodes and deployed on rivers during rainy and sunny conditions.

1.2 OBJECTIVES

The primary objective of this work is to comparatively evaluate low-cost non-contact distance sensing technologies—LiDAR and ultrasonic—for river water level monitoring through a systematic Lab-to-Bridge validation pipeline, and to derive a validated WSN node design from the empirical findings.

1.3 SPECIFIC OBJECTIVES

The specific objectives of this work are:

1. Evaluate multiple non-contact distance sensing technologies under controlled laboratory conditions, characterizing distance range, precision, accuracy, and operational limits.
2. Compare spot-beam versus line-beam LiDAR geometries for water surface measurement stability.
3. Assess sensor resilience under simulated environmental stressors relevant to riverine deployment, including rain interference, water surface reflectivity (clear and turbid water), and ambient solar radiation.
4. Develop functional LoRaWAN-connected sensor nodes integrating the evaluated technologies.
5. Implement a complete data pipeline from sensor acquisition to cloud visualization.
6. Deploy and validate the integrated sensor nodes at real bridge sites over rivers under authentic weather conditions, including rain events.
7. Benchmark sensor performance against the international hydrological standard ISO 4373:2022, classifying each sensor technology by performance class.
8. Propose validated sensor selection criteria and a recommended WSN node architecture for scalable, cost-effective river level monitoring systems.

1.4 RESEARCH QUESTIONS

The experimental evaluation conducted in this work is guided by the following research questions:

1. What type of sensor technology is most suitable for river level monitoring in the context of low-cost, non-contact distance sensing?
2. How does beam geometry (spot-beam vs. line-beam) affect LiDAR measurement stability over dynamic water surfaces?

3. To what extent does ambient solar radiation limit the availability of low-cost LiDAR sensors for outdoor water level monitoring?
4. How does water turbidity influence LiDAR measurement accuracy, and do flood conditions improve or degrade optical sensor performance?
5. Can low-cost ultrasonic and LiDAR sensors meet the ISO 4373:2022 performance class requirements for hydrometric instruments when deployed at river bridge sites?

1.5 RESEARCH METHODOLOGY

This research is classified as applied and experimental in nature, with a quantitative approach to data analysis. Following the research classification frameworks proposed by Wazlawick (2009) and Prodanov and Freitas (2013), the work combines laboratory experimentation, field research, and a case study approach.

The technical procedures employed combine laboratory experimentation (controlled sensor evaluation in Phase 1), field research (real-world deployment in Phase 3), and a case study approach (Chapter 5), where specific hardware and software components are selected and evaluated within a defined deployment context. Data collection is performed through direct observation via instrumented measurement, with sensors serving as the primary data collection instruments.

1.6 STRUCTURE OF THE WORK

This research is organized into seven chapters. Chapter 2 first reviews the existing literature on WSNs, LoRa technology, and sensor technologies for hydrological monitoring, identifying the research gaps that this work addresses. Chapter 3 then provides the theoretical foundations—including IoT, LoRa/LoRaWAN, sensor technologies, and embedded systems—needed to understand the methodology and interpret the experimental results. This ordering allows the reader to appreciate the research context and gaps before engaging with the underlying technical concepts. Chapter 4 presents the general, replicable methodological framework, including system architecture design, evaluation strategy, data analysis methods with formal statistical equations, and evaluation criteria based on ISO 4373. Chapter 5 applies the methodology to the specific context of river level monitoring in Vale do Itajaí, detailing hardware and software selection, node implementation, LoRaWAN network integration, data backend development, and end-to-end system validation. Chapter 6 presents all experimental results across the three evaluation phases: controlled environment sensor testing (Phase 1), preliminary field testing at bridge sites with ISO 4373 benchmarking (Phase 2), and extended field deployments under rainy and sunny conditions (Phase 3). Finally, Chapter 7 draws conclusions from the research, discusses novel contributions, regional impact, recommendations, and directions for future work.

2 LITERATURE REVIEW

This chapter reviews the existing literature on wireless environmental monitoring technologies and non-contact sensing methods for water level measurement. The choice for wireless, non-contact sensor nodes is driven by the harsh and remote conditions typical of riverine environments, where wired infrastructure is impractical and contact-based instruments are vulnerable to debris, biofouling, and mechanical wear (Chen et al., 2013; Yellampalli, 2021). The chapter concludes with a critical analysis of identified research gaps and the specific contributions of this work (Section 2.11).

2.1 CLIMATE CHANGE AND FLOODS

The scientific consensus, articulated by the Intergovernmental Panel on Climate Change (IPCC), is that anthropogenic climate change is intensifying the global hydrological cycle, leading to an increased frequency and severity of flood events worldwide. This section examines the scientific evidence for climate-driven changes in flood patterns and their implications for monitoring systems. It is considered an established fact that human-caused greenhouse gas emissions have led to more intense and/or frequent weather and climate extremes (Pörtner et al., 2022). The primary physical mechanism is that a warmer atmosphere holds more moisture, approximately 7% more for every 1°C of warming, which provides more fuel for extreme precipitation. Consequently, the intensity of heavy precipitation has increased in many regions globally since the 1950s, a trend that is projected to continue with further warming (Pörtner et al., 2022).

This intensification of the hazard directly translates to greater disaster risk. Extreme weather events that cause highly impactful floods have become more likely and more severe due to human-induced climate change (Pörtner et al., 2022). Since the 1970s, 44% of all disaster events have been flood-related, and these events disproportionately affect vulnerable populations, particularly in the Global South. The IPCC notes with high confidence that several recent heavy rainfall events that led to substantial flooding in countries across the globe, including Brazil, were made more likely by anthropogenic climate change (Pörtner et al., 2022).

The impacts of this global trend are acutely felt in Brazil, which has experienced a series of devastating floods in recent years. The catastrophic flooding in the state of Rio Grande do Sul in May 2024, which was driven by record-breaking rainfall, serves as a stark example. A rapid attribution study concluded that human-induced climate change made this extreme rainfall event twice as likely, with the concurrent El Niño phenomenon also amplifying its intensity (Otto et al., 2024). This is not an isolated incident; similar studies have demonstrated the role of climate change in other major events, such as the 2021 extreme floods in the western Brazilian Amazon, where anthropogenic influence made the event 153% more likely to occur. These events underscore Brazil's vulnerability and highlight the urgent need for robust adaptation and mitigation strategies in response to the escalating flood risk.

2.2 IMPACTS OF FLOODING AND THE IMPORTANCE OF MITIGATION

The need for advanced environmental monitoring systems is underscored by the growing social and environmental impacts of hydrological disasters. This section explores the consequences of flooding events and establishes the rationale for improved monitoring capabilities. There is a scientific consensus that the global hydrological cycle is intensifying, leading to a general increase in the frequency and severity of extreme climate events, which in turn affects flood regimes (Hall et al., 2014). This phenomenon demands a shift in how flood data is analyzed; instead of merely detecting linear trends, research now suggests focusing on identifying "flood-rich" and "flood-poor" periods to better understand long-term dynamics.

A particularly dangerous and challenging aspect of this problem is the monitoring of flash floods. These events are often a rapid hydrological response to intense storms in small catchments, frequently escaping conventional monitoring networks due to their speed and localized nature. As noted by Borga et al. (2014), effective monitoring of these floods is critical for developing more efficient early warning systems and for calibrating the rainfall-runoff models used in prediction.

These environmental phenomena have profound social consequences, which are often exacerbated by historical patterns of land use. A study on the history of floods in the Itajaí Valley, Brazil, a region frequently affected by such events, demonstrates how the process of territorial occupation has forged situations of vulnerability that explain the tragic outcomes of modern-day floods (Santos; Tornquist; Marimon, 2014). This highlights that floods are not merely natural events, but complex socio-environmental disasters. Therefore, the development of robust and accessible monitoring technologies is not just a technical challenge, but a crucial step towards mitigating these impacts and building more resilient communities.

2.3 WSN AND LORAWAN

The evolution of environmental monitoring has shifted from labor-intensive manual data collection towards real-time, remote systems enabled by the advent of WSNs (Pule; Yahya; Chuma, 2017). This section reviews the fundamental technologies that enable modern wireless monitoring systems, with particular focus on LoRaWAN as a communication solution for remote deployments. The demand for long-range and energy-efficient communication for these remote deployments caused the emergence of Low Power Wide Area Networks (LPWANs) as a new IoT paradigm (Sun et al., 2022). Within this landscape, LoRa is a dominant physical layer modulation technique, while the LoRaWAN protocol defines the system architecture, typically a star-of-stars topology, governing communication between end-devices and central servers. As highlighted by multiple surveys, LoRaWAN is specifically designed for applications that send small amounts of data over long distances, with its low-power features offering a theoretical battery autonomy of up to ten years (Sun et al., 2022). In this topology, end-devices communicate directly with one or more gateways, which relay messages to a central network server; the gateways do not perform protocol-level routing, which simplifies the network architecture (see Figure 6 in Chapter 5 for an illustration). However, while this technology effectively solves the challenge of remote communication, Pule, Yahya, and Chuma (2017) also provide a critical perspective, cautioning that many system architectures, while using the cloud for data access, often neglect cybersecurity, leaving the collected environmental data vulnerable to attacks.

Empirical studies have validated LoRaWAN's range capabilities for environmental monitoring applications. Orlovs et al. (2025) conducted a comparative analysis of LPWAN technologies, demonstrating that LoRaWAN achieves 11 km range in rural environments, which validates its suitability for river basin monitoring deployments. This range significantly outperforms Sigfox (10 km maximum) and is superior to NB-IoT, which requires cellular infrastructure that may be unavailable in remote river locations. Furthermore, their energy analysis quantified LoRaWAN message transmission cost at approximately 82.2 µWh per message, establishing a baseline for battery life calculations in sensor node design.

Comparative analysis between LPWAN technologies has provided critical insights for flood monitoring deployments. Ballerini et al. (2020) conducted an experimental evaluation comparing NB-IoT and LoRaWAN for industrial and IoT applications, demonstrating that while NB-IoT offers superior Quality of Service (QoS), lower latency, and higher throughput, it incurs a significant energy penalty due to synchronization overhead and higher peak transmission currents (>200 mA). For the infrequent, small-payload traffic characteristic of flood sensors (e.g., 4 bytes every 15 minutes), LoRaWAN consumes approximately an order of magnitude less energy than NB-IoT. Additionally, NB-IoT's reliance on cellular infrastructure presents a vulnerability during disaster scenarios, as base stations powered by grid electricity may fail during major floods, whereas LoRaWAN gateways can be easily solar-powered and deployed ad-hoc. This empirical evidence strongly supports LoRaWAN as the preferred technology for off-grid, energy-constrained flood monitoring deployments.

2.3.1 LoRaWAN Network Performance and Scalability

The scalability and performance characteristics of LoRaWAN networks are critical factors for large-scale flood monitoring deployments. Network capacity studies have revealed important limitations that must be considered in network planning. Mikhaylov, Petäjäjärvi, and Hänninen (2018) analyzed the capacity and scalability of LoRaWAN technology, demonstrating that as the number of nodes increases, collision probability grows non-linearly with the Time on Air. This relationship means that network capacity is not simply a function of available channels, but also depends on the Spreading Factor distribution and transmission frequency. For flood monitoring applications where multiple nodes may trigger high-frequency transmissions during emergency conditions, network congestion can significantly impact both reliability and energy consumption. The analysis reveals that LoRaWAN networks can support up to 1000 devices per gateway under optimal conditions, but this capacity decreases substantially when nodes must use higher spreading factors due to poor signal conditions or when transmission frequency increases during critical events.

2.3.2 Power Management in LoRaWAN Sensor Nodes

Achieving long-term autonomous operation in remote environmental monitoring deployments requires careful power management strategies. The ESP32 microcontroller, used in this project, offers advanced power management capabilities including multiple sleep modes. Deep sleep mode, which powers down most of the system while maintaining only the real-time clock (RTC) and a small amount of memory, can reduce power consumption from hundreds of milliamperes during active operation to approximately 10 microamperes (Systems, 2023). This dramatic reduction in power consumption enables battery-powered sensor nodes to operate for extended periods, with battery life estimates ranging from months to years depending on the transmission frequency and active duty cycle.

The implementation of deep sleep strategies in LoRaWAN sensor nodes is a well-established practice in IoT deployments. By configuring nodes to wake only for sensor readings and data transmission, then immediately returning to deep sleep, the overall power consumption can be reduced by several orders of magnitude. This approach is particularly important for environmental monitoring applications where nodes may be deployed in remote locations with limited or no access to power infrastructure.

Foundational energy modeling frameworks have been established to predict and optimize the energy budget of LoRaWAN sensor nodes. Casals et al. (2017) established the theoretical baseline for LoRaWAN battery estimation, deriving equations that link hardware sleep currents, protocol overheads, and transmission parameters. Their model demonstrated that a device with a 2400 mAh battery could theoretically achieve a 6-year lifespan with 5-minute reporting intervals, provided the node uses Spreading Factor 7 (SF7). This finding underscores the critical importance of gateway density: more gateways allow nodes to use lower spreading factors, directly extending battery life. The model decomposes the energy consumption into discrete states: wake-up energy, sensor measurement energy, processing energy, transmission energy, and receive window energy for acknowledgments. Importantly, the transmission energy ($E_{tx} = V \cdot I_{tx} \cdot T_{oa}$) is dominated by the Time on

Air (T_{oa}), which increases exponentially with the Spreading Factor. Increasing SF from 7 to 12 can increase transmission time from 40 ms to 1500 ms, representing a nearly 40-fold increase in energy consumption for the same data packet.

Complementing this work, Bouguera et al. (2018) developed an energy consumption model that decomposes node operation into discrete states, allowing for precise lifetime estimation. Their model accounts for the operational state machine, including sleep states, wake-up overhead, measurement phases, and communication windows. Mikhaylov, Petäjäjärvi, and Hänninen (2018) expanded these models to account for stochastic network effects, demonstrating that in dense networks or during events where many nodes transmit simultaneously, collisions occur with increasing probability. The average energy per successfully delivered packet becomes $E_{packet} = E_{cycle}/(1 - P_{error})$, where P_{error} combines collision probability and channel error rates. This non-linear relationship implies that a congested network drains batteries significantly faster than a clean one, highlighting the importance of network planning and adaptive duty cycling strategies.

In their work, Ferreira, Silvério, and Viana (2023) present a comprehensive case study on the design of an autonomous sensor node for a WSN aimed at detecting and classifying pollutants in aquatic environments. Their system provides a complete solution by integrating multiple sensors, measuring pH, turbidity, temperature, and conductivity, with a LoRa-based communication network and an embedded machine learning model for on-site pollutant classification. Powered by a photovoltaic panel and battery system to ensure long-term deployment, the node's viability was demonstrated through a structured process of modeling, implementation, and successful indoor testing with oil derivatives.

Recent field validation studies have confirmed the viability of ESP32-based nodes for long-term deployments. Pires and Veiga (2025) demonstrated that ESP32 sensor nodes, when properly optimized with deep sleep strategies, can achieve multi-month battery life using 2600mAh batteries. Their implementation validates that the theoretical power consumption specifications can be achieved in practice, enabling autonomous operation for extended periods without external power infrastructure. Additionally, their work highlights the importance of integrating structural health monitoring capabilities, such as MEMS accelerometers, to detect physical displacement or tilting of sensor nodes, which is critical for ensuring measurement validity in flood-prone environments.

2.4 ULTRASONIC SENSORS

The viability of low-cost ultrasonic sensors for monitoring water levels in open channels and rivers is a recurring theme in recent literature, with multiple studies validating their performance for environmental applications. This section reviews the state-of-the-art in ultrasonic sensing technology for hydrological monitoring. For instance, in research aimed at developing a high-accuracy device specifically for flood monitoring, Masoudi-Moghaddam, Yazdi, and Shahsavandi (2024) tested the GY-Us42 sensor. By applying specific error reduction techniques and validating the device in both controlled environment and field settings, including under challenging conditions with foamy waves, they demonstrated an average measurement error below 3%.

A comprehensive validation study by Panagopoulos et al. (2021) conducted a direct comparison between ultrasonic sensors and submersible pressure transducers in an urban stream environment. Their findings revealed that ultrasonic sensors tracked pressure transducers within 7% variance, confirming their viability for water level monitoring applications. However, the study identified a critical limitation: ultrasonic sensors exhibited distinct diurnal fluctuations correlated with air temperature changes, even when water level remained stable, with the authors recommending external temperature measurement for improved compensation as future work. This temperature sensitivity is a well-known property of acoustic ranging: the speed of sound in air varies approximately as $v(T) \approx 331.3 + 0.606 \cdot \theta$ m/s (Wong; Embleton, 1985), introducing a systematic bias of roughly 1.8 mm per meter of range per degree Celsius if left uncompensated. In a separate study, Mohammed et al. (2019) demonstrated that low-cost ultrasonic sensors can achieve sub-centimeter accuracy (0.07 cm error) for water level measurement in tank environments, confirming the viability of these sensors for precise applications.

This conclusion of technical and economic viability for ultrasonic sensors is echoed in other work, which identifies the popular HC-SR04 model as a feasible alternative for water level monitoring (Pereira et al., 2022). Beyond technical applications, the low cost and accessibility of these sensors have also led to their recognition as valuable tools for education, citizen science initiatives, and preliminary research projects (Bresnahan et al., 2023).

Beyond temperature, wind represents an additional environmental factor affecting ultrasonic measurement accuracy. Radu Tarulescu and Stelian Tarulescu (2014) demonstrated that wind velocity vectorially adds to the speed of sound, introducing directional measurement errors: perpendicular crosswinds at 12 m/s caused a consistent overestimation of approximately 6.9 mm (1.38% relative error), while parallel winds caused underestimation. For bridge-mounted sensors exposed to open river valleys—where sustained winds are common—this wind-induced drift adds to the temperature drift already documented by Panagopoulos et al. (2021), further limiting the achievable accuracy of ultrasonic sensors in unshielded outdoor installations.

The vulnerability of ultrasonic sensors to adverse weather extends to precipitation. Sumi et al. (2024) conducted a systematic evaluation of non-contact safety sensors under controlled rainfall conditions, revealing that light drizzle with high densities of small droplets (<1 mm) paradoxically caused higher failure rates than heavy rain in some ultrasonic sensors, due to acoustic scattering saturation from the dense droplet field. In extreme conditions, field reports from hurricane monitoring deployments document that ultrasonic sensors produced noisy, unreliable data during high wind and rain events, while radar-based sensors maintained continuous accurate readings through wind speeds exceeding 160 km/h (Mukai, 2025). These findings highlight a fundamental limitation of acoustic sensing in exposed riverine environments: while ultrasonic sensors perform reliably under calm conditions, their accuracy degrades under the combined effects of wind and rain—precisely the conditions associated with the flood events they are intended to monitor.

2.5 LIDAR SENSORS

To address the challenge of safely monitoring flash floods, Tamari and Guerrero-Meza (2016) and Tamari et al. (2016) evaluated an inclined LiDAR technique for water level monitoring. The method operates by having the LiDAR's near-infrared beam detect suspended particles in the water, meaning higher turbidity leads to better quality readings. During field tests at the Amacuzac River, the authors validated this principle for flood stage data with good accuracy (±0.08 m), while a long-term assessment (over 2 years) in turbid reservoirs confirmed that the technique provides reliable data in turbid conditions, specifically when the water Secchi depth is below approximately 1.0 m, indicating sufficient suspended sediment concentration for adequate LiDAR return signal. Their work serves as a proof of concept for the technique as a low-cost and safe monitoring option, while highlighting that its viability is dependent on the water reaching a sufficient level of turbidity.

In a technical evaluation of emerging non-contact sensors, Paul, Buytaert, and Sah (2020) investigated the suitability of a low-cost, near-infrared LiDAR sensor for measuring river water levels. Their controlled environment and field tests demonstrated that despite the low reflectivity of water, the sensor could achieve high accuracy with a relative error of approximately 0.1% and a range of up to 30-35 meters, significantly outperforming typical ultrasonic sensors in range. However, the study identified a critical limitation: the sensor's accuracy was strongly dependent on its internal temperature, indicating a need for thermal control or compensation for reliable deployment. While precision improved with water surface roughness, it decreased as the measurement distance increased. The authors conclude that LiDAR is a practical and cost-efficient method with significant potential for expanding hydrometric networks in data-scarce regions, provided the issue of thermal stability is addressed.

In a study motivated by recurring hydrological disasters in Brazil, Santana, Salustiano, and Tiezzi (2024) conducted a direct comparative analysis between a low-cost LiDAR sensor and a traditional, more expensive limnigraph for river level measurement. Their results demonstrated that the data obtained from the low-cost LiDAR were equivalent to those from the limnigraph, achieving a notable accuracy of ±0.05 m when compared to a physical metric scale. Importantly, the study found that the LiDAR's measurements were not impacted by the presence of sediments in the water, indicating a strong potential for reliable performance in real-world field conditions. The authors conclude that the LiDAR sensor is an excellent and advantageous alternative capable of replacing traditional limnigraphs, presenting a highly promising approach for developing more accessible and robust environmental monitoring systems.

The turbidity dependence identified by Tamari and Guerrero-Meza (2016) and Tamari et al. (2016) was quantified more precisely by Jannata, Salam, and Suhendi (2021), who evaluated near-infrared LiDAR sensors (including the TF-Luna) for water level measurement across a range of turbidity conditions. Their results established that infrared LiDAR at 850 nm requires a minimum turbidity of approximately 700 NTU to reliably detect the water surface: at 700 NTU the measurement error was 5.2%, improving to 2.6% at 900 NTU (muddy/flood conditions), while clear water below 300 NTU produced errors exceeding 21% or outright detection failure. This turbidity threshold has significant practical implications, as flood conditions—when accurate monitoring is most critical—typically produce turbidity levels well above 700 NTU due to suspended sediment.

A complementary sensor comparison by Utepov et al. (2023) evaluated the TF-Luna alongside ultrasonic and time-of-flight laser sensors for liquid level monitoring in sewer environments, finding the TF-Luna achieved a standard deviation of 0.44–1.15 cm in the 1–5 meter range, while shorter-range time-of-flight sensors degraded significantly at distance (standard deviation up to 10 cm). These comparative results reinforce the TF-Luna's viability for medium-range liquid level monitoring, while highlighting the sensor-specific trade-offs between range, precision, and environmental tolerance.

Regarding precipitation resilience, LiDAR sensors demonstrate a fundamentally different failure mode compared to ultrasonic sensors under rain conditions. Goodin et al. (2019) modeled the physics of rain-induced signal attenuation in LiDAR systems, showing that rain reduces signal intensity through Mie scattering with an extinction coefficient proportional to rainfall rate. However, even at a heavy rainfall rate of 45 mm/h, the maximum detection range was reduced by only approximately 6 meters—a modest degradation that leaves LiDAR sensors operational for typical bridge-mounted installations where sensor-to-water distances are below 15 m. This contrasts with the acoustic saturation and "whiteout" failures reported for ultrasonic sensors under similar conditions (Sumi et al., 2024), suggesting that LiDAR offers superior rain resilience for continuous monitoring applications.

The review by Singh, Raghuwanshi, and Kumar (2018) provides a comparative analysis of liquid-level measurement technologies, categorizing them into conventional and optical methods. They note that while the conventional methods are generally low-cost, they can present challenges related to maintenance and operational lifetime. In contrast, the paper highlights optical techniques as a more modern and preferable approach, offering significant advantages such as high accuracy and immunity to electromagnetic interference. The authors conclude by presenting a critical trade-off: optical sensors, while superior in performance, involve a higher cost and are more vulnerable to environmental conditions than their conventional counterparts.

2.6 ALTERNATIVE MEASURING METHODS

Beyond LiDAR and ultrasonic sensors, other non-contact technologies are also being explored. This section briefly reviews alternative approaches such as computer vision, radar, and satellite remote sensing, providing context for why these methods were not selected for this work. A systematic review by Wu et al. (2023) highlights the principles and challenges of using computer vision and radar for water level measurement. The authors note that computer vision techniques have evolved from traditional algorithms toward deep learning-based approaches, but progress is often hampered by the lack of large-scale benchmark datasets. While photogrammetry offers high resolution, it faces challenges in complexity and calibration. Similarly, radar technology is limited by the trade-off between resolution, accuracy, and computational complexity. Wu et al. (2023) conclude that future improvements in non-contact water level measurement will likely come from multi-view and multi-mode sensor fusion, combining the strengths of different technologies.

An alternative hardware approach that sidesteps the challenge of direct water surface detection is the float-controlled laser gauge developed by Pierret et al. (2025). Rather than measuring distance to the water surface directly, their system uses a float mechanism that rises with water level, and a ToF laser measures the position of the float. This design achieves ±1 mm precision at temperatures between 20-30°C and 2 mm accuracy compared to manual readings, at a cost of approximately EUR 220. The system operates autonomously for several weeks without external power or solar panels, making it suitable for remote tropical environments. While this approach avoids the optical challenges of water surface reflectivity, it requires physical contact with the water and a stilling well or guide structure, making it more susceptible to debris damage and requiring more complex installation than fully non-contact sensors.

A hybrid approach combining image recognition with wireless sensor networks was proposed by Yukawa et al. (2025), who developed an intelligent water level estimation system that uses gauge image recognition alongside WSN data. Their system demonstrates that combining visual and sensor-based measurements can improve estimation robustness, though it requires visible gauge infrastructure and clear imaging conditions. Another innovative approach by DAO et al. (2025) introduced an energy-harvesting beat sensor with LoRa communication for water-level monitoring, achieving high accuracy and long communication range while eliminating the need for battery replacement through ambient energy harvesting. Their work demonstrates an alternative sensing principle that, while promising for long-term deployments, requires physical contact with the water body.

In addition to ground-based systems, satellite remote sensing offers a powerful alternative for large-scale and long-term hydrological monitoring. For instance, Jiang and

Hong (2024) employed a multi-source data fusion method via Google Earth Engine to estimate water level changes in nine plateau lakes over a 20-year period, achieving high consistency with measurements (deviations under 0.3 meters). Similarly, Ali et al. (2024) utilized Sentinel-3A radar altimetry to assess dam-induced water level changes in the Mekong River basin, validating their satellite-derived data against ground telemetry with a correlation of 0.98. These studies confirm that satellite-based techniques are a highly viable and accurate approach, particularly for monitoring vast, remote, or transboundary water bodies where deploying ground networks is impractical.

2.7 DATA COLLECTION AND FUTURE ANALYTICAL POTENTIAL

Effective environmental monitoring is inherently a data-intensive challenge, complicated by large spatial scales, environmental uncertainties, and harsh operating conditions. As Chen et al. (2013) highlight, WSNs address these issues by offering advantages in cost, responsiveness, and scalability over conventional manual approaches, enabling continuous data collection from remote or hazardous locations. Their work reinforces the need for robust system design focused on reliable data transmission and energy efficiency—both critical requirements for building effective early warning systems.

The data generated by such networks also provides a foundation for advanced analytical techniques. Recent reviews have examined the application of AI for environmental prediction and water quality assessment (Mukhopadhyay et al., 2021; N.R. et al., 2025), demonstrating that machine learning models can enhance sensor data interpretation and enable predictive capabilities. However, these studies consistently identify two prerequisites for effective AI deployment: large, high-quality datasets collected over extended periods, and region-specific training data that captures local hydrological characteristics. This underscores the importance of reliable, long-term WSN deployments—such as the one developed in this work—as the data infrastructure upon which future predictive models can be built.

2.8 CYBERSECURITY IN ENVIRONMENTAL MONITORING

The widespread integration of embedded systems in IoT architectures introduces critical security challenges, particularly as these systems perform real-time sensing and decision-making in sensitive contexts (Pimentel, 2017). This section addresses security considerations relevant to WSN deployments, particularly in the context of critical monitoring applications. As embedded systems now support safety-critical applications, ensuring reliability and resilience becomes essential (Koulamas; Lazarescu, 2018). A compromised device can threaten the entire IoT network, highlighting the need for robust, integrated security, especially in edge processing, where minimizing data transfer also reduces the attack surface (Tien, 2017).

In the context of hydrological monitoring for flood alerts, the integrity and availability of sensor data are paramount. A successful cyberattack could manipulate water level data, leading to a failure to issue a timely warning (a false negative) or triggering a false alarm that causes unnecessary public panic and economic disruption. The deployment of low-cost sensor nodes in public, often remote, locations also exposes them to physical tampering. Therefore, securing the data from the sensor node to the end-user is a critical aspect of system design, ensuring that the early warnings generated are trustworthy and reliable. While comprehensive security implementation is beyond the scope of this work, the developed system architecture considers security as a design requirement for future enhancements.

2.9 ALTERNATIVE DATA COLLECTION STRATEGIES

While fixed Wireless Sensor Networks using LoRaWAN are common, alternative architectures have emerged to overcome challenges related to infrastructure, energy, and scalability in large areas (Yellampalli, 2021). This section reviews mobile and hybrid approaches that complement traditional fixed WSN deployments. One prominent strategy is the use of vehicles for mobile data collection.

For example, Deng et al. (2020) developed a hybrid system for agricultural monitoring that uses passive RFID soil sensors and a patrol vehicle. The vehicle acts as a mobile gateway, collecting data as it moves through the area. This approach offers low cost and high energy efficiency by leveraging backscatter communication to transmit environmental data to a central platform without requiring batteries in the sensors themselves.

In a similar vein, Caruso et al. (2021) introduced a drone-based system where UAVs equipped with LoRa radios periodically collect data from ground sensors. This method is ideal for areas without fixed communication infrastructure or where real-time updates are not essential. The work includes an adaptable model for optimizing the drone's flight path and the layout of ground sensors, making it a flexible solution for various monitoring scenarios.

2.10 FIELD DEPLOYMENT AND LONG-TERM OPERATION

While controlled environment testing provides valuable insights into sensor performance, real-world field deployments present unique challenges that can only be validated through extended operational periods. A critical gap in the literature has been the lack of long-term field deployment studies that demonstrate the viability of low-cost LoRaWAN sensor nodes in harsh environmental conditions.

Kabi, Kamucha, and Maina (2023) addressed this gap by conducting an 18-month field deployment of a low-cost river level monitoring system on the Muringato River in Kenya. Their system utilized an ARM-Mbed platform (comparable in capability to ESP32) interfaced with ultrasonic sensors and LoRaWAN communication. This longitudinal study validated several critical aspects of river monitoring deployments: first, that low-cost LoRaWAN nodes can survive long-term exposure if properly enclosed (IP67 rating); second, that raw sensor data in river environments is prone to significant noise from turbulence and debris, necessitating machine learning or statistical filtering for usable hydrological insights; and third, that LoRaWAN can reliably transmit data from river gorges where cellular signals fail, demonstrating the technology's advantage in remote locations. Their work serves as a reference design for open-source river monitoring systems and provides empirical validation of system reliability over extended operational periods, addressing a critical requirement for practical deployment in resource-constrained regions.

A complementary study by Ragnoli et al. (2020) documented a full-stack implementation of an autonomous low-power LoRa-based flood monitoring system deployed in Italy. Their work combined ultrasonic sensing with a custom "smart sleep" algorithm and solar energy harvesting, achieving indefinite theoretical autonomy (limited only by battery cycle life) by carefully balancing the solar recharge rate with the daily energy consumption budget calculated via energy models. The system's innovation lies in its adaptive duty cycling strategy: during normal conditions, the node sleeps for 60 minutes, but if the water level change rate ($\Delta h/\Delta t$) exceeds a threshold, the system switches to "Alert Mode," reducing the interval to 5 minutes. This approach balances longevity with granular data during critical flood events. Their work demonstrates that theoretical energy models, when properly implemented with adaptive algorithms, can be translated into practical, long-term autonomous deployments, validating the feasibility of solar-powered LoRaWAN sensor nodes for river monitoring applications.

2.11 RESEARCH GAPS AND CONTRIBUTION OF THIS WORK

The preceding sections reveal a diverse landscape of water level measurement technologies, from contact-based methods (pressure transducers, float gauges) to non-contact approaches (ultrasonic, LiDAR, radar, computer vision, satellite remote sensing). Table 2 compares these approaches and justifies the selection of ultrasonic and LiDAR as the sensing technologies for this work.

Table 2 – Comparison of water level measurement technologies and selection rationale.

Technology	**Key Advantages**	**Limitations for River Monitoring**	**Selection Rationale**
Ultrasonic (non-contact)	Low cost, proven track record, simple interface (Pereira et al., 2022; Masoudi-Moghaddam; Yazdi; Shahsavandi, 2024)	Limited range (<5 m), temperature-dependent, weather-sensitive (Panagopoulos et al., 2021; Tarulescu, R.; Tarulescu, S., 2014)	**Selected**: widely validated baseline for comparative evaluation
LiDAR (ToF)	Long range (up to 40 m), high accuracy, fast response (Paul; Buytaert; Sah, 2020; Santana; Salustiano; Tiezzi, 2024)	Reflectivity dependent on turbidity, higher cost than ultrasonic (Tamari; Guerrero-Meza, 2016; Tamari et al., 2016; Jannata; Salam; Suhendi, 2021)	**Selected**: emerging alternative with superior range for bridge installations
Pressure transducer	High accuracy, well-established in hydrology (Panagopoulos et al., 2021)	Requires submersion, vulnerable to debris and corrosion (Ragnoli et al., 2020)	Not selected: contact-based, higher maintenance
Radar	All-weather operation, long range (Mukai, 2025)	High cost, complex signal processing (Wu et al., 2023)	Not selected: cost prohibitive for low-cost WSN nodes
Computer vision	Rich spatial data (Yukawa et al., 2025)	Lighting-dependent, calibration complexity, high power (Wu et al., 2023)	Not selected: incompatible with low-power LoRaWAN nodes
Satellite	Large-scale coverage (Jiang; Hong, 2024; Ali et al., 2024)	Coarse temporal/spatial resolution, non-real-time	Not selected: insufficient for local real-time monitoring

Source: The author.

Existing comparative studies address portions of the sensor-selection problem: Singh, Raghuwanshi, and Kumar (2018) compare conventional versus optical liquid-level measurement techniques, Tawalbeh et al. (2023) evaluate ultrasonic, short-range infrared, and pressure sensors for water level monitoring, and Utepov et al. (2023) benchmark LiDAR alongside other time-of-flight sensors for liquid-level detection in sewer environments. However, no published study subjects both ultrasonic and LiDAR sensors to identical controlled *and* field environmental stressors within a complete lab-to-field validation pipeline for river monitoring. The broader literature follows the same pattern: individual-technology evaluations test ultrasonic (Panagopoulos et al., 2021; MasoudiMoghaddam;

Yazdi; Shahsavandi, 2024) or LiDAR (Paul; Buytaert; Sah, 2020; Tamari; Guerrero-Meza, 2016) sensors in isolation, while field deployments commit to a single technology *a priori* (Kabi; Kamucha; Maina, 2023; Ragnoli et al., 2020).

Beyond this comparative gap, two specific aspects of low-cost LiDAR behavior over water remain unquantified. First, prior LiDAR water-monitoring studies focus on water-related factors, turbidity (Tamari; Guerrero-Meza, 2016; Jannata; Salam; Suhendi, 2021), reflectivity (Paul; Buytaert; Sah, 2020), and surface roughness, while the effect of ambient solar radiation on measurement reliability is unexplored. This omission is significant because low-cost 905–940 nm ToF sensors operate in the same spectral band as solar radiation, and water surfaces provide only ∼2% specular reflectance (Equation (1)). Strong background light such as direct sunlight is a recognized noise source in SPAD-based LiDAR detectors (Villa et al., 2021), and Hama et al. (2022) deliberately conducted low-cost LiDAR experiments indoors to avoid sunlight interference. Yet no study quantifies this failure mode over water surfaces, where the baseline return signal is orders of magnitude weaker than from solid targets.

Second, all existing LiDAR water-monitoring studies employ spot-beam sensors with narrow fields of view (2–3°). No study has investigated how wide line-beam geometry, such as the 14°×1° field of view available in commercial modules, affects measurement stability over dynamic water surfaces. Industrial automation literature documents that line-beam sensors average out surface irregularities for stable detection, and airborne oceanography exploits larger laser footprints for spatial wave averaging, but this geometric advantage has not been evaluated for stationary IoT water gauges.

Table 3 maps the four primary research gaps to the specific contributions of this research.

Table 3 – Research gaps identified in the literature and corresponding research contributions.

Gap Focus	**Key References**	**Research Contribution**
Comparative lab-to-field validation	Studies evaluate sensors in isolation; no complete pipeline tests ultrasonic vs LiDAR under identical stressors (Singh; Raghuwanshi; Kumar, 2018; Tawalbeh et al., 2023; Masoudi-Moghaddam; Yazdi; Shahsavandi, 2024; Kabi; Kamucha; Maina, 2023; Ragnoli et al., 2020)	Side-by-side evaluation of 5 sensors through a 3-phase Lab-to-Bridge pipeline under rain, turbidity, temperature, and sunlight
Ambient solar radiation on LiDAR over water	Literature focuses on water-related factors; sunlight effect unquantified (Paul; Buytaert; Sah, 2020; Tamari; Guerrero-Meza, 2016; Villa et al., 2021; Hama et al., 2022)	Field evaluation under overcast vs direct sunlight; solar identified as critical sensor-design-dependent limitation
Spot-beam vs line-beam LiDAR	All LiDAR water studies use spot-beam sensors (Paul; Buytaert; Sah, 2020; Tamari; Guerrero-Meza, 2016; Jannata; Salam; Suhendi, 2021)	Comparative evaluation of 3° spot-beam and 14°×1° line-beam; identification of Line Integration Effect
Turbidity effects on LiDAR	Conflicting findings: “no impact” vs 700 NTU threshold (Paul; Buytaert; Sah, 2020; Tamari; Guerrero-Meza, 2016; Jannata; Salam; Suhendi, 2021; Utepov et al., 2023)	Empirical tests show muddy water improves LiDAR accuracy via Mie scattering

Source: The author.

This work addresses the identified gaps through a three-phase Lab-to-Bridge pipeline: controlled sensor characterization under simulated stressors (Phase 1), system integration and preliminary field validation (Phase 2), and extended field deployment on active river bridges (Phase 3). The validated sensors are integrated into LoRaWAN-connected WSN nodes using commercially available ESP32-based development boards, implementing deep sleep power management (Casals et al., 2017; Pires; Veiga, 2025), adaptive transmission intervals (Ragnoli et al., 2020), and real-time speed-of-sound compensation for ultrasonic measurements (Equation (6)). The contribution is a validated reference design and comparative dataset that empirically characterizes the strengths and limitations of low-cost LiDAR versus ultrasonic sensing for riverine environments, not a commercial-ready early warning system.

This work advances the field of low-cost environmental monitoring by contributing at three complementary levels: methodological, experimental, and architectural. A structured Lab-to-Field validation framework for non-contact river level sensing is proposed and demonstrated. Unlike prior studies that isolate laboratory or field evaluation, this work integrates controlled environmental stress testing, bridge-level validation, and real-world deployment into a unified experimental pipeline. This framework is replicable and transferable to other environmental sensing applications.

The study provides the first side-by-side experimental comparison of low-cost ultrasonic and LiDAR sensors under identical environmental stressors, including rain interference, turbidity variation, and ambient solar radiation over natural water surfaces. The work quantifies the impact of solar radiation on measurement availability and identifies the stabilizing effect of beam geometry over dynamic surfaces.

A validated low-cost LoRa-based sensor node architecture is proposed, integrating sensing, embedded processing, adaptive transmission logic, and cloud data pipeline into a coherent and field-validated system. The proposed architecture demonstrates compliance with ISO 4373:2022 and supports scalable deployment in data-scarce tributaries.

3 THEORETICAL FRAMEWORK

This chapter presents the theoretical foundation for the proposed water level monitoring system. It discusses the essential technologies and concepts, including the IoT (Internet of Things), long-range wireless communication (LoRa (Long Range)/LoRaWAN), distance measurement methods such as LiDAR (Light Detection and Ranging) and ultrasonic sensors, and embedded systems. These topics establish the context and technical justification for the architecture adopted in this work.

3.1 IOT

The IoT encompasses a network of interconnected physical objects that are equipped with sensors, processors, and communication interfaces, allowing them to collect, process, and transmit data without human intervention (Madakam; Ramaswamy; Tripathi, 2015). The proliferation of IoT has enabled the deployment of intelligent systems in areas such as agriculture, industrial monitoring, and environmental surveillance (Javaid et al., 2021).

In this project, IoT concepts are applied to create an autonomous and distributed sensor network capable of collecting hydrological data and transmitting it remotely for analysis and visualization (Javaid et al., 2021).

3.2 LORA AND LORAWAN

LoRa (Long Range) is a proprietary spread spectrum modulation technique on the basis of CSS (Chirp Spread Spectrum), which is resilient and robust against interference and noise, it also provides a solution for long-range and ultra-low power-consumption transmission, using unlicensed radio bands such as 868 MHz (Europe) and 915 MHz (Americas) (Sun et al., 2022).

LoRaWAN (Long Range Wide Area Network) is the MAC (Medium Access Control) protocol built on top of LoRa, specifying how end-devices communicate with central gateways and application servers, defining a typical star-topology network architecture and its bi-directional communication protocol. The technology has been designed for applications that need to send small amounts of data over long distances a few times per day. Its low power features offer the capability to achieve autonomy of up to 10 years (Pule; Yahya; Chuma, 2017; Sun et al., 2022). Such long-range and energy-efficient communication demands have inspired the emergence of Low Power Wide Area Networks (LPWANs) as a new IoT paradigm, which fills the gap of legacy wireless communication technologies shown in Figure 1.

The theoretical claims of LoRaWAN regarding long-range and low-power operation have been empirically validated. Field measurements confirm ranges exceeding 10 km in rural environments and energy consumption approximately an order of magnitude lower than cellular-based alternatives for infrequent, small-payload traffic (Orlovs et al., 2025; Ballerini et al., 2020), as reviewed in Chapter 2. These results confirm that theoretical energy consumption models predicting multi-year battery life are achievable in practice when proper power management strategies are implemented.

Figure 1 – Comparison with legacy wireless communication technologies.

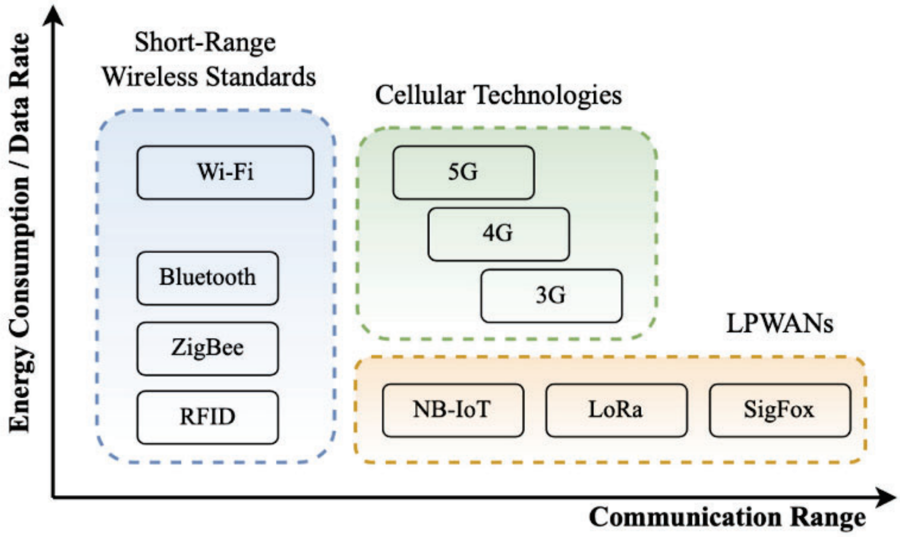

Source: (Sun et al., 2022).

3.3 MICROCONTROLLER ESP32 AND LORA-ENABLED DEVELOPMENT BOARDS

Embedded systems are specialized computing systems designed to perform dedicated functions within larger systems, often under real-time constraints. In environmental monitoring applications, microcontroller-based platforms provide the necessary processing capabilities while meeting the stringent power constraints of battery-operated field deployments. For this project, ESP32-based development boards with integrated LoRa communication capabilities were selected due to their combination of processing power, low-power modes, and community support. The ESP32 is a dual-core microcontroller that offers significant advantages over its predecessor, the ESP8266, including more processing power, Bluetooth connectivity, and enhanced low-power modes (Systems, 2023).

Several commercially available development boards integrate the ESP32 microcontroller with a Semtech SX1276/8 LoRa transceiver module on a single board, providing a complete solution for long-range, low-power wireless communication (Kolban, 2016). Representative examples include the Heltec WiFi LoRa 32 V2, which features an ESP32-WROOM-32 module, integrated OLED display (128×64), and built-in battery management circuitry; and the LilyGo T-Beam V1.2, which offers enhanced capabilities with an integrated AXP2101 PMU, onboard 18650 battery holder, and GPS module. Both platforms provide extensive community support and are widely used in academic and industrial IoT projects due to their ease of programming, low cost, and advanced features. The practical implementation of ESP32-based LoRaWAN nodes has been validated through field deployments (Pires; Veiga, 2025; Ragnoli et al., 2020), confirming that these development boards can achieve the theoretical power consumption specifications required for long-term autonomous operation.

The theoretical power consumption specifications of the ESP32 have been validated through field studies. The ESP32's deep sleep mode, which theoretically consumes 10-150 µA depending on board design and regulator efficiency, has been empirically validated by Pires and Veiga (2025), who demonstrated multi-month battery life using 2600 mAh batteries with proper deep sleep implementation. Furthermore, theoretical energy consumption models developed by Casals et al. (2017) and Bouguera et al. (2018) have been validated through field deployments, confirming that ESP32-based nodes can achieve the theoretical battery lifespans predicted by analytical models when proper power management strategies are implemented. These models decompose the node's energy consumption into discrete states (sleep, wake-up, measurement, processing, transmission, receive windows), allowing precise lifetime estimation based on duty cycle and transmission parameters.

3.4 LIDAR

LiDAR (Light Detection and Ranging) technology enables the accurate determination of an object's distance (and velocity) information and is widely used in metrology, environment monitoring, archaeology, and robotics (Li et al., 2022). Compared with more mature RADAR (Radio Detection and Ranging) technology, LiDAR makes use of optical waves at shorter wavelengths, and hence has the potential to achieve higher precision in 3D sensing (Behroozpour et al., 2017).

The principle of LiDAR ranging relies on the rugosity of the reflective surface to generate nonspecular reflection (i.e., scattering) of the incipient laser beam (Smart; Bind; Duncan, 2009). As with radar, LiDAR ranging measures time of flight, but it uses higher frequency waves for greater pulse intensities (Behroozpour et al., 2017). Near-infrared (NIR) light is most commonly used for this purpose, typically over wavelengths of 900–1,100 nm (270–330 THz) due to the low cost of lasers operating in this wavelength range and lower energy density than the visible spectrum (Li et al., 2022). The laser wavelength is a critical factor in determining the sensor's performance, as it influences the interaction with water and suspended particles. Figure 2 illustrates the spectral character of clear still water as a function of laser wavelength and the influence of suspended sediment concentration on reflectance in rivers (Lednev et al., 2013; Milan et al., 2010; Paul; Buytaert; Sah, 2020).

3.4.1 Optical Physics of LiDAR-Water Interaction

Understanding the physics of NIR LiDAR interaction with water surfaces is essential for interpreting sensor performance. When a laser pulse strikes a water surface, two distinct optical regimes govern the returned signal: specular reflection (Fresnel regime) and volume backscatter (scattering regime) (Hecht, 2017).

3.4.1.1 Fresnel Reflectance at the Air-Water Interface

For an air-water interface at normal incidence, the specular reflectance R is governed by the Fresnel equations (Hecht, 2017):

$$R = \left| \frac{n_1 - n_2}{n_1 + n_2} \right|^2 \tag{1}$$

where $n_1 \approx 1.0$ (air) and $n_2 \approx 1.33$ (water). Applying Equation (1), this yields a specular reflectance of approximately 2%, meaning 98% of the incident optical energy enters the water column. In clear water, this transmitted energy is absorbed by H_2O molecules at NIR wavelengths (905 nm), resulting in minimal return signal—a phenomenon described as "signal void" in the literature (Tamari; Guerrero-Meza, 2016; Tamari et al., 2016).

3.4.1.2 Turbidity Enhancement via Mie Scattering

In turbid water containing suspended sediment particles (clays, silts), the optical interaction shifts from the Fresnel regime to the scattering regime. When particle diameter d is comparable to or larger than the wavelength λ (905 nm), Mie scattering dominates (Bohren; Huffman, 1998). The suspended solids act as diffuse reflectors, redistributing photon energy in all directions—a phenomenon known as the Tyndall effect. A portion of this scattered energy is directed back towards the LiDAR receiver.

The total received power P_r can be modeled as:

$$P_r = P_t \frac{A_r}{R^2} (\rho_{surf} + \rho_{vol}) \tag{2}$$

where P_t is transmitted power, A_r is receiver aperture, R is range, ρ_{surf} is surface reflectivity, and ρ_{vol} is the effective reflectivity contribution from turbidity-induced volume backscatter. This theoretical framework predicts that high sediment load—a proxy for flood conditions—can enhance the reliability of optical monitoring systems, as the volume backscatter term ρ_{vol} may exceed the surface reflection term ρ_{surf} (Tamari; Guerrero-Meza, 2016; Tamari et al., 2016; Paul; Buytaert; Sah, 2020).

Figure 2 – (a) Spectral character of clear still water as a function of laser wavelength (Lednev et al., 2013; Milan et al., 2010). (b) Influence of suspended sediment concentration (curves: units of mg L(-1)) in river upon reflectance (Paul; Buytaert; Sah, 2020; Milan et al., 2010)

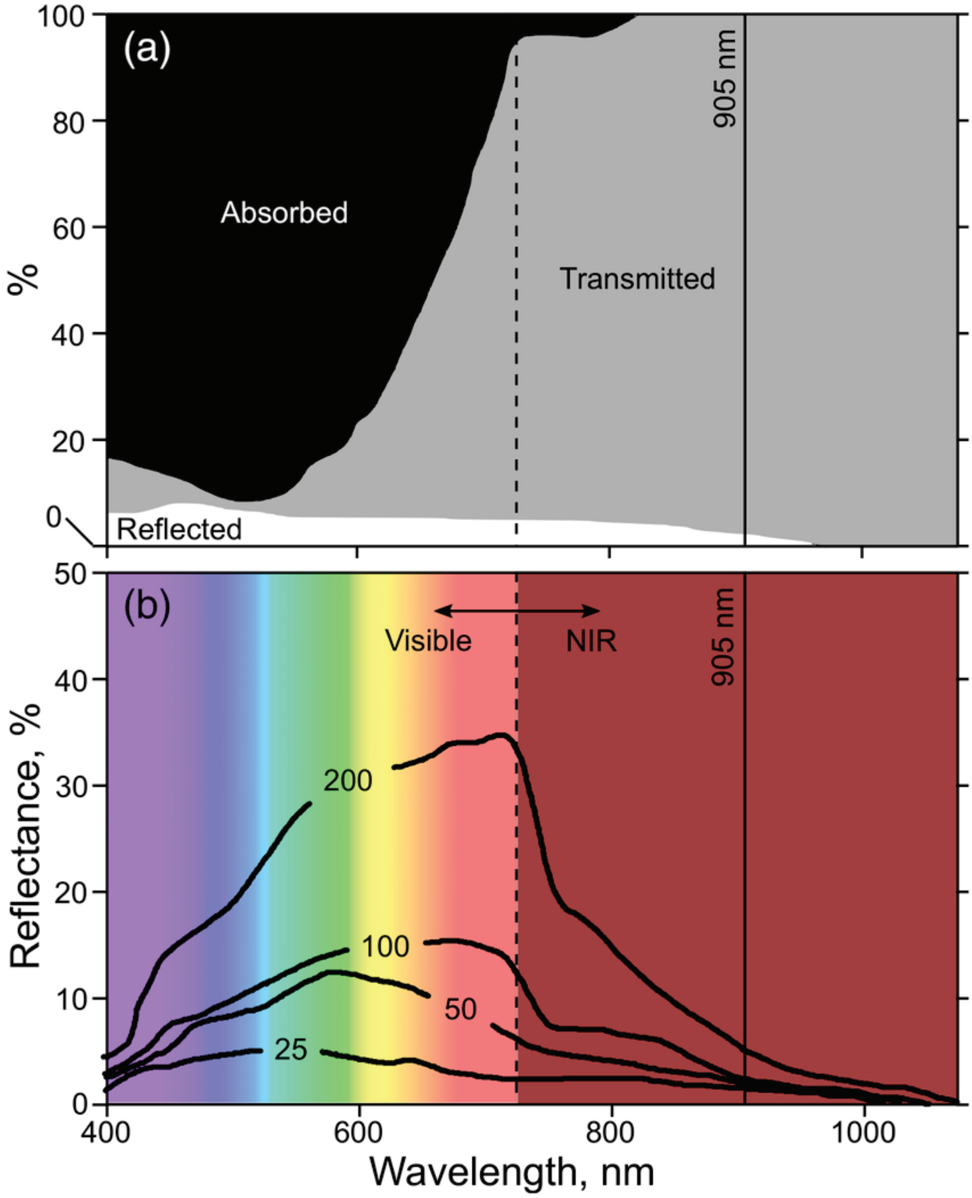

Source: (Lednev et al., 2013; Milan et al., 2010; Paul; Buytaert; Sah, 2020).

The three sensing schemes most commonly used in LiDAR sensors are: pulsed TOF (Time Of Flight), AMCW TOF, and FMCW (Li et al., 2022; Behroozpour et al., 2017). For this work the most important ones are the pulsed TOF and AMCW TOF, which are described below.

3.4.2 Pulsed Time of Flight

The pulsed TOF LiDAR works based on the time delay of an optical pulse emitted by the TX, reflected from the sensing object, and received by the RX. The sensing distance can be expressed using the following equation (Li et al., 2022).

$$d = \frac{c \cdot \Delta t}{2} \tag{3}$$

where d is the distance to the object in meters, c is the speed of light, and Δt is the time delay between emission and reception of the optical pulse in seconds.

3.4.3 Amplitude Modulated Continuous Wave Time of Flight

AMCW TOF LiDAR uses a continuous wave laser that is modulated in amplitude. The phase difference between the transmitted and received signals is measured to determine the distance to the object. The distance can be calculated using the following equation (Li et al., 2022).

$$d = \frac{c \cdot \Delta\phi}{4\pi f} \tag{4}$$

where d is the distance to the object in meters, c is the speed of light, $\Delta\phi$ is the phase difference between the transmitted and received signals, and f is the modulation frequency in Hz.

3.4.4 Practical Implications for Water Surface Detection

The choice of ToF technique, beam pattern, and environmental protection has significant practical implications for water level monitoring. Water surfaces present challenging conditions for optical sensors due to their low reflectivity at near-infrared wavelengths, as illustrated in Figure 2.

3.4.4.1 Beam Pattern: Spot vs. Line

Commercial LiDAR sensors implement two fundamentally different beam patterns:

- **Spot beam sensors** (e.g., 2-3° field of view) concentrate optical energy into a tight point, maximizing returned signal strength from a specific location. These are ideal for fixed-point distance measurement such as water level monitoring.
- **Line beam sensors** (e.g., 14° × 1° field of view) project optical energy across a wide angle, designed for obstacle detection and scanning applications. The dispersed energy results in weaker returns from any single point, and the sensor averages distance across the entire line width.

For water level monitoring in stilling wells or pipes, line beam sensors may produce erroneous readings due to multipath interference from sidewalls. However, over open water surfaces, line beam geometry offers a theoretical advantage through **spatial integration**. A spot beam interrogates a small footprint (e.g., 10 cm diameter at 4 m). If the water surface is rippled by wind or flow, the local facet angle of the wave within that small spot may exceed the critical angle for signal return, deflecting the specular reflection away from the sensor and causing signal dropouts.

In contrast, a line beam interrogates a much larger spatial extent (e.g., 100 cm length at 4 m). Even if a majority of wave facets along the line deflect the beam away, statistically, a percentage of the surface will be normal to the incident beam or provide sufficient backscatter. The sensor's internal processing integrates photon returns across the entire line array, effectively performing a hardware-level spatial averaging. This acts as a **spatial low-pass filter**, smoothing out high-frequency noise caused by capillary waves without requiring software post-processing. This theoretical advantage of line beam geometry over rippled water surfaces warrants empirical validation.

3.4.4.2 Temperature Effects on LiDAR Accuracy

Temperature variations affect ToF LiDAR measurement accuracy through two primary mechanisms (Alhashimi; Varagnolo; Gustafsson, 2015). First, the nominal wavelength of laser diodes shifts with temperature—for example, from 905 nm at 25°C to 907.8 nm at 35°C (a 2.8 nm shift). Since ToF calculations assume a constant wavelength, this shift introduces systematic distance bias of approximately 3.1 mm per meter of range for every 10°C temperature change.

Second, laser scanners require thermal stabilization after power-on, with warm-up periods of up to 30 minutes to reach equilibrium. During this warm-up phase, measurement drift can be substantial: experiments on industrial ToF LiDAR (SICK LMS 200) demonstrated 40 cm measurement difference at 6 m distance between device temperatures of 21°C and 45°C (Alhashimi; Varagnolo; Gustafsson, 2015).

3.5 ULTRASONIC SENSORS

Ultrasonic sensors estimate distance by transmitting high-frequency acoustic waves and measuring the echo delay. Common models like the HC-SR04 and JSN-SR04T are widely used in water level monitoring applications (MasoudiMoghaddam; Yazdi; Shahsavandi, 2024) and in citizen science and educational contexts (Bresnahan et al., 2023) due to their low cost and simplicity.

The basic principle of ultrasonic distance measurement is based on the time of flight (TOF) of sound waves. The sensor emits a high-frequency sound wave, which travels through the air, reflects off an object, and returns to the sensor. The distance d is derived from the total flight time t:

$$d = \frac{v_{sound} \times t}{2} \tag{5}$$

where v_{sound} is the speed of sound in air. A critical theoretical consideration is that the speed of sound varies as a function of air temperature. The speed of sound v in air varies with absolute temperature T (in Kelvin) according to the theoretical relationship:

$$v \approx 331.5\sqrt{\frac{T}{273.15}} \approx 331.5 + 0.607 \cdot \theta \tag{6}$$

where θ is the temperature in degrees Celsius (Wong; Embleton, 1985). This temperature dependence introduces a systematic bias of approximately 1.8 mm per meter of range per degree Celsius if left uncompensated. In field conditions, Panagopoulos et al. (2021) observed that this effect manifests as distinct diurnal fluctuations in ultrasonic readings correlated with air temperature changes, even when the actual water level remained stable. A co-located temperature sensor can compensate for this drift by adjusting the speed of sound in real time.

In addition to temperature, wind introduces a second source of systematic error for ultrasonic sensors. Wind velocity vectorially adds to the speed of sound, causing directional measurement bias: crosswinds perpendicular to the beam path cause overestimation, while headwinds or tailwinds cause underestimation (Tarulescu, R.; Tarulescu, S., 2014). Unlike temperature drift, wind-induced errors are transient and difficult to compensate without an anemometer, making them a practical concern for bridge-mounted sensors in exposed river valleys.

3.6 WIRELESS SENSOR NETWORK (WSN)

WSN (Wireless Sensor Network) are considered a promising alternative to complement conventional monitoring processes. These networks are relatively affordable and allow measurements to be taken remotely, in real-time and with minimal human intervention (Pule; Yahya; Chuma, 2017). A WSN is composed of spatially distributed autonomous nodes that monitor physical or environmental conditions. These nodes typically consist of a sensing unit, processing unit, communication interface, and power source. Natural disaster monitoring is very complex and imposes a number of challenges mainly due to huge scales,uncertainties, and harsh environments.

Each such sensor network node typically has many parts: a radio transceiver with an internal antenna or connection to an external antenna, a microcontroller, an electronic circuit for interfacing with the sensors and an energy source, usually a battery or an embedded form of energy harvesting (Yellampalli, 2021). An example architecture of a WSN is shown in Figure 3. The nodes are capable of collecting data from the environment, processing it, and transmitting it wirelessly to a base station or gateway for further analysis and visualization. A WSN can be single hop, where the nodes connect directly to the base station, or multi-hop, where the nodes can send information between themselves before reaching the base station (Yellampalli, 2021).

Figure 3 – Wireless Sensor Network architecture.

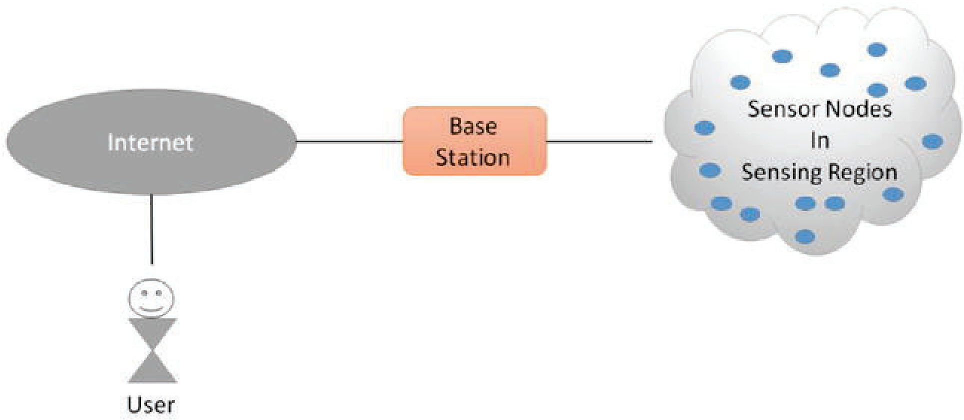

Source: (Yellampalli, 2021).

WSN-based natural disaster monitoring systems excel in terms of cost, speed of response, scalability and flexibility in contrast to conventional approaches (Chen et al., 2013). In general, disaster monitoring with WSN manifests a typical paradigm of data-intensive application upon low-cost scalable systems (Pule; Yahya; Chuma, 2017). In this work, the WSN architecture facilitates distributed hydrological data collection and centralized data aggregation through LoRa communication.

Network scalability analyses have shown that LoRaWAN capacity is bounded by collision probability, which increases non-linearly with the number of nodes and their Time on Air, limiting practical deployments to approximately 1000 devices per gateway under optimal conditions (Mikhaylov; Petäjäjärvi; Hänninen, 2018), as discussed in Chapter 2. Field deployments by Ragnoli et al. (2020) and Kabi, Kamucha, and Maina (2023) have validated that the star-of-stars topology is practical for river basin monitoring, where nodes can reliably transmit to gateways even in non-line-of-sight conditions typical of meandering river courses and dense riparian vegetation.

3.7 TIME-SERIES DATA AND ENVIRONMENTAL MONITORING

Time-series data represent sequential observations over time. In the context of water level monitoring, time-series analysis enables the detection of trends, anomalies, and correlations between environmental factors (Lozano et al., 2017). Basic statistical techniques, such as moving averages, root mean square error (RMSE (Root Mean Square Error)), and filtering, are applied to improve data reliability and reduce noise(Santana; Salustiano; Tiezzi, 2024).

The theoretical principles underlying statistical filtering techniques have been validated through field deployments. Kabi, Kamucha, and Maina (2023) demonstrated that raw sensor data in river environments is prone to significant noise from turbulence and debris, necessitating machine learning or statistical filtering for usable hydrological insights. The theoretical effectiveness of median filtering and outlier removal techniques has been validated through practical implementations, where these methods reduce noise from environmental factors such as surface turbulence, floating debris, and wind-induced wave action. Theoretical noise reduction principles, including moving averages and statistical outlier detection, have been empirically validated as essential components for converting raw sensor readings into reliable hydrological data suitable for flood prediction and early warning systems.

3.8 ISO 4373: HYDROMETRY — WATER-LEVEL MEASURING DEVICES

ISO 4373:2022 (International Organization for Standardization, 2022) is the international standard governing the specification and performance evaluation of water-level measuring devices used in hydrometry. It defines performance classes, typical device characteristics, environmental operating conditions, enclosure requirements, and installation guidelines. This standard provides the quantitative benchmarks against which the sensors evaluated in this work are assessed.

3.8.1 Performance Classes

The standard defines three performance classes for water-level measuring devices based on nominal uncertainty and resolution, as summarized in Table 4. These classes establish the accuracy thresholds that a device must satisfy for a given application.

Table 4 – ISO 4373 performance classes for water-level measuring devices.

Performance Class	**Nominal Uncertainty**	**Resolution**
Class 1	$< \pm 0.1\%$ of range	≤ 1 mm
Class 2	$< \pm 0.3\%$ of range	≤ 5 mm
Class 3	$< \pm 1.0\%$ of range	≤ 10 mm

Source: (International Organization for Standardization, 2022).

3.8.2 Typical Device Characteristics

Table 5 presents the typical uncertainty values for different types of water-level measuring devices as established by the standard. These benchmarks serve as a reference for evaluating whether a sensor performs within the expected range for its technology class.

Table 5 – ISO 4373 typical device characteristics for water-level measurement.

Device Type	**Typical Uncertainty (mm)**
Float-operated	2–5
Pressure transducer	5–10
Radar / laser (non-contact)	5–10
Ultrasonic through air	10–20
Bubbler gauge	5–15

Source: (International Organization for Standardization, 2022).

3.8.3 Environmental Requirements

The standard specifies environmental operating classes to ensure that devices are suitable for the climatic conditions at the deployment site. Temperature and humidity classes relevant to this work are:

- **Temperature Class 1**: +5°C to +40°C (temperate indoor environments).
- **Temperature Class 2**: −10°C to +45°C (moderate outdoor environments).
- **Temperature Class 3**: 0°C to +50°C (warm outdoor environments).
- **Temperature Class 4**: −25°C to +55°C (extreme outdoor environments).
- **Humidity Class 1**: 20–80% relative humidity (non-condensing).
- **Humidity Class 2**: 10–90% relative humidity (non-condensing).

Devices deployed in the field must operate within at least one of these classes. The subtropical climate of the deployment region in this work (typical temperatures 15–35°C, humidity 70–90%) is compatible with all four Temperature Classes and falls within Humidity Class 2. Temperature Class 3 (0–50°C) is adopted as the reference class because it represents the narrowest standard range that encompasses the observed field conditions while providing adequate margin for extreme summer temperatures, which can occasionally exceed 40°C in the Vale do Itajaí region.

3.8.4 Enclosure and Protection Requirements

The standard requires that the protection level of sensor enclosures be stated according to IEC 60529 (Ingress Protection ratings). For outdoor hydrological deployments, sensors must withstand exposure to rain, humidity, and potential water splash, making ratings such as IP65 (dust-tight, protected against water jets) or IP67 (dust-tight, protected against temporary immersion) essential for long-term reliability.

3.8.5 Installation Requirements for Non-Contact Sensors

ISO 4373 establishes specific installation guidelines for non-contact water-level sensors (radar, laser, and ultrasonic devices):

The standard requires that the sensor be mounted on a stable, rigid structure to prevent measurement drift caused by vibration or structural movement. The sensor beam must be directed perpendicular to the water surface to ensure accurate distance measurement and maximize signal return. Furthermore, the vertical path between the sensor and the water surface must remain free from obstacles such as vegetation, structural elements, or debris that could cause false reflections or signal interference. Finally, a stable reference point must be established to convert distance measurements into water-level values relative to a known datum. These installation requirements ensure measurement consistency and comparability across different sites and sensor technologies.

3.9 SYNTHESIS OF THE THEORETICAL FRAMEWORK FOR THIS WORK

The previous sections have established the theoretical foundation for this project by detailing the key components of an IoT monitoring system. This includes WSN architectures for data collection, long-range communication, the ESP microcontroller as a low-cost processing node, and the operational principles of both LiDAR and ultrasonic sensors. This framework provides the direct context for the central objective of this work: to conduct a practical, comparative evaluation of these sensor technologies for river level monitoring.

4 METHODOLOGY

This chapter presents the methodological framework for designing, evaluating, and deploying a sensor node and WSN for river level monitoring. The methodology is structured to be general and replicable, enabling its application to similar environmental monitoring contexts regardless of the specific hardware or software components selected.

4.1 SYSTEM ARCHITECTURE DESIGN

An environmental monitoring system for river level measurement is built around a modular WSN architecture. The conceptual architecture for such a system comprises four key subsystems, each of which can be independently configured and adapted for the deployment context.

The **Data Acquisition Subsystem** comprises the non-contact distance sensors and their interface circuitry, managed by the Processing Subsystem's microcontroller. It is responsible for capturing environmental data using sensors such as LiDAR or ultrasonic types, selected based on range, precision, and environmental resilience requirements. Non-contact sensing is preferred for hydrological applications because it avoids the mechanical wear, biofouling, and maintenance issues associated with contact-based instruments such as float gauges and pressure transducers (Mohindru, 2023). The selection of specific sensor technologies is driven by the deployment context, including the measurement range to the water surface, expected environmental conditions (temperature, humidity, solar irradiance), and the target accuracy defined by international standards such as ISO 4373:2022 (International Organization for Standardization, 2022).

The **Processing Subsystem** consists of a low-power microcontroller that serves as the core of each sensor node, reading sensor data, executing system logic (including temperature compensation algorithms for ultrasonic measurements), managing power states through deep sleep cycles, and preparing data for transmission. The microcontroller must support the communication interfaces required by the selected sensors (e.g., UART for LiDAR, GPIO for ultrasonic trigger/echo) while providing sufficient processing capability for real-time data acquisition and local filtering.

The **Communication Subsystem** provides a wireless communication interface that transmits processed data to a centralized gateway. For remote environmental applications where long transmission distances and minimal power consumption are essential, LoRa/LoRaWAN modules offer an optimal balance of range, energy efficiency, and infrastructure simplicity. Field measurements confirm ranges up to 11 km in rural environments and energy consumption of 82.2 µWh per message (Orlovs et al., 2025). The star-of-stars network topology characteristic of LoRaWAN enables direct communication between sensor nodes and gateways without the complexity of mesh routing protocols (Mikhaylov; Petäjäjärvi; Hänninen, 2018).

The **Power Management Subsystem** ensures operational autonomy in remote deployments through rechargeable batteries combined with aggressive power management strategies. Deep sleep modes reduce standby consumption to the microampere range, while duty-cycling the active measurement and transmission periods according to validated energy models (Casals et al., 2017; Bouguera et al., 2018) enables multi-month battery life without external recharging.

Figure 4 illustrates the generalized system architecture, showing the data flow from sensor acquisition through wireless communication to centralized storage and visualization.

Figure 4 – Generalized system architecture for river level monitoring, showing the four subsystems and end-to-end data flow.

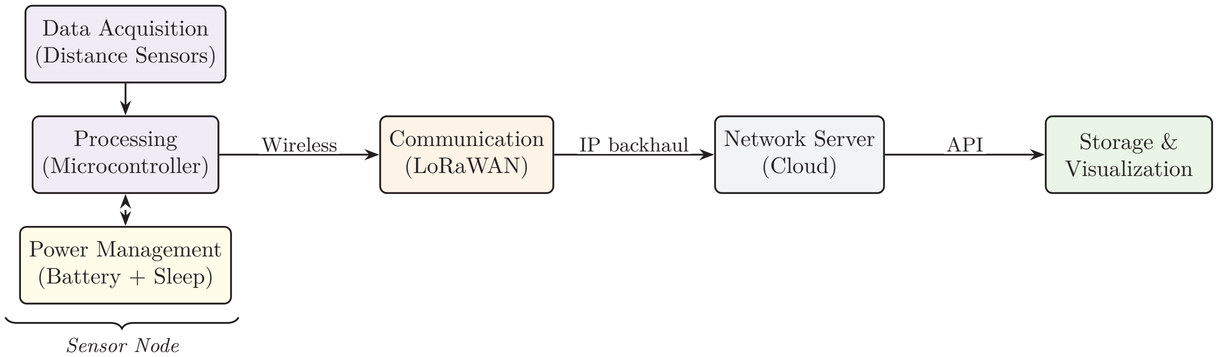

Source: The author.

The modular design allows each subsystem to be independently configured and adapted. Sensor selection is driven by the deployment context (measurement range, environmental conditions, target accuracy), while the communication and power subsystems are dimensioned according to transmission frequency, distance to gateway, and desired operational lifetime.

4.2 EVALUATION STRATEGY

The evaluation strategy follows a three-phase approach designed to progressively validate system components from individual sensor characterization through integrated system testing to real-world deployment. In embedded systems engineering terminology, Phase 1 corresponds to unit-level testing of individual sensor components, while Phase 2 corresponds to integration testing of the assembled system. This phased approach is consistent with the methodology adopted by Kabi, Kamucha, and Maina (2023) in their 18-month river monitoring deployment and by Ragnoli et al. (2020) in their autonomous flood monitoring system, where laboratory validation precedes field installation to minimize deployment risks. Table 6 summarizes the three evaluation phases, their objectives, and expected outputs.

Table 6 – Summary of the three-phase evaluation methodology.

Phase	Objective	Tests	Expected Outputs
1	Controlled environment sensor evaluation	Distance range, precision/accuracy, rain interference, water surface detection	Baseline sensor characterization, operational limits, sensor selection
2	System integration and validation	Node assembly, network validation, integrated sensor testing	Validated communication pipeline, end-to-end data flow
3	Field deployment and validation	Bridge-mounted deployment, adaptive transmission, multi-day operation	Real-world performance data, ISO 4373 classification, battery life estimates

Source: The author.

4.2.1 Phase 1: Controlled Environment Sensor Evaluation

The first phase evaluates sensor performance under controlled conditions before network integration. Before evaluation, each sensor is powered on and allowed a brief stabilization period until consistent readings are observed. Reference distances are established using a tape measure, which provides the ground truth for accuracy assessment with an estimated uncertainty of 20–30 mm. The objective is to systematically characterize each candidate sensor across four dimensions that are critical for hydrological monitoring applications.

Distance range tests establish the operational limits of each sensor technology by comparing measurements at multiple known distances against a tape measure reference. The test distances are selected to span the expected range of bridge-to-water distances at the planned deployment sites, as well as to identify the maximum reliable operating range of each sensor. This approach follows the methodology employed by Santana, Salustiano, and Tiezzi (2024), who validated LiDAR sensors at multiple fixed distances before field deployment.

Precision and accuracy tests collect multiple readings at each fixed distance to evaluate measurement consistency, quantified by standard deviation and correctness, quantified by MAE and RMSE against reference measurements.

Environmental interference tests assess sensor resilience under adverse weather conditions, including natural and simulated precipitation, to determine robustness for outdoor deployment. Rain can affect ultrasonic sensors through acoustic scattering from water droplets (Sumi et al., 2024), while LiDAR sensors experience signal attenuation through Mie scattering, though even heavy rainfall reduces detection range only modestly at the short distances typical of bridge installations (Goodin et al., 2019). Solar irradiance is also evaluated as a factor for LiDAR sensors, since ambient near-infrared radiation can overwhelm the sensor's photodetector and reduce the signal-to-noise ratio.

Water surface detection tests evaluate sensor behavior on low-reflectivity water surfaces under both clear and turbid conditions, following the methodology proposed by Tamari and Guerrero-Meza (2016) and Tamari et al. (2016). This test is critical for hydrological applications where the measurement target is the water surface itself, which presents challenging optical and acoustic properties compared to solid reference targets. Clear and turbid water conditions are tested separately to assess the influence of suspended sediment on sensor performance, as the Mie scattering enhancement predicted by theory (Bohren; Huffman, 1998) may improve LiDAR return signals in turbid conditions. Prior studies indicate that near-infrared LiDAR sensors require a minimum turbidity of approximately 700 NTU for reliable water surface detection (Jannata; Salam; Suhendi, 2021), and comparative evaluations of low-cost LiDAR sensors for liquid level monitoring have shown distance-dependent precision degradation that must be characterized empirically (Utepov et al., 2023).

Throughout all tests, candidate sensors are mounted on a common fixture to enable simultaneous measurements, eliminating temporal variations as a confounding factor. Ambient temperature and humidity are recorded alongside distance measurements using a dedicated environmental sensor, enabling post-hoc analysis of temperature effects on measurement accuracy, particularly for ultrasonic sensors whose speed-of-sound dependence on temperature introduces systematic bias without compensation (Equation (6)).

4.2.2 Phase 2: System Integration and Validation

The second phase integrates selected sensors with the complete communication stack and data management infrastructure. This phase validates that the individual sensor performance characterized in Phase 1 is preserved when the sensors are embedded within the complete system, and that the end-to-end data pipeline operates reliably.

Node assembly involves the development of sensor nodes combining the selected distance sensors with a microcontroller, communication module, and power management circuitry. The firmware implements data acquisition routines, local processing (including moving average filtering and speed-of-sound compensation for ultrasonic sensors), and wireless transmission via LoRaWAN.

Network validation encompasses verification of wireless connectivity, including join stability with the network server, uplink reliability, signal quality assessment (RSSI and SNR) from planned deployment locations, and end-to-end data flow from sensor to data storage. This validation ensures that the selected deployment sites have adequate gateway coverage before committing to field installation.

Integrated sensor testing repeats the environmental condition tests from Phase 1 (rain interference, water surface detection) with the complete integrated system to validate that sensor readings are correctly acquired, transmitted, and stored. This approach tests both sensor performance and system reliability simultaneously, identifying any integration-related issues that may not be apparent from component-level testing.

4.2.3 Phase 3: Field Deployment and Validation

The final phase deploys the integrated system in a real-world riverine environment to validate operational reliability under authentic conditions.The deployment strategy requires weatherproof enclosures to protect nodes against rain, humidity, and temperature extremes. The beam path must be perpendicular to the water surface and free from obstacles that could cause false reflections, in compliance with the installation requirements specified by ISO 4373:2022 for non-contact sensors (Section 3.8.5).

An adaptive transmission algorithm adjusts the interval between measurement-and-transmission cycles based on the rate of water level change detected between consecutive readings, following the three-level threshold approach established by Ma et al. (2017) for energy-efficient environmental monitoring. Since the node wakes from deep sleep, acquires a measurement, and transmits in a single duty cycle, the adaptive interval controls both the sampling and transmission rates simultaneously. Under stable base-flow conditions (change rate below 1 cm/hr), the system operates at a standard 15-minute interval, consistent with the USGS recommendation for routine hydrological monitoring (U.S. Geological Survey, 2024). During moderate hydrological activity (1–5 cm/hr change rate), the interval reduces to 5 minutes. Under conditions of rapid water level change (exceeding 5 cm/hr), the system increases to high-frequency 1–2 minute intervals to capture fast-moving flood events with maximum temporal resolution. Table 7 summarizes the adaptive sampling thresholds.

Table 7 – Adaptive transmission strategy: duty-cycle intervals based on percentage change between consecutive readings.

Condition	**Change Between Readings**	**Transmission Interval**
Stable base-flow	$< 1\%$ of distance	15 minutes
Moderate activity	1–3% of distance	5 minutes
Rapid change	$> 3\%$ of distance	2 minutes

Source: The author.

Expressing thresholds as a percentage of the measured distance rather than an absolute rate makes the algorithm self-normalizing: at greater sensor-to-water distances (e.g., 5 m), a 1% threshold corresponds to 50 mm, appropriately above the noise floor of longer-range sensors; at shorter distances (e.g., 1 m), the same threshold corresponds to 10 mm, providing proportionally higher sensitivity. The specific percentage values are validated against field deployment data in Section 6.3.3.

The field deployment evaluates measurement accuracy compared to reference distance measurements, transmission reliability and packet delivery rate, battery life under real operating conditions, and system resilience over extended deployment periods encompassing varying weather conditions.

Non-contact sensors measure the distance from the sensor to the water surface, requiring a conversion to obtain the river level. Given a reference distance d_{ref} recorded under a known baseline water level W_0, the instantaneous water level W is:

$$W = W_0 + (d_{\text{ref}} - d) \tag{7}$$

where d is the current measured distance. A decrease in d corresponds to a rising river level. When the sensor beam is not perpendicular to the water surface, the slant distance must be corrected by the installation angle θ:

$$W = W_0 + (d_{\text{ref}} - d)\cos\theta \tag{8}$$

For small angles ($\theta < 10°$), the cosine correction is less than 1.5% and may be negligible. Over long-term deployments, the baseline can be self-calibrated by setting $d_{\text{ref}} = d_{\max}$ (the maximum observed distance) and $W_0 = 0$, progressively reducing dependence on the initial manual calibration.

4.3 DATA MANAGEMENT AND ANALYSIS

Data received from the WSN is relayed to a persistent database via a backend service. Time-series data is cleaned and processed using statistical tools, and a visualization interface enables real-time monitoring and historical analysis.

The statistical analysis framework applies five primary metrics for sensor evaluation, each providing a complementary perspective on measurement quality.

The **Mean Absolute Error** (MAE) quantifies the average magnitude of measurement errors regardless of direction, providing an intuitive measure of overall accuracy. It is defined as:

$$\text{MAE} = \frac{1}{n}\sum_{i=1}^{n} |x_i - \hat{x}_i| \tag{9}$$

where x_i is the i-th measured value, $\hat{x}_i$ is the corresponding reference value, and n is the total number of measurements. The MAE treats all errors equally, making it suitable for assessing whether a sensor meets the absolute uncertainty thresholds defined by ISO 4373 performance classes (International Organization for Standardization, 2022).

The **Root Mean Square Error** (RMSE) provides a weighted measure of error magnitude that penalizes larger deviations more heavily than the MAE, making it sensitive to outliers and large measurement excursions:

$$\text{RMSE} = \sqrt{\frac{1}{n}\sum_{i=1}^{n}(x_i - \hat{x}_i)^2} \tag{10}$$

The RMSE is particularly useful for identifying sensors prone to occasional large errors, which may be acceptable in terms of mean accuracy but problematic for safety-critical flood monitoring applications.

The **Standard Deviation** (σ) characterizes measurement precision and repeatability by quantifying the dispersion of readings around their mean value:

$$\sigma = \sqrt{\frac{1}{n-1}\sum_{i=1}^{n}(x_i - \bar{x})^2} \tag{11}$$

where $\bar{x}$ is the arithmetic mean of the measurements. A low standard deviation indicates high repeatability, which is essential for detecting small water level changes over time. The use of the sample standard deviation (with $n - 1$ denominator) follows established statistical practice for finite sample sizes.

The **Percentage Error** expresses measurement deviation relative to the reference distance, enabling comparison across different measurement ranges:

$$\text{Error}(\%) = \frac{x_{\text{measured}} - x_{\text{reference}}}{x_{\text{reference}}} \times 100 \tag{12}$$

This metric is directly comparable to the ISO 4373 performance class thresholds, which are defined as percentages of the measurement range (e.g., $< \pm 1\%$ for Performance Class 3).

The **Success Rate** quantifies sensor reliability during field deployments as the proportion of valid readings to total measurement attempts:

$$\text{Success Rate} = \frac{n_{\text{valid}}}{n_{\text{total}}} \times 100\% \tag{13}$$

where n_{valid} is the number of readings within the expected measurement range and n_{total} is the total number of measurement attempts. This metric is critical for assessing operational reliability, as a sensor with excellent accuracy but low success rate may be unsuitable for continuous monitoring applications.

Peak Signal-to-Noise Ratio (PSNR) was not included in this framework because it is primarily used for image quality assessment, where a well-defined maximum signal value exists. For distance measurements with variable reference values, MAE and RMSE provide more directly interpretable accuracy metrics that are aligned with the ISO 4373 performance class thresholds used for sensor benchmarking in this work.

Quantifying measurement uncertainty from field data requires accounting for whether the measured quantity (river level) is stable or changing during the observation period.

Stable river level. When the river level is stable, the standard deviation of repeated measurements directly represents the random measurement uncertainty (σ), as all variation is attributable to sensor noise.

Changing river level. When the river level is changing, sensor noise must be isolated from the hydrological signal. A residual analysis is applied: a centered moving average is subtracted from each sensor's time series to extract the underlying trend. The standard deviation of the residuals (σ_{residual}) is then computed as a measure of random sensor noise independent of the actual water level change. When two sensors are co-located at the same measurement point, the standard deviation of their pairwise differences provides an independent combined uncertainty estimate. The per-sensor contribution is estimated as $\sigma_{\text{diff}}/\sqrt{2}$.

4.4 EVALUATION CRITERIA

Sensor performance is benchmarked against ISO 4373:2022 (International Organization for Standardization, 2022), detailed in Section 3.8, using four criteria:

1. **Performance class compliance**: measured uncertainty is compared against the three performance classes in Table 4. A sensor is considered suitable if it meets at least Performance Class 3 ($< \pm 1\%$ of range).
2. **Device characteristic benchmark**: measured uncertainty is compared against the typical values for non-contact devices in Table 5 (5–10 mm for radar/laser, 10–20 mm for ultrasonic through air).
3. **Environmental compatibility**: the deployment region's climate must fall within the temperature and humidity classes defined by the standard (Section 3.8.3).
4. **Installation compliance**: field deployments must satisfy the standard's requirements for non-contact sensors, including rigid mounting, perpendicular beam orientation, and obstacle-free measurement path (Section 3.8.5).

5 SYSTEM DESIGN AND IMPLEMENTATION

This chapter describes the application of the methodology to the specific context of river level monitoring in the Vale do Itajaí region, Santa Catarina, Brazil. It details the hardware and software components used, the integration of the sensor nodes with the LoRaWAN communication stack, and the end-to-end validation of the complete monitoring system. The experimental results from all three evaluation phases are presented in Chapter 6.

5.1 IOTEC LAB REGIONAL LORA NETWORK

This work was developed at the IoTec LAB of UNIVALI, within the scope of a FAPESC-funded regional environmental monitoring initiative. The project established a regional LoRa communication infrastructure designed to provide long-range, low-power connectivity for IoT applications in the Foz do Rio Itajaí region, serving as an experimental platform for urban sensing, smart cities, and environmental monitoring.

The IoTec LAB LoRa network consists of 20 strategically positioned antenna installation points distributed across eight municipalities: Itajaí, Navegantes, Balneário Camboriú, Camboriú, Itapema, Penha, Brusque, and Ilhota. The network uses a combination of 8 dBi and 5 dBi gain antennas, with placement defined through a technical coverage study to maximize signal reach and network efficiency. The resulting infrastructure provides estimated coverage of approximately 578,000 inhabitants, with the highest coverage ratios in Itajaí (61%), Navegantes (61%), and Balneário Camboriú (59%).

This regional infrastructure and the associated laboratory resources provided the foundation for the present work. The IoTec LAB supplied the hardware platform, a professional-grade Wisgate Edge Pro gateway.

5.2 HARDWARE AND SOFTWARE

5.2.1 Microcontroller and Development Boards

Two ESP32-based development boards with integrated LoRa transceivers (Section 3.3) were used: the Heltec WiFi LoRa 32 V2 and the LilyGo T-Beam V1.2 (AXP2101), both available within the IoTec LAB infrastructure (Section 5.1). The single-board integration of microcontroller and LoRa radio simplifies the hardware design and reduces potential points of failure for long-term outdoor deployments (Pires; Veiga, 2025). The LilyGo T-Beam V1.2's AXP2101 PMU with I2C interface provides programmable battery management, while the Heltec WiFi LoRa 32 V2 includes an OLED display (128×64) useful for field debugging. The LilyGo's onboard GPS module was not used in this project.

5.2.2 Sensors Evaluated

Multiple distance sensors were evaluated, representing both LiDAR and ultrasonic technologies. The scope of the sensor evaluation was guided by three criteria: suitability for non-contact water surface measurement, availability in low-cost commercial formats, and coverage of complementary sensing technologies to enable comparative evaluation.

The **TF02-Pro** is an industrial-grade, single-point TOF LiDAR sensor with a 3° spot beam and IP65 environmental protection rating (Benewake (Beijing) Co., Ltd., 2024c). According to its datasheet, the sensor offers an operating range of 0.1–40 m at 90% reflectivity (0.1–13.5 m at 10% reflectivity), with rated accuracy of ±5 cm at 0.1–5 m and ±1% at 5–40 m, repeatability of <2 cm (1σ), and 1 cm distance resolution. The optical system is explicitly designed for outdoor operation with ambient light immunity up to 100 kLux. The IP65 rating makes it suitable for long-term field deployment without additional weatherproofing, following the approach of Santana, Salustiano, and Tiezzi (2024) who evaluated similar low-cost LiDAR sensors for water level measurement.

The **TF-Nova** is a pulsed TOF LiDAR sensor with a 14° × 1° wide line beam, designed primarily for obstacle detection and presence activation (Benewake (Beijing) Co., Ltd., 2024b). Its datasheet specifies an accuracy of ±5 cm and repeatability of <1 cm (1σ) within the 0.1–4 m range, with 1 cm distance resolution. Detection range varies significantly with ambient light: ≥14 m at 0 kLux drops to ≥7 m at 100 kLux (90% reflectivity), and ≥13 m to ≥4 m (10% reflectivity). This sensor was included following a recommendation from the manufacturer (Benewake) via direct email communication, who suggested that the wide line beam geometry may improve detection reliability over water surfaces by averaging reflections across a larger spatial extent.

The **TF-Luna** is an entry-level LiDAR sensor with a 2° spot beam, indoor range up to 8 meters, and poor outdoor performance (below 3 m at 100 kLux). It was included as a reference for comparison with the TF02-Pro, sharing similar spot beam geometry but lacking the TF02-Pro's outdoor-optimized optics.

The **JSN-SR04T** is a waterproof ultrasonic sensor with IP67 rating, detection range from 23 cm to 600 cm, a stated accuracy of ±1 cm, and a wide beam angle (±37.5°) (Microsonic Systems, 2023). The module operates at 40 kHz and supports both pulse-echo (ping) and serial communication modes. Ultrasonic sensors have been widely validated for water level monitoring, with Panagopoulos et al. (2021) demonstrating their viability in urban stream environments and Mohammed et al. (2019) achieving sub-centimeter accuracy in tank-level applications. The JSN-SR04T's waterproof construction eliminates the need for additional enclosure design for the transducer.

The **HC-SR04** is a basic prototyping ultrasonic sensor with range up to 4 meters, included for comparison with the waterproof JSN-SR04T to assess the impact of IP67 construction on measurement performance.

Finally, the **DHT11** temperature and humidity sensor serves a dual purpose: it provides per-reading temperature data for speed-of-sound compensation in ultrasonic distance calculations (Equation (6)), following the speed-of-sound temperature relationship established by Wong and Embleton (1985), and it records ambient environmental conditions (temperature and humidity) that are transmitted alongside distance measurements for environmental characterization and as supplementary indicators of weather events such as rain onset. The DHT11 was selected for its adequate accuracy for speed-of-sound compensation: its ±2°C uncertainty translates to approximately ±3.6 mm systematic error per meter of ultrasonic range, which is within the acceptable margin for the target Performance Class 3 (< ±1% of range). A higher-precision sensor (e.g., DHT22, ±0.5°C) would reduce this contribution but was not available in the laboratory.

Table 8 summarizes the technical specifications of all sensors included in the evaluation.

Table 8 – Technical specifications of the sensors evaluated in this work, as stated in manufacturer datasheets (Benewake (Beijing) Co., Ltd., 2024c, 2024b; Microsonic Systems, 2023).

Sensor	**Type**	**Technology**	**Range**	**Repeat. (1σ)**	**Accuracy**
TF02-Pro	LiDAR	ToF (VCSEL)	0.1–40 m	<2 cm	±5 cm (<5 m); ±1% (≥5 m)
TF-Nova	LiDAR	PToF (VCSEL)	0.1–14 m	<1 cm	±5 cm (0.1–4 m)
TF-Luna	LiDAR	ToF (VCSEL)	0.2–8 m	<1 cm	±6 cm (0.2–3 m)
JSN-SR04T	Ultrasonic	Acoustic ToF	0.23–6 m	—	±1 cm
HC-SR04	Ultrasonic	Acoustic ToF	0.02–4 m	—	±3 mm
DHT11	Temp/Hum.	Capacitive	0–50°C	—	±2°C

Source: Manufacturer datasheets (Benewake (Beijing) Co., Ltd., 2024c, 2024b; Microsonic Systems, 2023).

5.2.3 Communication Infrastructure

The gateway used for this work is the Wisgate Edge Pro (Figure 9), a LoRaWAN gateway available within the IoTec LAB infrastructure, fitted with a 3.0 dBi omnidirectional antenna to provide uniform coverage across the deployment area. In the OSI reference model, LoRa operates at the physical layer (Layer 1), providing the radio modulation, while LoRaWAN defines the MAC protocol (Layer 2) and network layer (Layer 3) functions including device addressing, ADR, and end-to-end encryption. The microcontroller nodes with integrated LoRa transceivers communicate with the gateway via the LoRaWAN protocol, and TTN (The Things Network) operates as the network and application server (Layers 3–7), providing device management, authentication, data routing, and integration with downstream services via MQTT.

5.2.4 Data Backend Architecture

The data infrastructure comprises three integrated components, detailed in Section 5.5: a REST API service developed in Go that receives and decodes sensor data from TTN via MQTT; a SQLite database for persistent storage; and a web-based visualization dashboard. SQLite was selected for its zero-configuration deployment, single-file portability, and suitability for the expected data volume (hundreds of readings per day). For a prototype system with a single gateway and fewer than ten nodes, SQLite provides sufficient performance without the operational overhead of a client-server database.

5.2.5 Embedded Software Design

The ESP32 platform includes an underlying real-time operating system (RTOS) that manages task scheduling and hardware abstraction. The application software executes as a single task within this environment, implementing a duty-cycled operation pattern designed for long-term battery-powered deployment. Upon waking from deep sleep, the microcontroller initializes the sensor peripherals, acquires a burst of 10 distance readings—a size selected as a trade-off between measurement robustness (sufficient for median filtering to reject up to 4 outlier readings from surface glint or transient interference) and power consumption (keeping the active measurement window under 2 seconds)—applies median filtering and averaging to reduce noise, and performs temperature compensation for ultrasonic measurements using the co-located DHT11 sensor readings (Equation (6)). The adaptive transmission algorithm then evaluates the rate of water level change between consecutive readings to determine the next duty-cycle interval, following the thresholds defined in Table 7. The processed measurement is encoded into a compact 12-byte LoRaWAN payload and transmitted to the gateway. After transmission, the node enters deep sleep mode until the next scheduled wake-up, reducing current draw to approximately 10 µA. Figure 5 illustrates the firmware execution flow.

Figure 5 – Sensor node software flowchart showing the data acquisition, adaptive transmission, and deep sleep cycle.

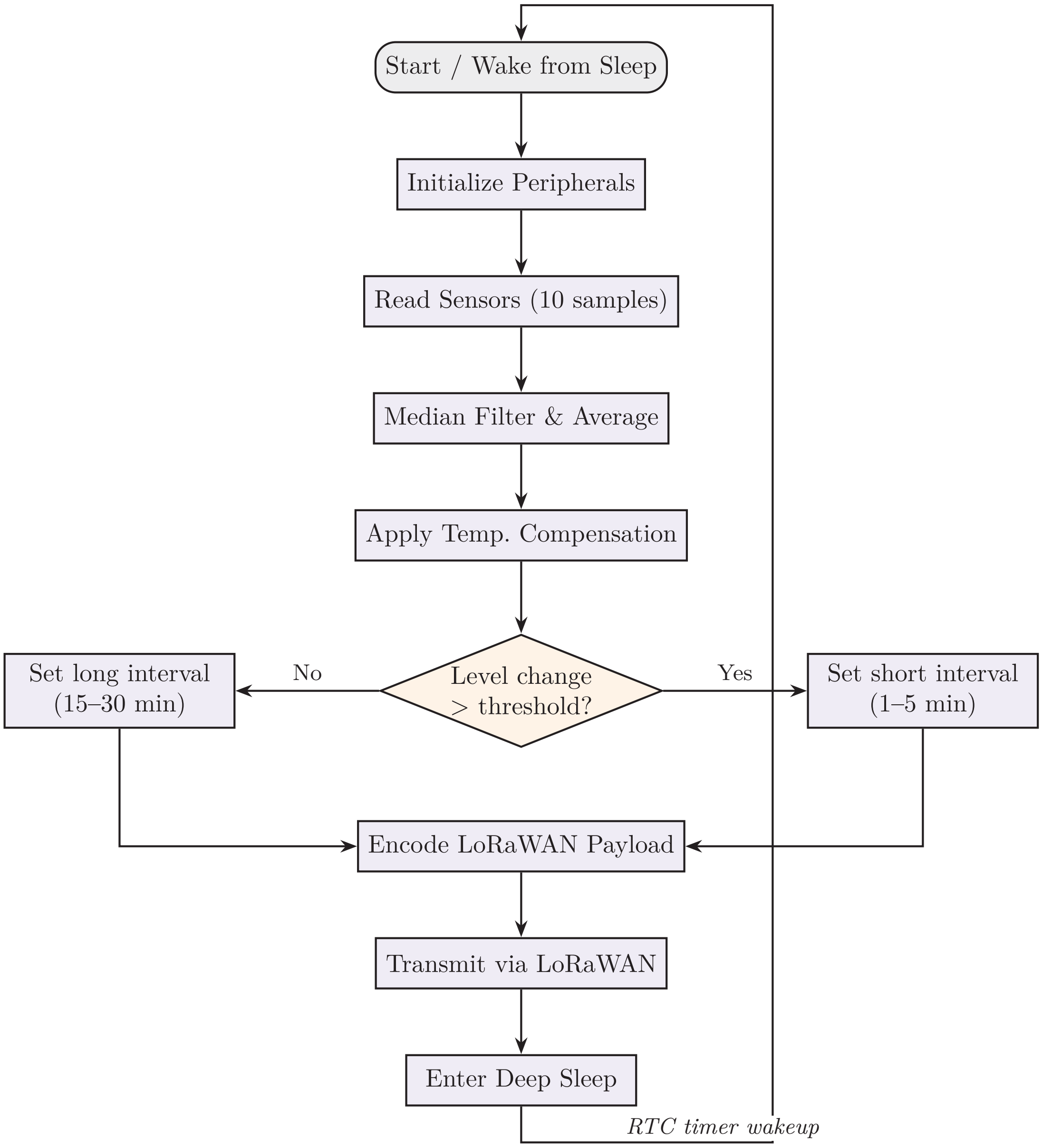

Source: The author.

5.3 NODE IMPLEMENTATION

Two sensor nodes were developed to enable comparative evaluation of different sensor and microcontroller combinations under identical deployment conditions. The sensor-to-board assignments were determined by hardware interface constraints—the TF-Nova's UART communication shared pins with the Heltec's OLED driver, requiring it to be paired with the LilyGo—rather than experimental design preference. To mitigate potential site-specific bias, the Phase 3 deployment placed both nodes at the same bridge (Bridge 2), enabling direct comparison under identical environmental conditions.

Node 1 (LilyGo T-Beam V1.2) interfaces with the TF-Nova LiDAR via UART, the JSN-SR04T ultrasonic sensor (TRIG: GPIO 13, ECHO: GPIO 12), and a DHT11 environmental sensor. The AXP2101 PMU provides battery management via I2C, enabling accurate battery voltage and charge level monitoring. An external battery shield with 5V boost converter powers the LiDAR sensor, which requires a higher supply voltage than the 3.3V provided by the microcontroller.

Node 2 (Heltec WiFi LoRa 32 V2) interfaces with the TF02-Pro LiDAR via UART and a DHT11 environmental sensor (GPIO 27). The same external battery shield architecture powers the board and sensors.

Both nodes implement deep sleep power management, achieving a current draw of approximately 10 µA in sleep mode compared to approximately 300 mA during active measurement and transmission. The LoRaWAN payload uses a compact 12-byte encoding that includes distance measurement, temperature, humidity, battery status, and signal strength, minimizing Time on Air and energy consumption per transmission (Casals et al., 2017).

5.4 LORAWAN NETWORK INTEGRATION

5.4.1 Connection Stability Testing

Both nodes were registered with TTN (The Things Network) and configured for AU915 frequency band with OTAA activation. Figure 6 shows the network topology. Stability tests confirmed consistent OTAA join success across multiple power cycles, reliable uplink transmission with acceptable RSSI and SNR values at the planned deployment locations, and no packet loss during extended testing periods lasting several hours.

Figure 6 – LoRaWAN network topology showing end devices, gateway, network server, and application backend.

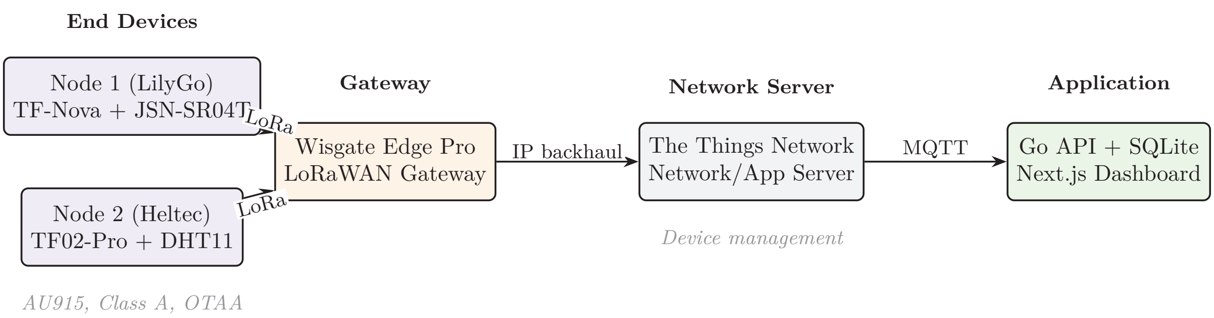

Source: The author.

5.4.2 Range Verification at Deployment Points

Uplink tests were conducted from the planned river deployment locations (bridge sites) to verify gateway coverage. All test locations showed adequate signal quality for reliable data transmission, confirming the planned sites are suitable for deployment. The

Heltec WiFi LoRa 32 V2 node experienced a few missed transmissions initially when in transport inside a box, but after improving the antenna placement it operated reliably at the bridges. Detailed signal quality metrics from the field deployments are presented in Section 6.3.1.6.

5.5 API BACKEND AND DASHBOARD IMPLEMENTATION

5.5.1 Go API Service

A REST API service was developed in Go to receive sensor data from TTN. The service connects to TTN via MQTT protocol, subscribing to uplink messages from all registered devices. Upon receiving a message, it automatically decodes the binary payload according to the 12-byte encoding schema and stores the reading in a SQLite database with full metadata including RSSI, SNR, gateway ID, and timestamps. The service also provides authenticated endpoints for data querying with filtering by device, date range, and signal type, enabling programmatic access for analysis scripts and the visualization dashboard.

5.5.2 Visualization Dashboard

A web-based dashboard was developed using Next.js, React, and Recharts to provide both real-time monitoring and historical analysis capabilities. The dashboard features interactive time-series charts for distance, battery level, and environmental parameters (temperature and humidity), device status tracking with connection status and uplink statistics, historical data analysis with configurable date ranges, and real-time monitoring capabilities that update automatically as new readings arrive. Figure 7 demonstrates the dashboard's multi-sensor comparison capability, displaying distance measurements from different sensors on a unified time-series chart. This visualization enables direct comparison of sensor behavior and facilitates identification of anomalies or drift patterns.

Figure 7 – Dashboard visualization showing simultaneous distance readings from multiple sensors over time.

Source: The author.

5.6 END-TO-END VALIDATION

The complete data pipeline was validated by tracing sensor readings through every component of the system: from the distance sensor acquisition, through LoRaWAN transmission to the Wisgate Edge Pro gateway, routing via TTN, delivery over MQTT to the Go API service, persistent storage in the SQLite database, and finally display on the visualization dashboard. Figure 8 illustrates the full system architecture from sensing to visualization. All rain interference and water tank tests reported in Chapter 6 were conducted with this integrated system, confirming both sensor performance and system reliability simultaneously.

Figure 8 – Implemented system architecture showing the specific hardware and software components that instantiate the generalized framework of Figure 4, from sensor nodes through the LoRaWAN communication stack to the visualization dashboard.

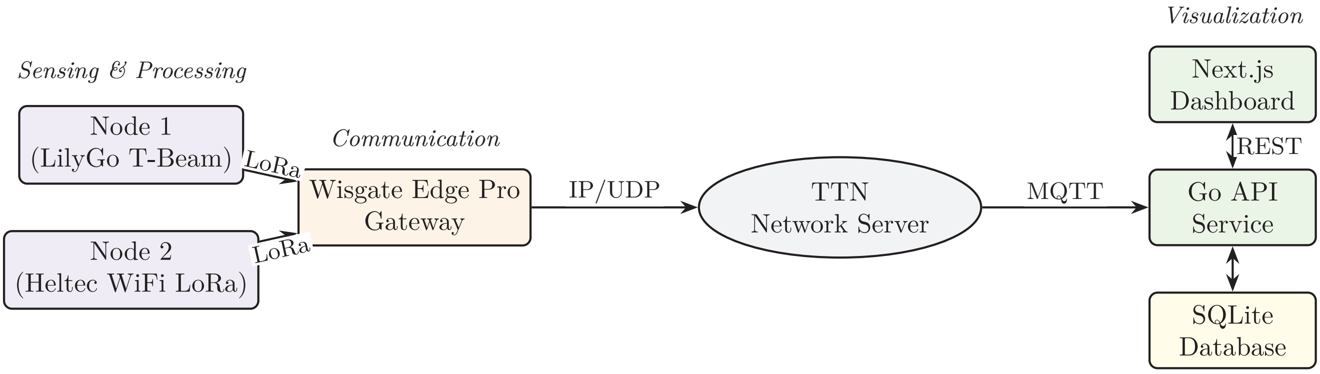

Source: The author.

5.7 BRIDGE DEPLOYMENT SETUP

In Phase 2 of the evaluation strategy, the sensor nodes were assembled into weatherproof plastic enclosures, with sensors mounted on 3D-printed adapter plates fitted to the bottom of each case to ensure a clear downward-facing beam path. Both nodes were registered on the LoRaWAN network and verified for uplink connectivity, and the Go API backend was configured to receive, decode, and store incoming sensor readings in the SQLite database.

Initial field testing was conducted from a bridge approximately 7 meters above a river surface to validate real-world performance. This river environment was in shade, with vegetation growing partially over the water and a river depth of approximately 20 cm during readings. The JSN-SR04T demonstrated significant susceptibility to interference from bridge structures, and the 7 meters was beyond its rated range. The TF-Nova LiDAR sensor failed some readings, likely due to the vegetation in the reading area (vines and bamboo leaves). The TF02-Pro had reliable readings in this environment.

5.7.1 Deployment Sites

Two bridges over rivers in the Vale do Itajaí region were identified for long-term deployment, in a region that experiences recurring flood events. Table 9 summarizes the site characteristics, and Figure 10 shows the deployment area with the LoRaWAN gateway position and the two bridge test sites.

Figure 9 – Wisgate Edge Pro gateway with 3.0 dBi omnidirectional antenna.

Source: The author.

Table 9 – Deployment site characteristics.

Site	Coordinates	Notes
Bridge 1	−27.1412, −48.9208	5.4 m above water; ultrasonic out of range
Bridge 2	−27.1413, −48.9184	4.1 m above water; all sensors within range
Gateway	−27.1418, −48.9190	Wisgate Edge Pro; ∼85 m from Bridge 2

Source: The author.

Figure 10 – Satellite view of the deployment area showing the LoRaWAN gateway and two bridge test locations.

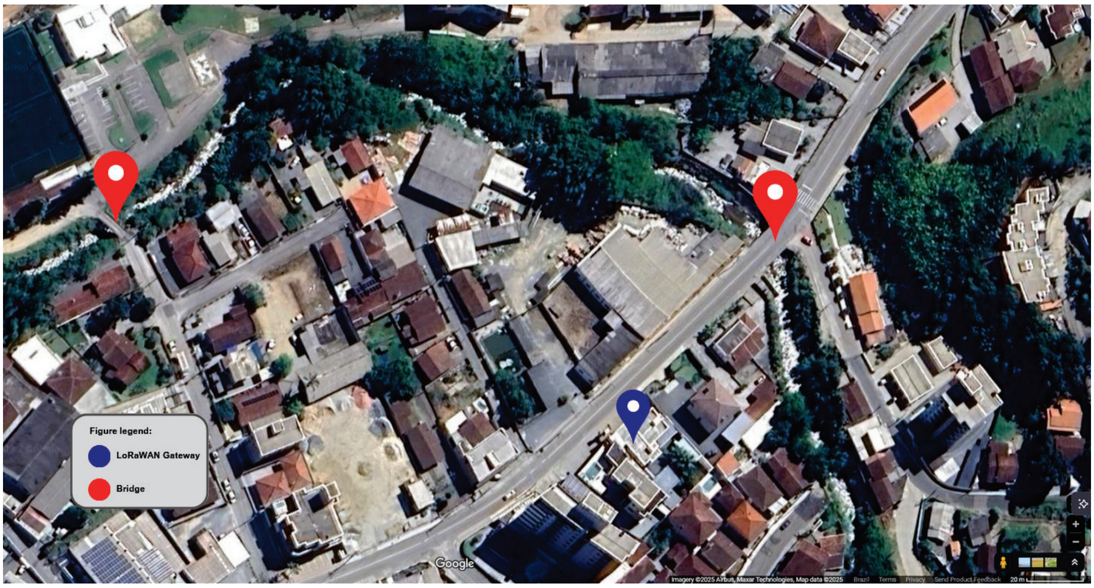

Source: Google Maps, adapted by the author.

Bridge 1 (Figure 11) has a guardrail-to-water distance of 5.4 meters (5400 mm). This height exceeds the JSN-SR04T's maximum range (6 m rated, approximately 4.5 m reliable), making it a LiDAR-only site.

Figure 11 – Bridge 1 test site: 5.4 meters from guardrail to water surface.

Source: The author.

Bridge 2 (Figures 12 and 13) has a guardrail-to-water distance of 4.1 meters

(4100 mm). This site is within the operating range of all sensors, enabling full comparative evaluation.

Figure 12 – Bridge 2 test site: 4.1 meters from guardrail to water surface.

Source: The author.

Figure 13 – Lateral view of Bridge 2 from the river margin, showing the bridge structure and surrounding environment.

Source: The author.

5.7.2 Node Installation

For the preliminary validation tests at the bridge sites, sensors were handheld against the bridge guardrails and multiple readings were taken at each location. Reference distances were measured using a tape measure. Water depth at the rivers was approximately 10 cm at both bridges during testing, and the water surface was clear. The validation results from these tests are presented in Section 6.2.

For the extended field deployment (Phase 3), both sensor nodes were mounted on the Bridge 2 railing, pointing downward toward the river surface at approximately 3.2 m distance. The nodes were housed in a shared plastic enclosure (Figures 15, 16, and 17) with additional plastic shielding above to protect against direct rain exposure. The Wisgate Edge Pro gateway was located within LoRaWAN range, and all data was transmitted via TTN and stored in the SQLite database through the Go API backend. Figure 14 illustrates the bridge deployment configuration. The deployment results are presented in Section 6.3.

Figure 14 – Bridge deployment configuration showing sensor node placement, distance to water surface, and protective enclosures.

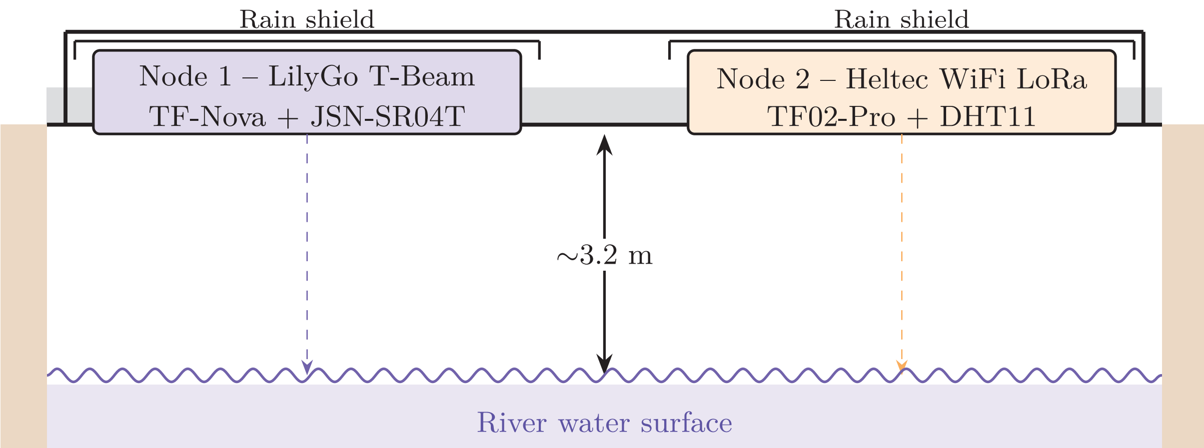

Source: The author.

Figure 15 – Interior of the sensor node enclosure showing both microcontroller boards and wiring.

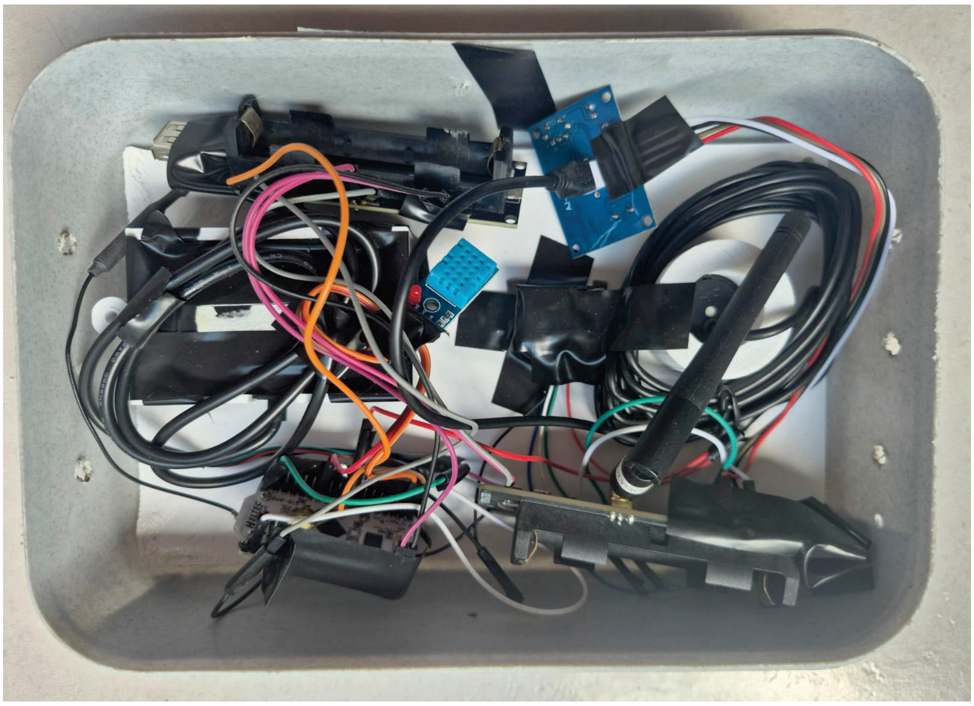

Source: The author.

Figure 16 – External top view of the sealed enclosure with protective shielding.

Source: The author.

Figure 17 – Bottom view of the enclosure showing the three downward-facing sensors: JSN-SR04T ultrasonic (left), TF-Nova LiDAR (center), and TF02-Pro LiDAR (right).

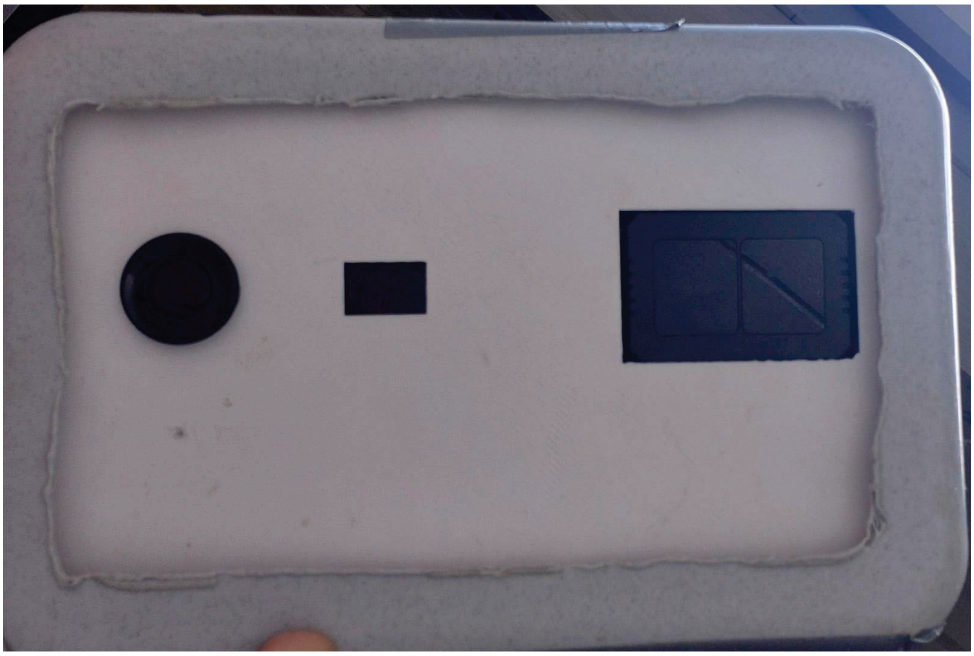

Source: The author.

6 EXPERIMENTAL RESULTS AND DISCUSSION

This chapter consolidates all experimental results obtained during the three evaluation phases: controlled environment testing (Phase 1), preliminary field testing (Phase 2), and extended field deployments under contrasting weather conditions (Phase 3). The results are presented in chronological order by evaluation phase, enabling a progressive assessment of the system from laboratory characterization through real-world operational validation.

6.1 PHASE 1: CONTROLLED ENVIRONMENT TESTING

The first phase focused on evaluating sensor performance under controlled conditions to establish baseline characteristics before network integration.

6.1.1 Preliminary Ultrasonic Sensor Evaluation

An initial evaluation compared two common low-cost ultrasonic sensors, the JSN-SR04T and HC-SR04, using ESP32-based development boards.

Readings were taken at four distances (210 cm, 350 cm, 460 cm, and 560 cm), verified using a measuring tape. These distances were selected to span the range of bridge-to-water distances observed at the planned deployment sites (approximately 4–6 meters) while also testing the operational limits of the ultrasonic sensors (manufacturer-rated maximum range of 4.0–4.5 meters). Following the ultrasonic measurement procedure described in Section 3.5, each measurement cycle activated the sensor trigger pin with a 10-microsecond high pulse, and the distance was calculated based on the echo response duration using the speed of sound compensated for ambient temperature (Equation (6)).

Table 10 presents the overall performance metrics for both ultrasonic sensors across all test distances. The JSN-SR04T demonstrated lower overall error (MAE 4.70 cm vs 8.38 cm) and better precision (Std. Dev. 3.01 cm vs 10.95 cm). The HC-SR04 excels only at short range (below 3 m), while the JSN-SR04T was the only sensor capable of operating reliably at 560 cm. Figure 18 illustrates the measurement distributions at each test distance.

Table 10 – Overall Performance Metrics (Valid Readings).

Sensor	MAE (cm)	RMSE (cm)	Std. Dev. (cm)
HC-SR04	8.38	9.07	10.95
JSN-SR04T	4.70	5.56	3.01

Figure 18 – Data from the ultrasonic sensors at different distances.

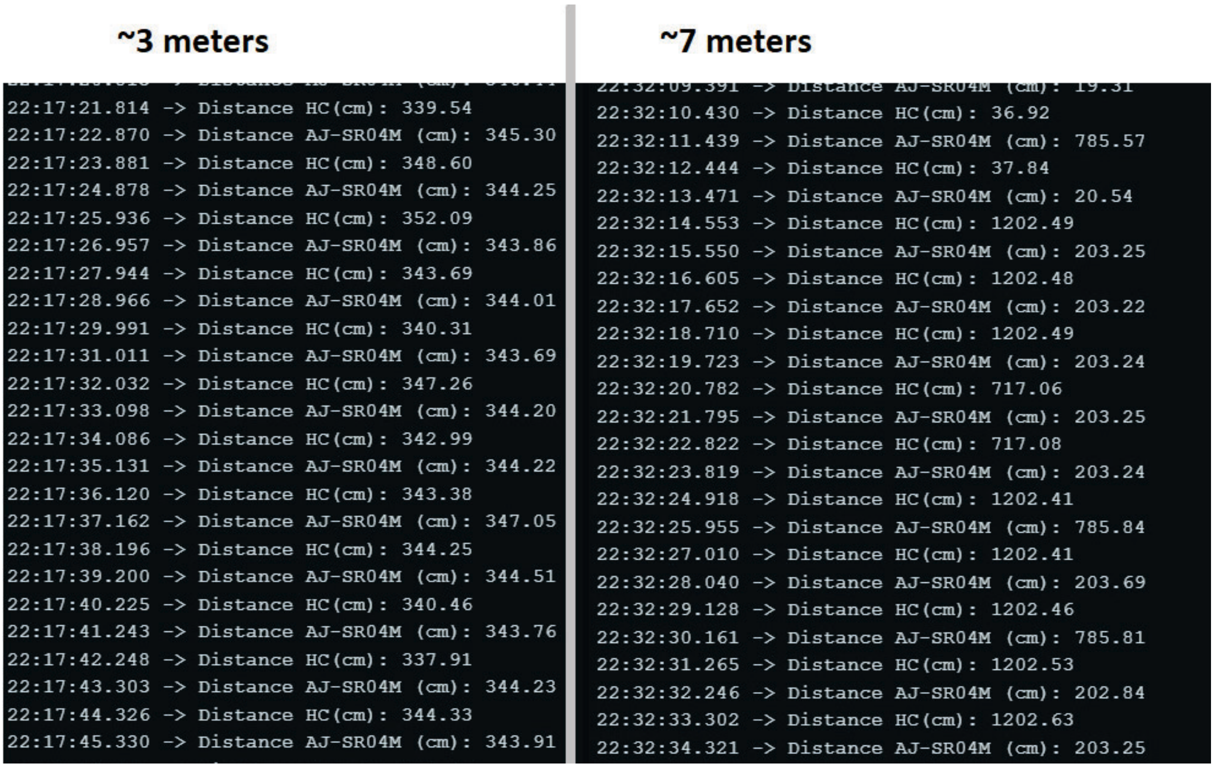

Source: The author.

6.1.2 Multi-Sensor Controlled Environment Evaluation

A comprehensive evaluation was conducted comparing all selected sensors under standardized conditions. A custom 3D-printed mounting board was fabricated to hold the JSN-SR04T ultrasonic, TF-Nova LiDAR and TF02-Pro LiDAR sensors in fixed positions for simultaneous measurements (Figure 19 shows from left to right: JSN-SR04T, TF-Nova and TF02-Pro, and above is the TF-Luna). The TF-Luna LiDAR was later added to the setup but not fixed for final deployment.

Tests were conducted in a parking lot at distances from 5 m to 25 m against a solid wall surface, with reference distances measured using a tape measure (Figure 20). It is important to note that these distance range tests were conducted against a solid, high-reflectivity target surface (concrete wall), not a water surface; the results therefore characterize each sensor's baseline distance accuracy and do not account for the lower reflectivity and dynamic nature of water surfaces, which are evaluated separately in the water surface detection tests (Section 6.1.3.2).

During the 5-meter tests, light rain was present; however, the rain had no significant impact on readings, as confirmed by the consistent measurements across all sensors at that distance (Table 11), consistent with the more detailed rain interference results presented in Section 6.1.3.1.

Figure 19 – Custom 3D-printed sensor mounting board with all sensors arranged for simultaneous distance measurements (from left to right: JSN-SR04T, TF-Nova and TF02-Pro, and above is the TF-Luna).

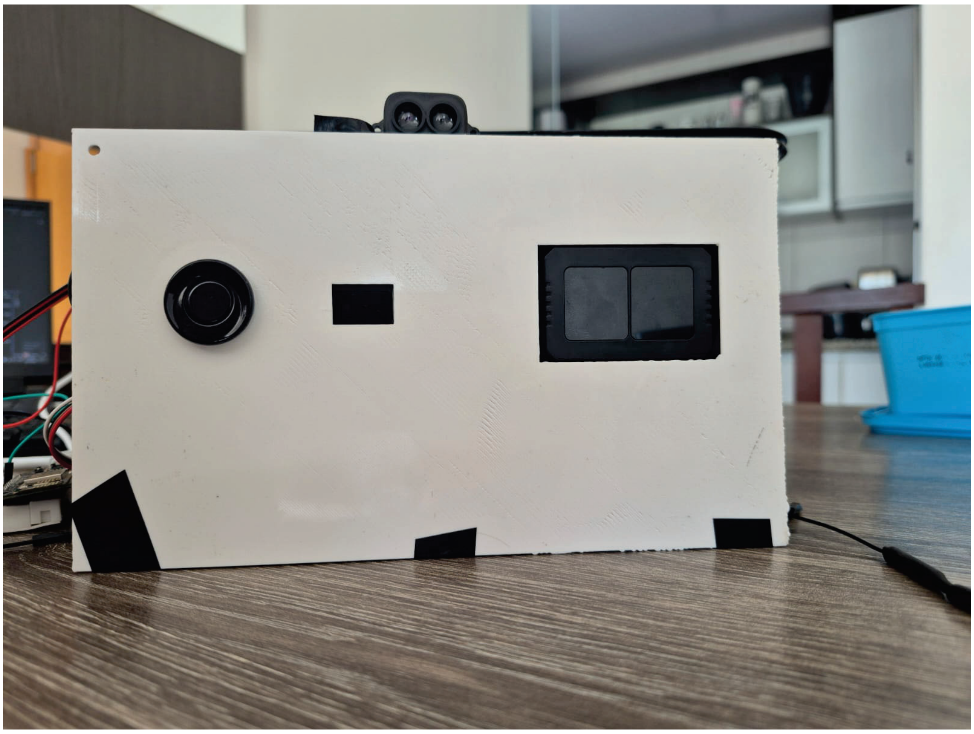

Source: The author.

Figure 20 – Parking lot test setup for controlled distance measurements.

Source: The author.

Throughout the controlled tests, ambient temperature and humidity were recorded using DHT11 sensors. During the range tests, average conditions were 32°C and 67% relative humidity. The ultrasonic sensor software applies per-reading speed-of-sound temperature compensation using the DHT11 readings (Equation (6)), with a fallback to a default 25°C if the DHT11 is unavailable. This environmental data is also stored in the SQLite database alongside distance measurements.

6.1.2.1 Distance Range Test Results

Table 11 presents the distance measurements from all sensors at reference distances from 5 m to 25 m. The TF02-Pro demonstrated the best overall performance, with reliable readings up to 21 meters, exceeding its manufacturer-specified outdoor range of 13.5 m at 100 kLux. The TF-Nova provided reliable measurements up to 13 meters but showed occasional interference from objects within its wide 14° line beam angle at longer distances.

The TF-Luna was limited to 7 meters and was excluded from subsequent tests due to its redundancy with the TF02-Pro and inferior outdoor performance. The JSN-SR04T ultrasonic sensor provided reliable readings only up to 5 meters, as expected from its manufacturer-specified maximum range of 4.5 m.

Table 11 – Multi-sensor distance measurements. Ambient conditions: 32°C, 67% RH (DHT11).

Reference (m)	**JSN-SR04T (cm)**	**TF-Luna (cm)**	**TF-Nova (cm)**	**TF02-Pro (cm)**	**Notes**
5.0	505	504	500	505	Light rain
7.0	440	731	716	713	TF-Luna limit
8.0	140	-1	826	823	
10.0	160	-1	1015	1010	
11.0	120	-1	1114	1109	
12.0	125	-1	1218	1212	
13.0	130	-1	1324	1318	TF-Nova limit
14.0	90	-1	-1	1503	
20.0	123	-1	-1	1993	
21.0	131	-1	-1	2142	TF02-Pro limit
25.0	111	-1	-1	-1	

Source: The author.

6.1.3 Environmental Condition Tests

These tests were conducted with the integrated LoRaWAN system, with sensor readings transmitted via LoRa and stored in the SQLite database through the Go API service.

6.1.3.1 Rain Interference Test

Measurements were taken at 5 meters under dry, natural rain, and simulated heavy rain (garden hose) conditions. Ambient conditions during testing were 26°C and 79% relative humidity (DHT11). Figure 21 shows the simulated rain test setup.

Figure 21 – Simulated rain test setup using garden hose to evaluate sensor resilience.

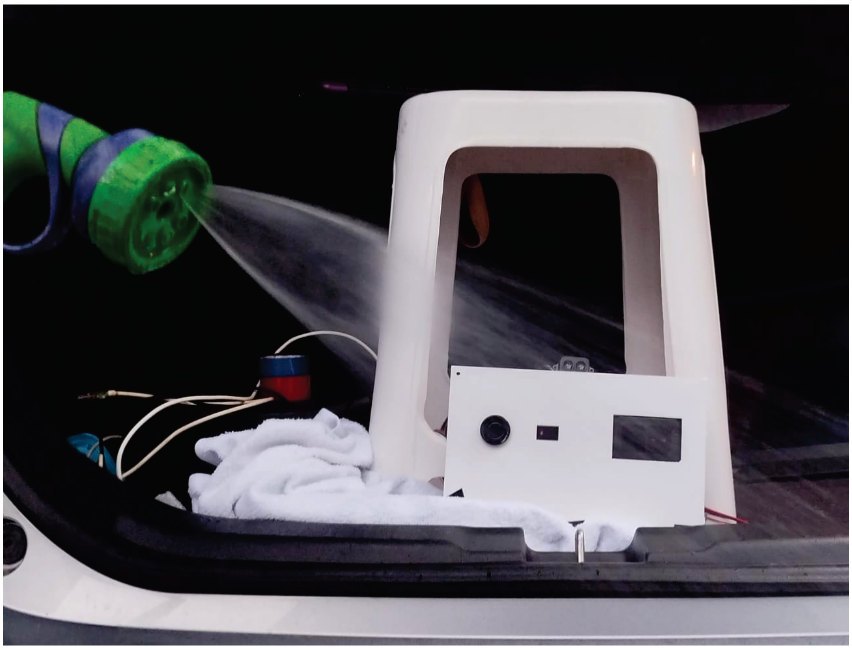

Source: The author.

As shown in Table 12, the TF-Nova detected the water spray at 45 cm due to its wide 14° line beam, while the JSN-SR04T and TF02-Pro (spot beam) correctly measured the wall distance. This demonstrates the TF-Nova's sensitivity to objects within its beam pattern and confirms that spot-beam and acoustic sensors are more resilient to rain interference when the rain is not directly in the narrow beam path.

The TF02-Pro's unaffected performance under simulated heavy rain is consistent with the LiDAR rain attenuation model of Goodin et al. (2019), who showed that even at 45 mm/h rainfall, LiDAR detection range is reduced by only approximately 6 meters, usally within the operational margin for bridge-mounted installations in the longer range LiDAR sensors. By contrast, Sumi et al. (2024) reported that ultrasonic sensors can suffer acoustic saturation under dense drizzle conditions, a failure mode not observed here at 5 m range but which may become relevant at longer distances or higher rainfall intensities.

Table 12 – Sensor performance at 5 m under rain conditions.

Condition	**JSN-SR04T (cm)**	**TF-Nova (cm)**	**TF02-Pro (cm)**	**Notes**
Dry (baseline)	492	500	495	Reference
Natural rain	491	499	506	Light/moderate
Simulated rain	490	45	495	Heavy spray

Source: The author.

6.1.3.2 Water Surface Detection Test

Tests were conducted at 1, 2, and 3 meters above a 1-meter diameter circular water tank (0.5 meters water depth) with both clear and murky (mud-mixed) water to simulate river conditions, following the turbidity-dependent evaluation approach motivated by Jannata, Salam, and Suhendi (2021) and Utepov et al. (2023), who established that near-infrared LiDAR performance varies significantly with water surface reflectivity. From a physics perspective, the ultrasonic sensor's mechanical (acoustic) waves reflect effectively from the water surface regardless of optical properties, while the LiDAR sensors' electromagnetic waves are subject to the low reflectivity of water at near-infrared wavelengths ($\sim$2%, Equation (1)). The fundamental advantage of acoustic sensing for water surface detection is therefore limited primarily by range, not by surface optical characteristics.

Reference distances were measured using a tape measure, which introduces a small uncertainty of approximately 2–3 cm. Single readings (no averaging) were taken at 10-second intervals. Ambient conditions were 26°C and 79% relative humidity (DHT11). Figure 22 shows the water tank test setup with both clear and murky water conditions.

Figure 22 – Water tank test: clear water (left) and murky water with mud (right).

Source: The author.

Table 13 presents the raw sensor readings for all three sensors at each distance and water condition. Tables 14 and 15 provide the corresponding statistical analysis for clear and muddy water conditions, respectively.

Table 13 – Raw sensor readings for water surface detection (values in mm).

Distance	**Condition**	**Sensor**	**Readings (mm)**
1 m	Clear	TF02-Pro	1070, 1060, 1080, 1060, 1090
		TF-Nova	1020, 1010, 980, 990, 1000, 990
		JSN-SR04T	986, 984, 985, 972, 983
	Muddy	TF02-Pro	1020, 1030, 1060, 970
		TF-Nova	1020, 1070, 990, 980, 1060
		JSN-SR04T	962, 967, 989, 966
2 m	Clear	TF02-Pro	2120, 2090, 2020, 2030
		TF-Nova	1890, 1920, 1930, 1870
		JSN-SR04T	1924, 1934, 1927, 1954
	Muddy	TF02-Pro	2060, 1950, 1960, 2050
		TF-Nova	1930, 1980, 2020, 2120, 2000
		JSN-SR04T	1976, 1991, 1993, 1937
3 m	Clear	TF02-Pro	2960, 2850, 2940, 2950
		TF-Nova	2880, 3220*, 2670*
		JSN-SR04T	2874, 2974, 2967, 2812
	Muddy	TF02-Pro	3010, 2970, 2970, 2960
		TF-Nova	3170, 2930, 2890, 2880, 2930
		JSN-SR04T	2935, 2864, 2958, 2953

Source: The author.

*TF-Nova readings at 3m showed interference from the tank edge due to the sensor's wide 14° line beam detecting outside the 1-meter diameter water tank.

Table 14 – Statistical analysis of water surface detection - Clear water.

Reference	**Metric**	**JSN-SR04T**	**TF-Nova**	**TF02-Pro**
1 m	Mean (mm)	982.0	998.3	1072.0
	Std. Dev (mm)	5.7	14.7	13.0
	Error (%)	-1.8	-0.2	+7.2
2 m	Mean (mm)	1934.8	1902.5	2065.0
	Std. Dev (mm)	13.1	26.3	47.3
	Error (%)	-3.3	-4.9	+3.3
3 m	Mean (mm)	2906.8	2923.3*	2925.0
	Std. Dev (mm)	71.8	275.4*	50.0
	Error (%)	-3.1	-2.6*	-2.5

Source: The author.

Table 15 – Statistical analysis of water surface detection - Muddy water.

Reference	Metric	JSN-SR04T	TF-Nova	TF02-Pro
1 m	Mean (mm)	971.0	1024.0	1020.0
	Std. Dev (mm)	12.5	40.9	37.4
	Error (%)	-2.9	+2.4	+2.0
2 m	Mean (mm)	1974.3	2010.0	2005.0
	Std. Dev (mm)	25.4	70.7	55.0
	Error (%)	-1.3	+0.5	+0.3
3 m	Mean (mm)	2927.5	2960.0	2977.5
	Std. Dev (mm)	43.8	113.1	22.2
	Error (%)	-2.4	-1.3	-0.8

Source: The author.

*TF-Nova 3m clear water statistics include interference readings; the wide beam angle is problematic in narrow tanks.

In terms of consistency, the JSN-SR04T ultrasonic sensor showed the lowest standard deviation across all tests (5.7–71.8 mm), demonstrating the most consistent readings. The TF02-Pro showed moderate consistency (13.0–55.0 mm), while the TF-Nova showed higher variability (14.7–275.4 mm). Regarding the effect of water turbidity, muddy water improved sensor performance across all LiDAR sensors. The TF02-Pro showed improved accuracy in muddy water (errors of +0.3% to +2.0%) compared to clear water (+3.3% to +7.2%), as shown in Tables 14 and 15.

Suspended particles provide improved surface reflectivity for LiDAR through the Mie scattering enhancement mechanism described in Equation (2). This finding is consistent with the turbidity threshold identified by Jannata, Salam, and Suhendi (2021), who demonstrated that near-infrared LiDAR sensors require a minimum turbidity of approximately 700 NTU for reliable water surface detection, with measurement error improving from 5.2% at 700 NTU to 2.6% at 900 NTU. The muddy water conditions in these tests likely exceeded this threshold, explaining the improved LiDAR performance. A systematic bias was also observed: the TF02-Pro tended to read slightly long at short distances (+7.2% at 1 m in clear water), while the JSN-SR04T consistently read slightly short (−1.3% to −3.3%). These systematic biases can be corrected through calibration. Finally, the TF-Nova's 14° line beam pattern caused detection of tank edges at 3 meters in the 1-meter diameter tank, resulting in outlier readings (3220 mm and 2670 mm), confirming the sensor's unsuitability for narrow or confined measurement scenarios.

6.1.4 Temperature Compensation Effectiveness

As noted in Section 6.3, the DHT11 sensor on Node 1 (LilyGo) failed during the field deployments, causing the JSN-SR04T ultrasonic sensor to operate with a fixed fallback temperature of 25°C for speed-of-sound compensation. To quantify the impact of this failure, a post-hoc correction was computed using the concurrent ambient temperature recorded by Node 2's (Heltec) working DHT11 sensor. For each ultrasonic reading stored with $v(25°\text{C})$, the corrected distance was calculated as $d_{\text{corrected}} = d_{\text{stored}} \times v(T_{\text{actual}})/v(25°\text{C})$, where $v(T)$ is given by Equation (6) and T_{actual} is the nearest heltec temperature reading.

Figure 23 shows the comparison across both field deployment days (206 paired readings). On the rainy day (February 7, mean temperature 28°C), the mean correction was 15 mm (0.50% of measured distance). On the sunny day (February 8, mean temperature 36°C), the correction increased to 61 mm (1.86%). The peak correction reached 68 mm during the warmest conditions. These results confirm that even a moderate temperature deviation from the fallback value introduces systematic bias that can exceed the ISO 4373 Performance Class 3 threshold ($< \pm 1\%$ of range), particularly under sunny conditions, reinforcing the importance of a functioning temperature sensor for ultrasonic compensation in outdoor deployments.

Figure 23 – Effect of DHT11 failure on JSN-SR04T temperature compensation during field deployment at Bridge 2. Upper panel: stored readings using fixed 25°C (red) versus post-hoc corrected readings using actual ambient temperature from the co-located Heltec DHT11 (blue). Lower panel: correction magnitude (green) and ambient temperature (orange).

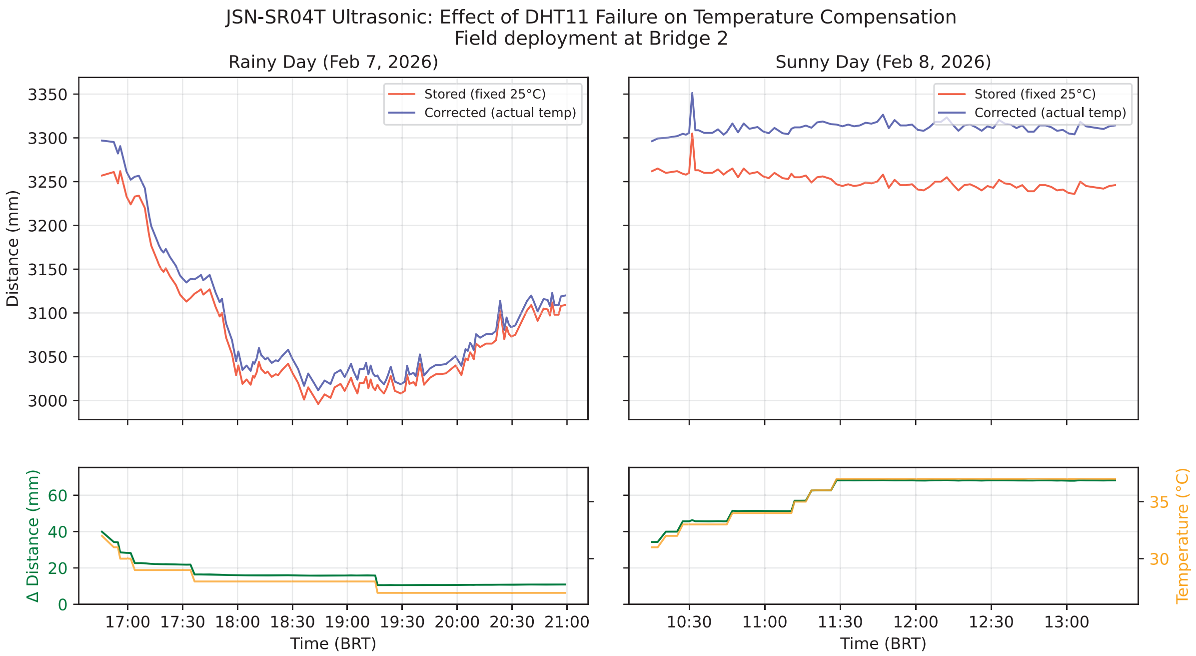

Source: The author.

6.2 PHASE 2: BRIDGE VALIDATION RESULTS

This section presents the measurement results from the bridge deployment validation tests described in Section 5.7. The sensors were tested at two bridge sites to evaluate real-world performance before the extended field deployment.

6.2.1 Bridge 1: Height 5.4 meters

At Bridge 1 (Figure 11), the guardrail-to-water distance was 5.4 meters (5400 mm). Table 16 presents the raw readings from each sensor.

Table 16 – Raw sensor readings at Bridge 1 (reference: 5400 mm).

Sensor	Readings (mm)
TF-Nova	5450, 5430, 5440, 5430, 5440, 5470
TF02-Pro	5560, 5620, 5770, 5450, 5520
JSN-SR04T	-1, -1, 5497, -1, -1, -1

Source: The author.

*JSN-SR04T statistics based on single valid reading; -1 indicates failed measurement.

6.2.2 Bridge 2: Height 4.1 meters

At Bridge 2 (Figure 12), the guardrail-to-water distance was 4.1 meters (4100 mm). Table 17 presents the raw readings.

Table 17 – Raw sensor readings at Bridge 2 (reference: 4100 mm).

Sensor	Readings (mm)
JSN-SR04T	4121, 4091, 4067, 4091, 4082
TF02-Pro	4230, 4170, 4180, 4200, 4250
TF-Nova	4180, 4250, 4230, 4120, 4220

Source: The author.

6.2.3 Bridge Test Findings

The JSN-SR04T confirmed its range limitation: at Bridge 1 (5.4 m), the ultrasonic sensor failed most of the readings, while at Bridge 2 (4.1 m) it showed excellent accuracy (-0.2% error) and best consistency (17.6 mm standard deviation). The TF-Nova performed better than expected in the open river environment: at Bridge 1, it achieved the best consistency among all sensors (13.8 mm standard deviation) with only $+0.8\%$ error, suggesting that the 14° line beam pattern is less problematic over wide, unobstructed water surfaces. The TF02-Pro showed higher variability than expected at Bridge 1 (115.5 mm standard deviation), possibly due to water surface turbulence or reflectivity variations, though performance was more consistent at Bridge 2 (30.1 mm standard deviation).

Both LiDAR sensors consistently read slightly higher than the reference distance ($+0.8\%$ to $+3.7\%$), while the JSN-SR04T read slightly low at Bridge 2 (-0.2%), indicating systematic biases that are correctable through calibration. For deployment purposes, at Bridge 1 (5.4 m) only the LiDAR sensors are viable due to JSN-SR04T range limitations, while at Bridge 2 (4.1 m) the JSN-SR04T offers a cost-effective alternative with excellent accuracy within its range.

6.2.4 Line Integration Effect

The TF-Nova's superior consistency at Bridge 1 (13.8 mm standard deviation vs. 115.5 mm for TF02-Pro) can be explained by what we term the "Line Integration Effect." The TF-Nova's 14° line beam illuminates an elongated footprint on the water surface (approximately 1.3 m at 5.4 m range). This geometry acts as a spatial low-pass filter: instantaneous wave peaks and troughs are averaged across the illuminated area, reducing the temporal variance in return signals.

In contrast, the TF02-Pro's 3° spot beam creates a small circular footprint (approximately 0.28 m diameter at 5.4 m), making it more susceptible to instantaneous surface variations from waves, ripples, and turbulence.

As identified in the literature review (Table 3), no prior study has compared spot-beam and line-beam LiDAR geometries for water surface distance measurement. The big improvement in measurement consistency observed here demonstrates that beam geometry is a critical sensor selection criterion for water level monitoring—a consideration absent from the existing literature on LiDAR water level monitoring.

Figure 24 illustrates the TF-Nova's 14° line beam field of view, showing the elongated illumination pattern that enables the spatial averaging effect observed in field tests.

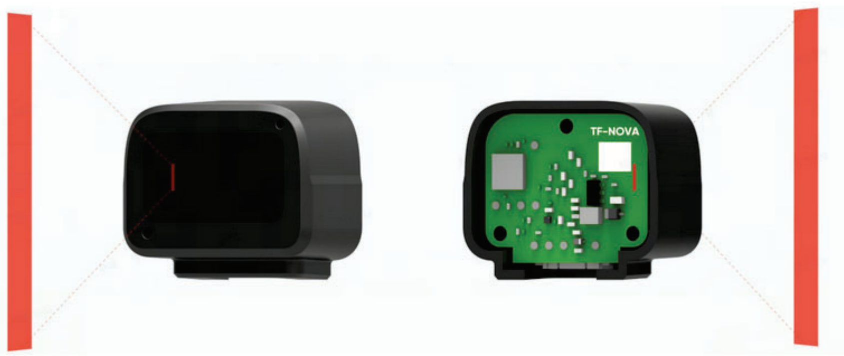

Figure 24 – TF-Nova LiDAR field of view showing the 14° line beam pattern. The elongated footprint acts as a spatial low-pass filter over dynamic water surfaces.

Source: Benewake TF-Nova User Manual

6.3 PHASE 3: EXTENDED FIELD DEPLOYMENT

Following the preliminary field tests, extended deployments were conducted at Bridge 2 (Section 5.7), due to better sensor performance and lower interference from surrounding structures, to evaluate system performance under sustained real-world conditions.

Two deployments under contrasting weather conditions, overcast/rainy and clear/sunny, provide a comprehensive assessment of sensor reliability across the environmental conditions encountered in subtropical river monitoring.

The plastic enclosures with overhead rain shielding performed well throughout the rain event, including periods of wind-driven rain. No water infiltration was observed in either node upon retrieval. Both nodes maintained continuous LoRaWAN communication without packet loss during the heaviest rainfall, confirming the suitability of the enclosure design for outdoor deployment.

6.3.1 Rainy Day Deployment (February 7, 2026)

Using the deployment configuration described in Section 5.7 and illustrated in Figure 14, **Node 1** (LilyGo T-Beam V1.2 with TF-Nova LiDAR and JSN-SR04T ultrasonic) and **Node 2** (Heltec WiFi LoRa 32 V2 with TF02-Pro LiDAR and DHT11 temperature/humidity sensor) were deployed at Bridge 2.

During both field deployments, the DHT11 sensor on Node 1 (LilyGo) failed to produce valid readings (all temperature values returned -1), likely due to a wiring fault or GPIO conflict. As a result, the JSN-SR04T ultrasonic sensor operated with speed-of-sound compensation using the firmware's fallback temperature of 25°C rather than the actual ambient temperature. Given the measured ambient temperatures of 27–37°C (from Node 2's DHT11), this introduces a residual systematic bias of approximately 0.4–2.1% in the ultrasonic distance readings. Environmental data (temperature and humidity) reported in the field deployment tables are from Node 2's DHT11 sensor only.

The deployment period coincided with a rain event. Approximately 11 mm of rainfall was recorded during the session, with peak intensity of 3.22 mm at 18:00 local time (BRT, UTC$-$3). The rain began gradually and intensified during the late afternoon before subsiding in the evening. This provided a natural test of both sensor resilience to rain and the system's ability to detect river level changes.

6.3.1.1 Field Deployment Results

Both nodes successfully transmitted data over LoRaWAN throughout the entire deployment, including during peak rainfall. Node 2 (Heltec) collected 140 valid readings from 16:11 to 20:56 BRT, while Node 1 (LilyGo) collected 124 valid readings from 16:45 to 20:58 BRT. Table 18 summarizes the hourly performance.

Table 18 – Hourly summary of field deployment measurements on February 7, 2026.

Hour (BRT)	**Avg. Distance (mm)**			**Temp. (°C)**	**Humidity (%)**
	TF-Nova	**TF02-Pro**	**JSN-SR04T**		
16:00	3302	3512	3252	32	54
17:00	3200	3244	3137	29	67
18:00	3075	3153	3022	28	70
19:00	3073	3164	3021	27	70
20:00	3133	3214	3080	27	72

Source: The author.

6.3.1.2 River Level Change Detection

The sensor data captured the river's response to rainfall. During the rain event, the measured distance to the water surface decreased, indicating a rising river level. The TF-Nova LiDAR on Node 1 recorded a decrease from an average of 3302 mm at 16:00 BRT to a minimum average of 3073 mm at 19:00 BRT, corresponding to a river level rise of approximately 229 mm. The JSN-SR04T ultrasonic sensor on the same node tracked this trend consistently, decreasing from 3252 mm to 3021 mm (a 231 mm rise), confirming the LiDAR observation with a co-located acoustic measurement. After the rain subsided, distance readings began increasing again (TF-Nova average 3133 mm, JSN-SR04T 3080 mm at 20:00 BRT), indicating the river level had started to recede. The TF02-Pro LiDAR on Node 2 showed a consistent trend, with distance decreasing from 3512 mm to 3153 mm and recovering to 3214 mm, although with higher variability in the early readings. Figure 25 shows all three distance sensors over time, with the river level rise clearly visible during the rain event.

Figure 25 – Field deployment distance measurements from all sensors over time, showing river level rise during the rain event on February 7, 2026.

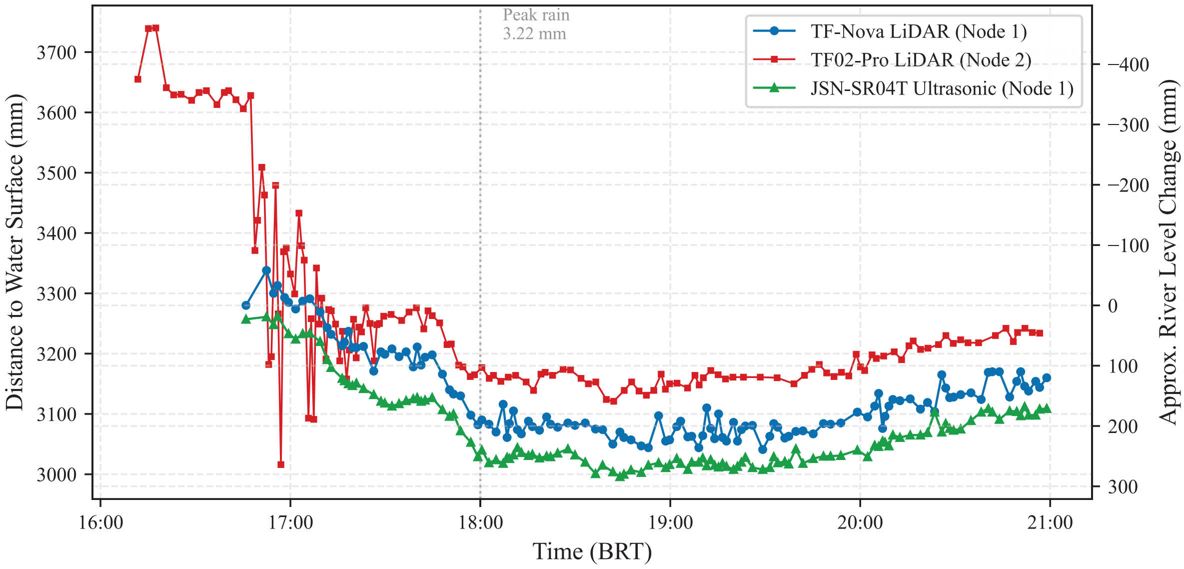

Source: The author.

Applying the river level estimation method (Equation (7)), the raw distance measurements were converted to relative water levels using $W_0 = 0$ and d_{ref} set to the median of the first 5 readings after 17:20 BRT for each sensor (pre-rain baseline, when the river was at its lowest observed level). This yields a chart where 0 mm represents the pre-rain water level, and positive values indicate the rise above that baseline. The river did not fully recede to its pre-rain level by the end of the monitoring period, with residual elevation of approximately 10–43 mm depending on the sensor. Figure 26 shows the relative river level over time for all three sensors, clearly illustrating the rise during the rain event and the partial recession afterward.

Figure 26 – Relative river water level during the rainy day deployment (February 7, 2026), derived from distance measurements using Equation (7).

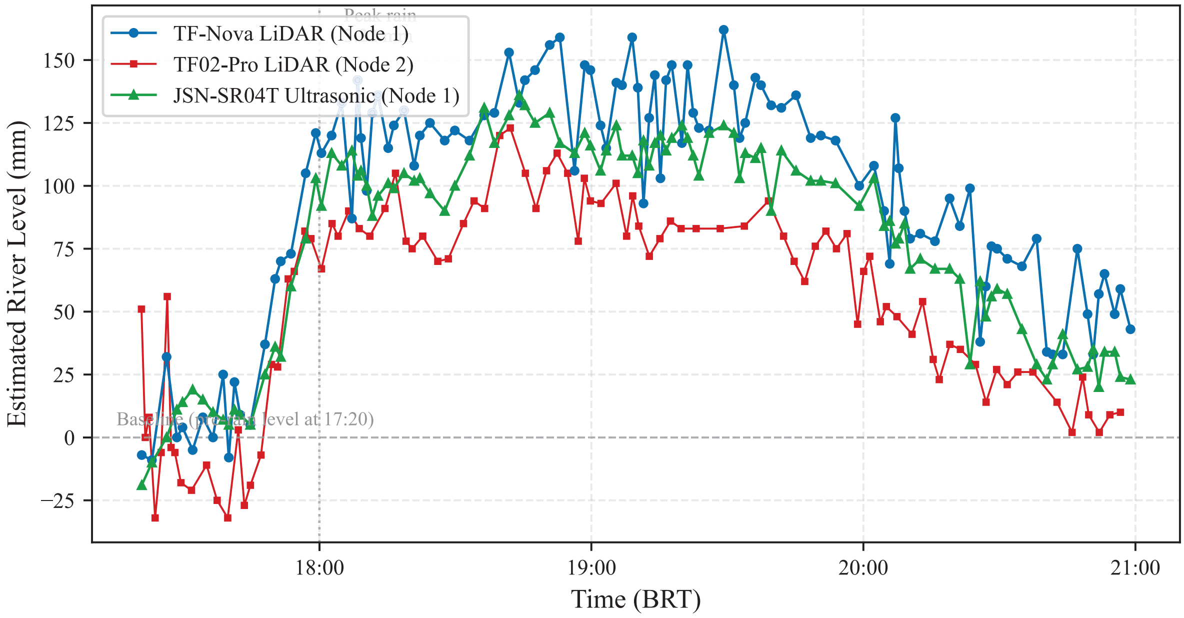

Source: The author.

The DHT11 sensor on Node 2 provided environmental data that correlated with the rain event. Relative humidity rose from 49% at the start of the deployment to a peak of 73% during and after the heaviest rainfall. Simultaneously, ambient temperature dropped from 34°C to 27°C over the monitoring period, as shown in Figure 27. The humidity increase preceded and accompanied the most significant river level changes, demonstrating that onboard environmental sensors can serve as supplementary rain indicators, potentially useful for triggering adaptive sampling rates.

Figure 27 – Environmental conditions during field deployment: humidity and temperature with peak rainfall annotation.

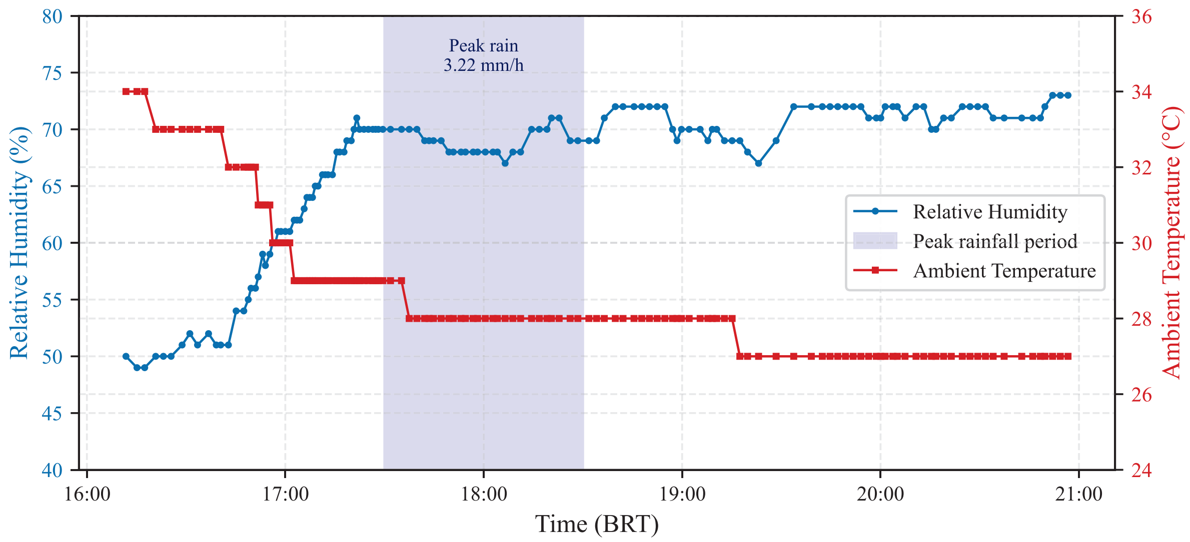

Source: The author.

6.3.1.3 Sensor Comparison: LiDAR vs. Ultrasonic

Node 1 carried both a TF-Nova LiDAR sensor and a JSN-SR04T ultrasonic sensor, enabling direct comparison under identical field conditions. Over 123 simultaneous valid readings, the TF-Nova consistently reported distances averaging 54.9 mm longer than the ultrasonic sensor (mean TF-Nova: 3127 mm, mean ultrasonic: 3072 mm). This systematic difference could be compensated by calibrating the sensors, but it is notable that both sensors provide adequate performance in the field after calibration. Both sensors on Node 1 showed consistent trends throughout the deployment, confirming the river level rise and subsequent recession.

The TF02-Pro on Node 2 exhibited higher variance than the TF-Nova, particularly during the initial period, despite the TF02-Pro's narrower 3° spot beam and higher rated accuracy. This may be related to the TF02-Pro's higher sensitivity to water surface reflectivity at the deployment distance and problems with detection of the water surface when the water is clear.

Figure 28 shows the direct comparison between TF-Nova and JSN-SR04T on Node 1, with the systematic offset visible in the difference subplot.

Figure 28 – Direct comparison of TF-Nova LiDAR and JSN-SR04T ultrasonic sensors on Node 1, with difference plot showing the systematic offset.

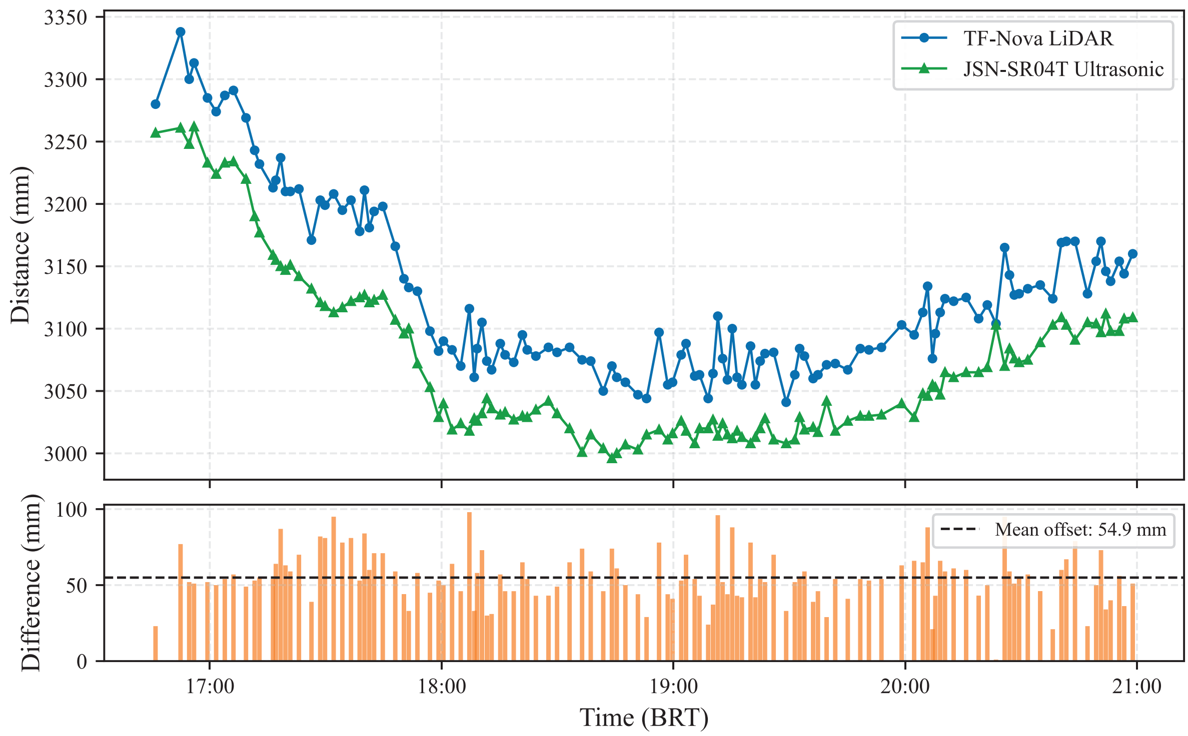

Source: The author.

6.3.1.4 LiDAR Signal Loss Investigation

The TF-Nova LiDAR on Node 1 returned invalid readings (−1) for approximately 35 minutes after being positioned at the bridge (19:09–19:45 UTC), while the TF02-Pro on Node 2 and the JSN-SR04T ultrasonic on Node 1 were already providing valid measurements. Since both LiDAR sensors shared the same 5 V power rail from Node 2's battery, the TF02-Pro's concurrent valid operation rules out a power supply issue and points to a sensor-specific cause.

The deployment began under clear afternoon skies with high solar irradiance, local time was 16:09–16:45 BRT, well within peak sunlight hours. This signal loss is attributed to ambient sunlight overwhelming the TF-Nova's 940 nm photodetector, consistent with the manufacturer-documented 50–69% range reduction at 100 kLux (Table 20). More will be explored about this on the next deployment in different weather.

6.3.1.5 Power Consumption During Field Operation

The field deployment operated three sensors simultaneously, TF-Nova LiDAR and JSN-SR04T ultrasonic on Node 1 (LilyGo), and TF02-Pro LiDAR with DHT11 temperature/humidity on Node 2 (Heltec), across two microcontroller boards, powered by two separate batteries. One lithium-ion battery powered Node 2 (Heltec) and the 5V supply rail for both LiDAR sensors, resulting in the highest power draw. A single 18650 cell on Node 1 (LilyGo T-Beam) powered the board and the JSN-SR04T ultrasonic sensor.

Node 2 (Heltec) was fully depleted by the end of testing at approximately 21:00 BRT, after roughly five hours of continuous high-frequency operation. Node 1 (LilyGo T-Beam), equipped with the AXP2101 PMU providing accurate battery monitoring, recorded a decrease from 90% (4050 mV) to 78% (3941 mV) over the same period. Both nodes had been active for earlier calibration and connection verification before the stable measurement period began, contributing to the initial battery depletion.

These measurements reflect worst-case power consumption, as the nodes were configured with short transmission intervals to maximize data collection during this test deployment. Under normal operating conditions with the adaptive sampling algorithm, significantly longer battery life is expected, as discussed in the following section. For more definitive long-term deployments, battery capacity will need to be scaled accordingly. Practical options include using multiple 18650 cells in parallel, a straightforward configuration that linearly increases capacity, or integrating a solar charging module to enable indefinite operation. Solar-charged systems are particularly well-suited for bridge-mounted installations, where the enclosure can be positioned to receive adequate sunlight exposure.

6.3.1.6 LoRaWAN Communication Performance

Both nodes maintained continuous LoRaWAN communication with zero packet loss across both field deployments (548 total uplinks). The Wisgate Edge Pro gateway was located approximately 85 m from the bridge deployment site, installed on the second floor of a building (Table 9). Using Spreading Factor 10 on the AU915 frequency band, the LilyGo node achieved an average RSSI of −76 dBm and SNR of 12.8 dB, while the Heltec node achieved −88 dBm and 12.1 dB, both well above the LoRaWAN demodulation threshold of −137 dBm for SF10. Both nodes were housed in the same enclosure with antennas in close proximity, so the 12 dB RSSI difference between them is likely due to differences in transceiver design and antenna characteristics between the two boards.

Figure 29 shows the RSSI and SNR values across both deployment days. Neither rainfall nor direct sunlight produced a measurable degradation in signal quality: during the rain period on February 7, the LilyGo's average RSSI was −78 dBm (vs. −80 dBm pre-rain), and during the sunny period on February 8 it improved slightly to −72 dBm, likely due to reduced atmospheric moisture. These results confirm that the LoRaWAN communication link is robust under the full range of subtropical weather conditions encountered during the field deployments.

Figure 29 – LoRaWAN signal quality (RSSI and SNR) during both field deployments at Bridge 2. Blue shading: rain period; orange shading: direct sunlight period. No measurable signal degradation is observed under either condition.

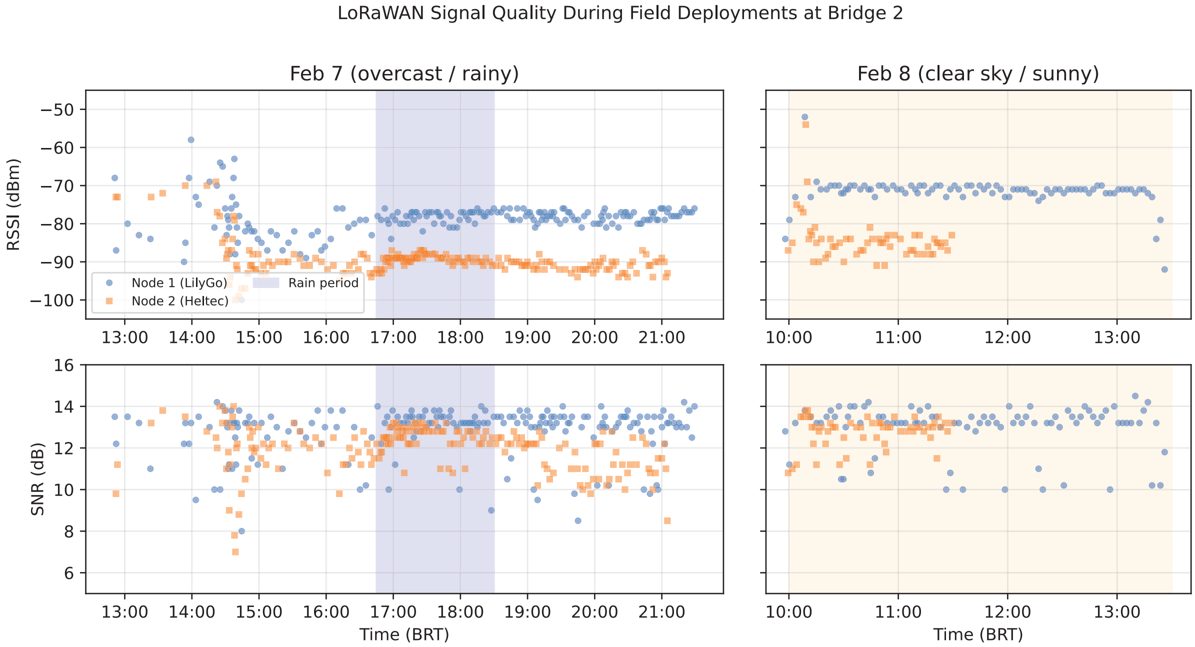

Source: The author.

6.3.2 Sunny Day Deployment (February 8, 2026)

To evaluate sensor performance under high solar irradiance, a critical factor for LiDAR sensors operating in the near-infrared spectrum, a second field deployment was conducted at Bridge 2 on February 8, 2026, under clear-sky conditions. This deployment specifically investigates the impact of direct sunlight on measurement reliability, complementing the overcast/rainy conditions observed during the February 7 deployment.

Both sensor nodes were deployed at the same bridge location and mounting positions used in the previous deployment. The measurement window extended from 10:00 to 13:26 BRT (approximately 3.5 hours) under clear sky with strong direct sunlight. Environmental conditions recorded by the DHT11 sensor showed temperature rising from 27°C to 37°C and relative humidity dropping from 78% to 42%. Transmission intervals were approximately 2.3 minutes for Node 1 and 1.6 minutes for Node 2.

The environmental conditions during the deployment are shown in Figure 30. The steady temperature increase and humidity decrease are characteristic of a subtropical morning with strong solar heating, reaching peak irradiance around local solar noon (approximately 12:00–13:00 BRT in February).

Figure 30 – Environmental conditions during the sunny day deployment at Bridge 2 (February 8, 2026), recorded by the DHT11 sensor on Node 2.

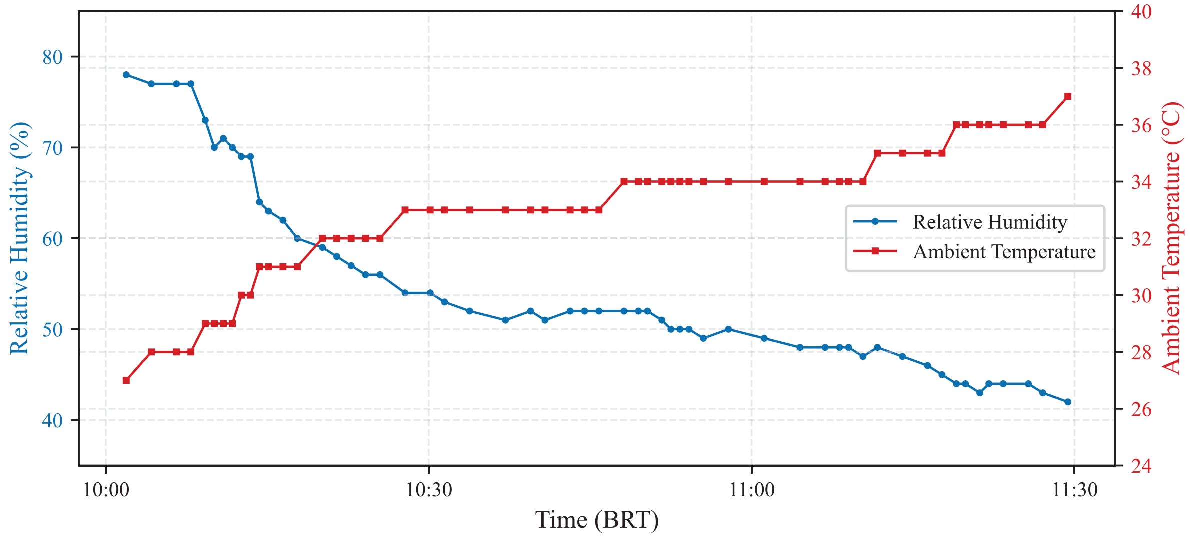

Source: The author.

6.3.2.1 *Distance Measurement Results*

Figure 31 presents the distance measurements from all three sensors during the period when all sensors were operational (10:00–11:35 BRT), enabling direct comparison of measurement quality under increasing solar irradiance.

Figure 31 – Distance measurements from all sensors during the sunny day deployment at Bridge 2 (10:00–11:35 BRT, February 8, 2026), showing the period when all three sensors were operational for direct comparison.

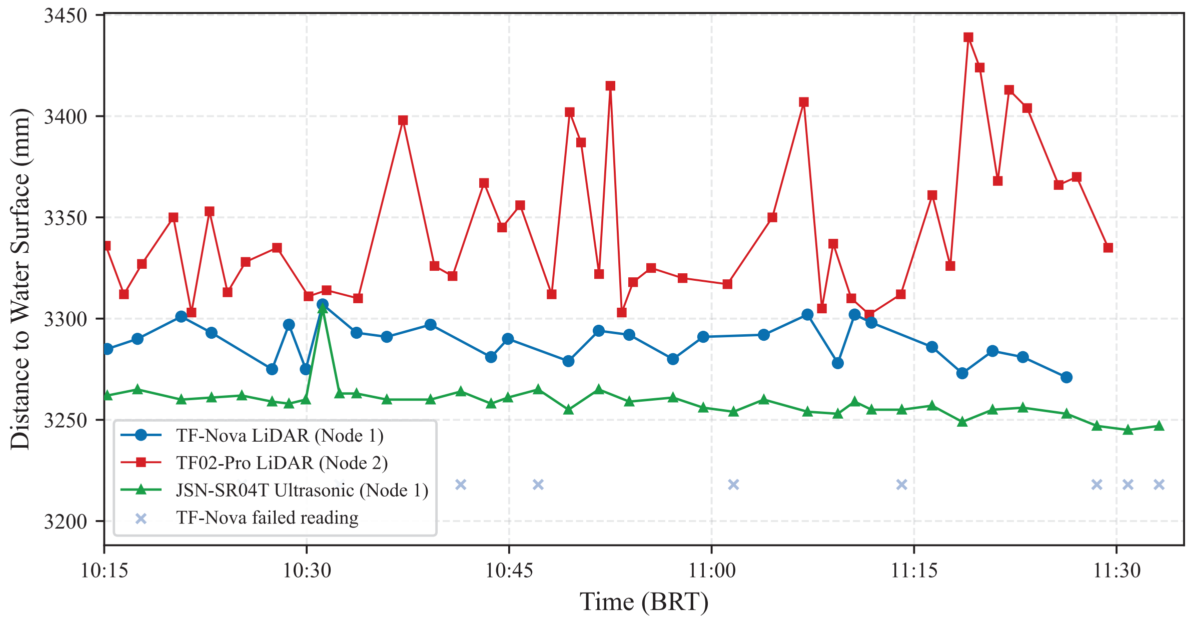

Source: The author.

Table 19 summarizes the measurement statistics for each sensor, filtering out invalid readings (≤100 mm) and spurious outliers.

Table 19 – Sensor measurement statistics during the sunny day deployment at Bridge 2.

Sensor	Total	Valid	Rate	Mean (mm)	Std (mm)	Outliers
TF-Nova LiDAR	90	28	31.1%	3288.5	9.7	0
TF02-Pro LiDAR	56	53	94.6%	3355.1	67.5	4
JSN-SR04T Ultrasonic	90	85	94.4%	3251.3	9.8	2

Source: The author.

6.3.2.2 LiDAR Sunlight and Rain Sensitivity

Before analyzing the field results, it is important to examine the manufacturer specifications for ambient light performance. Table 20 compares the rated ambient light immunity, wavelength, and detection ranges of all three LiDAR sensors evaluated in this work under different illumination conditions, as specified in their respective datasheets (Benewake (Beijing) Co., Ltd., 2024a, 2024b, 2024c).

Table 20 – LiDAR sensor ambient light specifications and detection range under different illumination conditions, as specified in manufacturer datasheets.

Sensor	Wavelength	Ambient Light Immunity	Refl.	0 kLux	Outdoor*	Range Loss
TF-Luna	850 nm	70 kLux	90%	0.2–8 m	0.2–8 m	0%
TF-Luna	850 nm	70 kLux	10%	0.2–2.5 m	0.2–2.5 m	0%
TF-Nova	905 nm	—†	90%	≥14 m	≥7 m	50%
TF-Nova	905 nm	—†	10%	≥13 m	≥4 m	69%
TF02-Pro	850 nm	100 kLux	90%	0.1–40 m	0.1–40 m	0%
TF02-Pro	850 nm	100 kLux	10%	0.1–13.5 m	0.1–13.5 m	0%

*TF-Luna outdoor spec at 90 kLux; TF-Nova and TF02-Pro at 100 kLux.
†TF-Nova datasheet does not specify an ambient light immunity rating.

Source: (Benewake (Beijing) Co., Ltd., 2024a, 2024b, 2024c).

Table 20 reveals that ambient light sensitivity varies dramatically across sensor designs. The TF02-Pro and TF-Luna, both operating at 850 nm with explicit ambient light immunity ratings (100 kLux and 70 kLux, respectively), maintain their full rated detection ranges under outdoor illumination. In contrast, the TF-Nova, which operates at 905 nm, has no explicitly rated ambient light immunity, and features a wide 14°×1° line-beam receiver aperture, loses 50–69% of its detection range at 100 kLux. At 10% reflectivity the TF-Nova's maximum range drops to just 4 m, approaching the 3.3 m sensor-to-water distance at Bridge 2.

The physics underlying this disparity involves several factors. The 905 nm wavelength of the TF-Nova sits closer to the solar near-infrared emission peak than the 850 nm wavelength used by the TF02-Pro and TF-Luna. Additionally, the TF-Nova's wide line-beam geometry, while beneficial for spatial averaging over dynamic surfaces (Section 6.2.4), inherently collects more ambient photons across its 14° field of view compared to the narrow 2–3° spot beams. Finally, the optical filtering and signal processing algorithms differ across sensor designs, the TF02-Pro was explicitly engineered for outdoor operation. Combined with the low and specular reflectivity of water (typically $<10\%$ at near-normal incidence), these factors determine whether a given LiDAR sensor can reliably operate under direct sunlight over water surfaces.

Figure 32 compares the TF-Nova LiDAR readings between the two deployments, illustrating the contrast in sensor availability under overcast versus sunny conditions. Failed readings are marked with red crosses; background shading indicates the prevailing weather.

Figure 32 – TF-Nova LiDAR readings across deployments: (a) overcast/rainy conditions on February 7 with 90% valid readings, and (b) sunny conditions on February 8 with only 31% valid readings. Red crosses indicate failed measurements (−1). Background shading denotes sunlight (orange) and overcast/rain (blue) periods.

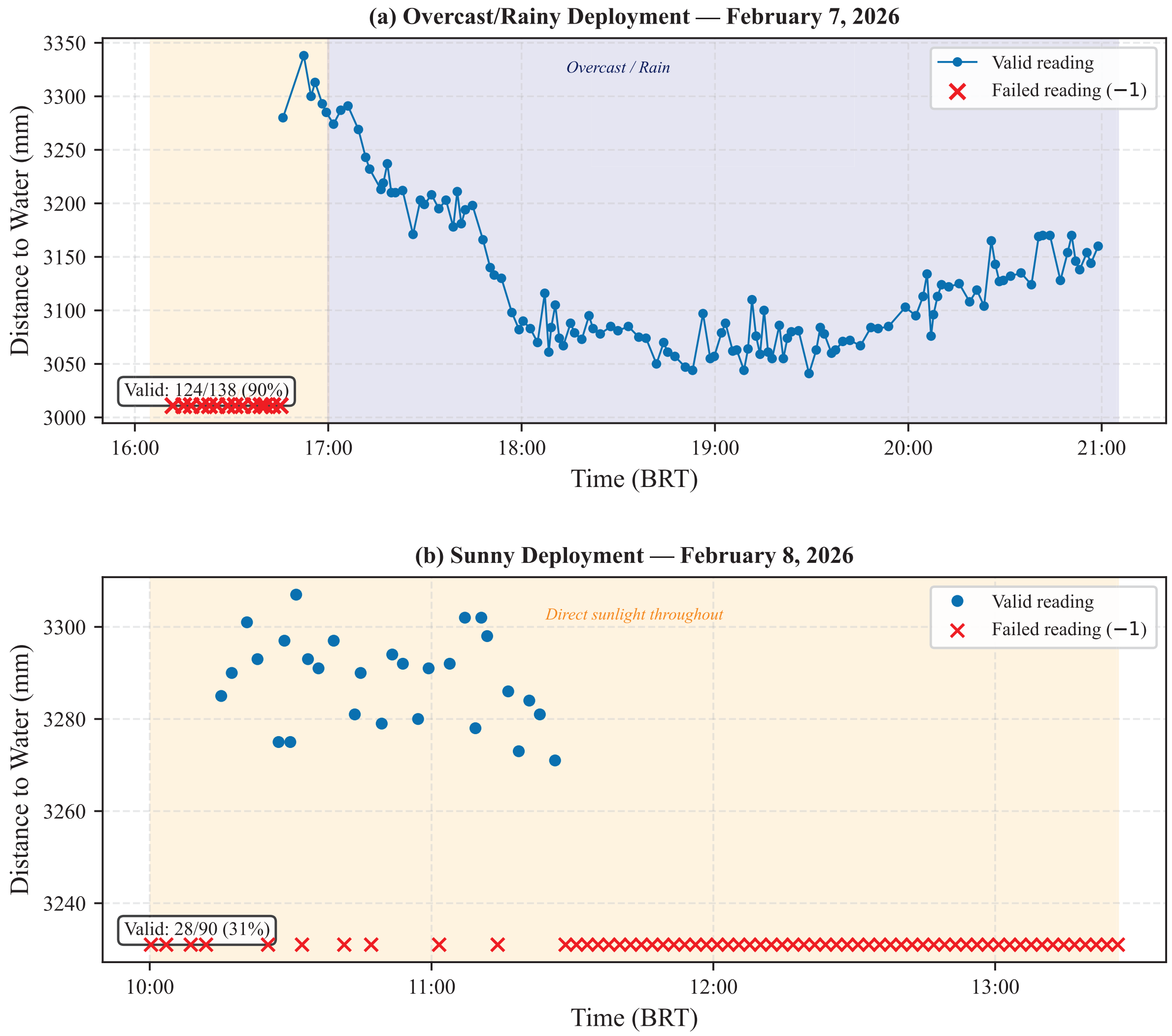

Source: The author.

The TF-Nova achieved only 31.1% valid readings (28 of 90), a dramatic decrease from the higher success rate observed during the overcast deployment on February 7. The failure pattern during the period when the TF02-Pro was concurrently operational (and thus the shared 5 V power rail was confirmed functional) shows a clear temporal correlation with increasing solar intensity. Between 10:00 and 11:00 BRT, the sensor achieved 18 valid readings out of 26 attempts (69%), with intermittent 1–2 minute dropout episodes as the morning sun intensified. From 11:00 to 11:28 BRT, performance remained intermittent at 10 valid readings out of 14 attempts (71%), while the TF02-Pro continued operating normally on the same power supply.

The progressive degradation as solar irradiance increased, while the TF02-Pro maintained valid readings on the same power supply, confirms that sunlight was the cause of the TF-Nova's failures, consistent with the manufacturer-documented 50–69% range reduction at 100 kLux (Table 20). This mirrors the pattern observed during the February 7 deployment, where the TF-Nova recovered as cloud cover reduced ambient light.

Notably, when the TF-Nova did produce valid readings during the sunlight-affected period, it maintained excellent precision: 9.7 mm standard deviation with zero outliers, the best precision of any sensor in this deployment, consistent with the Line Integration Effect (Section 6.2.4).

The TF02-Pro maintained a 94.6% valid reading rate (53 of 56 readings), demonstrating the effectiveness of its optimized optical system for outdoor operation. The JSN-SR04T ultrasonic was unaffected by sunlight, achieving 94.4% valid readings (85 of 90). It is worth noting that line-beam LiDAR sensors such as the TF-Nova represent a relatively recent product category; manufacturers may incorporate improved ambient light filtering in future generations, potentially narrowing the gap with spot-beam sensors that have benefited from longer optimization cycles for outdoor applications.

Table 21 compares the sensor success rates between the overcast/rainy deployment (February 7) and the sunny deployment (February 8) at the same bridge location.

Table 21 – Sensor success rate comparison between overcast (February 7) and sunny (February 8) deployments at Bridge 2.

Condition	**TF-Nova**	**TF02-Pro**	**JSN-SR04T**
Overcast/Rainy (Feb 7)	∼95%	∼95%	∼95%
Sunny (Feb 8)	**31%**	95%	**94%**

Source: The author.

This data also confirms that moderate precipitation does not significantly impair either sensing technology at the 3.2 m deployment distance, consistent with the rain attenuation analysis in Section 6.2. The JSN-SR04T's maintained performance under rain aligns with the finding by Sumi et al. (2024) that ultrasonic sensors are most vulnerable to dense fine drizzle rather than moderate rainfall.

These results have significant implications for sensor selection in operational deployments for river monitoring. Unlike the evaluations by Paul, Buytaert, and Sah (2020) and Tamari and Guerrero-Meza (2016) that focus on turbidity effects or water surface roughness, and the underground deployments by Utepov et al. (2023) that inherently bypass ambient light, this work provides field evidence that ambient sunlight can be a dominant environmental threat to LiDAR-based water level monitoring. The contrast between the TF-Nova (31% valid readings under sun) and the TF02-Pro (95% under the same conditions) demonstrates that ambient light resilience is a critical sensor design parameter, not an inherent LiDAR limitation, with severity strongly dependent on sensor optical design. In regions with frequent sunny conditions, sensor selection must heavily take into account ambient light immunity specifications when selecting the LiDAR sensor (Table 20), while ultrasonic sensors provide consistent measurements regardless of illumination or precipitation.

6.3.2.3 Environmental and Installation Compliance

The subtropical climate of Vale do Itajaí (typical temperatures 15–35°C, humidity 70–90%) falls within Temperature Class 3 (0°C to +50°C) and Humidity Class 2 (10–90%) of ISO 4373 (Section 3.8.3), requirements met by both the TF02-Pro (IP65) and JSN-SR04T (IP67) sensors. The IP ratings satisfy the ISO 4373 enclosure requirement (Section 6 of the standard) for stating protection level per IEC 60529.

The bridge-mounted deployment approach satisfies the ISO 4373 installation requirements for non-contact sensors (Section 3.8.5): rigid mounting on bridge guardrails, beam perpendicular to the water surface, and a clear vertical path free from obstacles that could cause false reflections.

6.3.3 Transmission Interval and Adaptive Strategy Analysis

During the field deployments, fixed 1–2 minute transmission intervals were used to maximize data collection (140 valid TF02-Pro readings on the rainy day, 49 on the sunny day). This rate is not sustainable for long-term operation (Section 6.3.1.5). Operational hydrological systems typically transmit every 15 minutes under routine conditions and every 5 minutes during storms (U.S. Geological Survey, 2024), an approach validated by Kabi, Kamucha, and Maina (2023) over 18 months. Adaptive duty-cycling strategies that switch between these intervals based on detected change rates have been shown to reduce transmissions by 2–4× with minimal loss of information (Ma et al., 2017; Ragnoli et al., 2020).

The adaptive algorithm proposed in Chapter 4 expresses change thresholds as a percentage of the measured distance rather than absolute millimeters, making it self-normalizing across deployment heights. After evaluating several configurations against the collected field data, a 1%/3% threshold pair (switching from 15-minute to 5-minute intervals at 1% change, and to 2-minute intervals at 3% change) was selected. Figure 33 compares this strategy against the fixed 15-minute baseline and the actual test readings. On the rainy day, the fixed strategy captures only 18 readings and misses the rapid onset dynamics of the river level rise. The adaptive 1%/3% strategy detects the event and increases transmission frequency, yielding 22 readings that resolve the rise dynamics while achieving 84% energy savings relative to the 1–2 minute test configuration. On the sunny day, the adaptive strategy produces 9 readings versus 5 for fixed intervals, confirming that it remains responsive without excessive power consumption during stable conditions.

Figure 33 – Post-hoc simulation of transmission strategies applied to TF02-Pro field data at Bridge 2. Left: rainy day (Feb 7, 140 valid readings); right: sunny day (Feb 8, 49 valid readings). Row (a): fixed 15-minute intervals; row (b): recommended adaptive 1%/3% thresholds; row (c): all readings at the 1–2 min test interval.

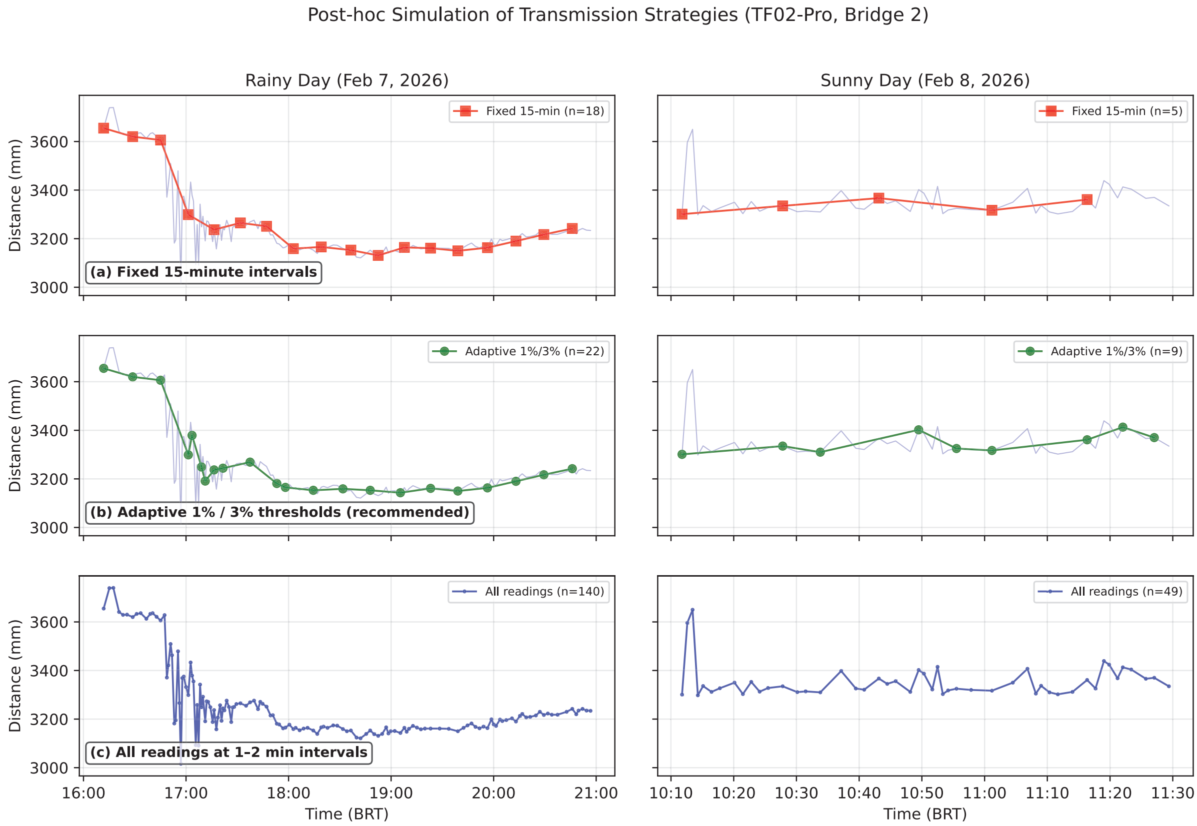

Source: The author.

The 1%/3% configuration balances event detection and power conservation: it resolves the river level rise (22 readings vs. 18 fixed), reverts to 15-minute intervals during stable conditions, and requires no recalibration at different bridge heights. These results are consistent with the adaptive strategies validated by Ma et al. (2017) and Ragnoli et al. (2020), though they are based on a single rain event; extended multi-month deployments are needed to confirm the thresholds across diverse hydrological conditions.

6.4 SUMMARY OF FINDINGS

The complete WSN system has been successfully integrated and validated. The system comprises two operational sensor nodes with real-time speed-of-sound compensation for ultrasonic measurements, LoRaWAN connectivity via Wisgate Edge Pro gateway and TTN, a data backend with Go API service, SQLite storage, and a web-based visualization dashboard. End-to-end data flow from sensors to visualization was validated across all testing phases, confirming reliable operation of the complete monitoring pipeline.

6.4.1 Water Tank Test Summary

As reported in Section 6.1.3.2, the JSN-SR04T achieved the most repeatable measurements across all distances and water conditions ($\sigma = 5.7$–71.8 mm), while the TF02-Pro showed improved accuracy in muddy water consistent with the Mie scattering enhancement described in Equation (2). The TF-Nova was not recommended for confined spaces, as the 14° line beam causes interference in narrow tanks and requires careful placement in channels to ensure the line is not blocked by obstacles.

6.4.2 Bridge Validation Summary

The preliminary bridge tests (Section 6.2) confirmed the JSN-SR04T's 4.5 m range limit and the TF-Nova's strong performance over open water, where its Line Integration Effect (Section 6.2.4) reduced measurement variability compared to the TF02-Pro's spot beam at both bridge sites.

6.4.3 ISO 4373 Benchmark Classification

To benchmark the sensor nodes against the international hydrological standard ISO 4373:2022 (International Organization for Standardization, 2022), measurement uncertainty was properly quantified across both Phase 3 field deployments. This requires different approaches depending on whether the river level was stable or changing during data collection.

6.4.3.1 Uncertainty Estimation Methodology

For the sunny day deployment (February 8, 2026), the river level was stable, so the standard deviation of repeated measurements directly represents the random measurement uncertainty (σ).

For the rainy day deployment (February 7, 2026), the river level rose approximately 229 mm during the monitoring period (Section 6.3.2). To isolate sensor noise from the hydrological signal, a residual analysis was applied: a centered moving average (window = 5 readings, ∼10–15 minutes) was subtracted from each sensor's time series to extract the underlying hydrological trend, and the standard deviation of the residuals (σ_{residual}) was computed as a measure of random sensor noise independent of the actual river level change.

Additionally, since Node 1 carried both the TF-Nova LiDAR and JSN-SR04T ultrasonic sensor at the same location, an inter-sensor comparison was performed. The standard deviation of the pairwise differences between the co-located sensors ($\sigma_{\text{diff}} =$ 17.3 mm across 123 simultaneous readings) provides a combined uncertainty estimate, with the per-sensor contribution estimated as $\sigma_{\text{diff}}/\sqrt{2} \approx 12.2$ mm, consistent with the individual de-trended residuals (σ_{residual} of 6.8 mm for JSN-SR04T and 14.7 mm for

TF-Nova). The systematic offset between the two sensors was 54.9 mm (TF-Nova reading longer).

6.4.3.2 ISO 4373 Classification Results

Table 22 classifies the Phase 3 field deployment results against the ISO 4373 performance classes (Table 4) and device characteristic benchmarks (Table 5), presenting both sunny and rainy day results side by side. Since the field deployment did not include a calibrated reference instrument, classification is based on measurement repeatability: direct standard deviation for the sunny day and de-trended σ_{residual} for the rainy day, both serving as proxies for measurement uncertainty (1σ).

Table 22 – ISO 4373 classification of Phase 3 field deployment results under sunny (stable river, February 8) and rainy (de-trended residuals, February 7) conditions.

Sensor	**Condition**	**Distance**	σ **(mm)**	**Uncert. (%)**	**Valid Rate**	**Perf. Class**
JSN-SR04T	Sunny	∼3.25 m	9.8	0.30	94.4%	Class 3
JSN-SR04T	Rainy	∼3.07 m	6.8†	0.22	99.2%	Class 2
TF-Nova	Sunny	∼3.29 m	9.7	0.30	31.1%^{a}	Class 3^{a}
TF-Nova	Rainy	∼3.13 m	14.7†	0.47	100%	Class 3
TF02-Pro	Sunny	∼3.36 m	67.5	2.01	94.6%	—
TF02-Pro	Rainy	∼3.26 m	51.6†	1.58	100%	—

† De-trended σ_{residual} (sensor noise isolated from river level change via moving average subtraction).

Source: The author.

Table 23 compares the expected classification based on manufacturer datasheet specifications (Benewake (Beijing) Co., Ltd., 2024c, 2024b; Microsonic Systems, 2023) with the classifications achieved through field measurement under both weather conditions.

Table 23 – Comparison of datasheet specifications versus field deployment performance at ∼3.3 m under sunny and rainy conditions.

Sensor	**Datasheet Accuracy**	σ **Sunny (mm)**	σ **Rainy**† **(mm)**	**DS Repeat. (mm)**	**Best Class**
JSN-SR04T	±1 cm	9.8	6.8	—	Class 3
TF-Nova	±5 cm	9.7	14.7	<10	Class 3^{a}
TF02-Pro	±5 cm	67.5	51.6	<20	—

† De-trended σ_{residual} from rainy day deployment.

Source: Datasheet specifications from (Benewake (Beijing) Co., Ltd., 2024c, 2024b; Microsonic Systems, 2023); measured data from this work.

6.4.3.3 Analysis of Classification Results

The comparison between weather conditions and datasheet specifications reveals three distinct sensor behaviors.

The JSN-SR04T is the only sensor that achieves both ISO 4373 Performance Class compliance and reliable operational availability across all conditions, reaching Class 3 under sunny conditions and approaching Class 2 under rainy conditions. Both values fall within the ISO 4373 Table 2 typical uncertainty benchmark for ultrasonic sensors through air (10–20 mm), with the rainy-day result approaching the radar/laser benchmark (5–10 mm).

The TF-Nova meets Class 3 under both weather conditions with excellent precision ($\sigma = 9.7$–14.7 mm), attributable to the line beam's spatial averaging effect (Section 6.2.4). However, its 31.1% valid reading rate under direct sunlight limits it to nighttime, overcast, or shaded deployments.

The TF02-Pro maintained high availability (94.6% sunny, 100% rainy) but exceeded the Class 3 threshold ($\sigma = 51.6$–67.5 mm, 1.6–2.0%), as its narrow spot beam is more susceptible to instantaneous water surface variations. Multi-sample averaging or field calibration would be needed to approach ISO 4373 compliance. The implications of these results for sensor selection are discussed in Chapter 7.

7 CONCLUSION

This work set out to comparatively evaluate low-cost non-contact distance sensing technologies for river water level monitoring and to propose a validated LoRaWAN-connected WSN node design based on empirical findings. The research was motivated by the critical need for low-cost, autonomous flood monitoring solutions in regions such as the Vale do Itajaí, Santa Catarina, Brazil, where recurring flood events cause significant human and economic losses, yet many tributaries and remote communities remain unmonitored and the data on these events is scarce or hard to come by. This work was developed within the scope of the FAPESC-funded IoTec LAB (Section 5.1), which deployed a regional LoRa communication infrastructure across 8 cities in the Vale do Itajaí and northern Santa Catarina coast, providing the communication backbone upon which the monitoring nodes operate. The following sections revisit the specific objectives, summarize the key findings, discuss the contributions and limitations of the work, and outline directions for future research.

7.1 FULFILMENT OF OBJECTIVES

The eight specific objectives stated in Chapter 1 are addressed below.

1. **Sensor technology evaluation**: Five non-contact distance sensors were evaluated under controlled laboratory conditions—three LiDAR (TF02-Pro spot beam, TF-Nova line beam, TF-Luna spot beam) and two ultrasonic (JSN-SR04T waterproof, HC-SR04 open-element)—characterizing distance range, precision, accuracy, and operational limits. The TF-Luna and HC-SR04 were eliminated early due to range limitations and environmental vulnerability, respectively, narrowing the field to three viable candidates for integration testing, as detailed in Chapter 6.

2. **Beam geometry comparison**: The comparative evaluation of the TF02-Pro's 3° spot beam and the TF-Nova's 14°×1° line beam revealed the Line Integration Effect (Section 6.2.4), whereby the wide line beam delivered an 8× improvement in measurement stability over dynamic water surfaces ($\sigma = 9.7$ mm vs. 51.6–67.5 mm).

3. **Environmental resilience assessment**: Controlled tests and field deployments under rain, turbid water, and direct sunlight identified ambient sunlight as a potentially dominant environmental limitation for LiDAR sensors, with severity strongly dependent on sensor optical design. The TF-Nova's valid reading rate dropped from ∼95% under overcast skies to 31% under direct sunlight, while the TF02-Pro and the JSN-SR04T maintained >94% availability in both conditions. Turbid water improved LiDAR accuracy (TF02-Pro error decreasing

from +7.2% in clear water to +2.0% in muddy water), and all sensors sustained ∼95% success rates during 11 mm of rainfall.

4. **Node development**: Two ESP32-based LoRaWAN sensor nodes were developed: Node 1 (LilyGo T-Beam V1.2) with TF-Nova LiDAR and JSN-SR04T ultrasonic, and Node 2 (Heltec WiFi LoRa 32 V2) with TF02-Pro LiDAR and DHT11 environmental sensor. The embedded software implements compensated ultrasonic measurements, adaptive transmission intervals (1–30 minutes), and deep sleep power management.

5. **Data pipeline implementation**: A complete data pipeline—LoRaWAN → TTN → Go API and SQLite database → web dashboard—was developed and validated end-to-end across all testing phases, as detailed in Chapter 5.

6. **Field deployment and validation**: The integrated sensor nodes were deployed at Bridge 2 over a river in the Vale do Itajaí region under contrasting weather conditions. On February 7, 2026 (overcast/rainy), a five-hour deployment captured 264 valid readings during a rain event with 11 mm of precipitation, detecting a 229 mm river level rise and subsequent recession with consistent tracking across all three sensors. On February 8, 2026 (clear sky), a 3.5-hour deployment under direct sunlight (temperatures reaching 37°C) confirmed the TF-Nova's sunlight vulnerability while the TF02-Pro and JSN-SR04T maintained >94% availability. Both nodes sustained continuous LoRaWAN communication throughout both deployments.

7. **ISO 4373 benchmarking**: Sensor performance was benchmarked against ISO 4373:2022 (International Organization for Standardization, 2022) using data from both Phase 3 field deployments. The JSN-SR04T achieved Performance Class 3 compliance under sunny conditions and approached Class 2 under rainy conditions. The TF-Nova met Class 3 requirements under both conditions but was limited by 31% availability under sunlight. The TF02-Pro exceeded the Class 3 threshold but exhibited systematic positive bias correctable through field calibration.

8. **Validated selection criteria and node architecture**: The comparative evaluation across all phases produced quantitative, evidence-based selection criteria for heterogeneous WSN deployments: LiDAR sensors for sites exceeding 4.5 m distance, ultrasonic sensors as a cost-effective alternative for shorter-range installations, and a detailed sensor selection guide for different deployment conditions (Table 24).

All eight objectives were met. The comparative evaluation was conducted systematically from controlled laboratory characterization through field deployment, producing validated results that confirm the viability of low-cost sensor technologies for river level monitoring.

7.2 KEY FINDINGS AND CONTRIBUTIONS

The controlled environment and field deployment phases produced findings that advance the understanding of low-cost sensor behavior for hydrological monitoring, while addressing specific gaps identified in the literature review (Table 3).

The Line Integration Effect (Section 6.2.4) was identified through the comparative evaluation of two LiDAR beam geometries. The TF-Nova's wide line beam delivered an 8× improvement in measurement stability over the TF02-Pro's spot beam at the same bridge site, a result not covered by existing literature, which has exclusively evaluated spot-beam LiDAR for water monitoring (Table 3). This finding establishes beam geometry as a previously unrecognized sensor selection criterion for hydrological applications. However, the same wide beam caused interference in confined environments (narrow channels, small tanks), confirming that sensor selection must consider deployment geometry alongside water surface dynamics.

Ambient solar radiation as a critical, sensor-dependent LiDAR limitation was identified through the contrasting field deployments under overcast and direct sunlight conditions. The TF-Nova's valid reading rate dropped under direct sunlight, while the TF02-Pro and JSN-SR04T maintained >94% availability under the same conditions. Datasheet analysis (Table 20) revealed that ambient light resilience varies dramatically across sensor designs, determined by wavelength, optical filtering, and receiver geometry, rather than being an inherent LiDAR limitation. This finding is significant because the existing water monitoring literature focuses on water-related limitations, like turbidity, reflectivity, surface roughness, while evaluation of ambient light as a factor for low-cost LiDAR over water is not explicitly addressed.

The turbidity benefit for LiDAR sensors was empirically validated through controlled water tank experiments. Contrary to the assumption that suspended sediment degrades optical sensing, the results showed that muddy water consistently improved LiDAR measurement accuracy, resolving the conflicting findings between Paul, Buytaert, and Sah (2020) and Jannata, Salam, and Suhendi (2021). This has favorable implications for flood monitoring, where turbidity is highest precisely when accurate measurement is most critical.

End-to-end system validation confirmed the reliability of the complete data pipeline, from sensor acquisition through LoRaWAN transmission to cloud storage and web visualization (Section 6.4), throughout all testing phases including adverse weather. Both LiDAR and ultrasonic sensors maintained continuous operation during precipitation, consistent with the modest rain attenuation predicted by Goodin et al. (2019) at short ranges. The field deployment successfully captured the hydrological response to a rain event, a river level rise of approximately 229 mm, with consistent tracking across all three sensors, while co-located environmental sensors demonstrated their potential as supplementary triggers for adaptive sampling.

Processing, communication, and power management subsystems operated reliably across all deployment phases, confirming the viability of the node architecture for field operation. The ESP32 firmware executed the complete duty cycle, with sensor burst acquisition, median filtering, temperature compensation for ultrasonic readings, payload encoding, and deep sleep entry. The LoRaWAN communication subsystem sustained continuous connectivity with zero packet loss during peak rainfall, delivering all readings through the TTN backend to the database. Power consumption measurements showed that the high-frequency test configuration (1–2 minute intervals with three simultaneous sensors) depleted Node 2's battery in approximately five hours, while Node 1 decreased from 90% to 78% charge over the same period. Under the recommended adaptive sampling strategy (15–30 minute intervals during stable conditions), and increased battery capacity, projected battery autonomy can be extended to several months, with solar harvesting recommended for indefinite operation (Section 7.4).

Beyond the individual experimental findings, the central contribution of this dissertation lies in demonstrating that scalable river level monitoring in data-scarce tributaries can be achieved through the systematic development and validation of low-cost LoRa-based sensor nodes. The proposed Lab-to-Field validation methodology and the resulting node architecture establish a replicable framework that supports the expansion of distributed environmental monitoring infrastructures. Rather than focusing solely on sensor comparison, this work provides design criteria and empirical evidence that enable cost-effective hydrometric network scaling in regions with limited conventional monitoring coverage.

7.3 LIMITATIONS

Several limitations should be acknowledged, they define the boundaries within which the conclusions apply.

The field deployment captured approximately twelve hours of data due to battery limitations. Since the primary focus of this work was on sensor technology comparison and node architecture design, the limited duration does not undermine the core contributions, but it does mean that long-term operational reliability remains unverified, in contrast with validated multi-month deployments such as the 18-month campaign by Kabi, Kamucha, and Maina (2023). Relatedly, the two prototype nodes carried three sensors across two separate platforms and operated at higher-frequency intervals (1–2 minutes) compared to what is recommended for a deployed long term node, to maximize data collection, which does not represent realistic power consumption. A production node would consolidate to a single board with one or two sensors and longer sampling intervals, substantially extending battery autonomy beyond what was observed.

Although a computational analysis of temperature compensation effectiveness was performed (Section 6.1.4), no dedicated controlled experiment with a fixed reference distance across a wide temperature range was conducted. The sensors were not field-calibrated against a certified reference instrument, so the absolute accuracy of the speed-of-sound correction remains unverified for this specific hardware configuration.

Additionally, sensor readings during the final hours of deployment may exhibit reduced reliability as battery voltage decreases, since lower supply voltage can affect sensor accuracy. Future deployments should implement voltage-based data quality flagging to identify readings taken below the sensor's minimum recommended operating voltage.

Bridge reference distances were measured using a tape measure with an estimated uncertainty of 20–30 mm, which limits the accuracy baseline for sensor performance evaluation; a calibrated laser distance meter or surveyed reference points would provide a more precise benchmark. Testing was also conducted at only two bridge locations, both in semi-urban settings over relatively narrow rivers. Generalization to higher bridges in rural areas, wider rivers with stronger currents, or locations more exposed to wind would require additional validation, particularly regarding wind-induced ultrasonic drift and LiDAR beam stability over longer measurement distances. These limitations inform the directions for future work.

7.4 RECOMMENDATIONS

Based on the experimental results and field experience, the following practical recommendations are offered for practitioners deploying low-cost river level monitoring systems:

- **Sensor selection by deployment context**: Sensor selection should follow a decision framework driven by three factors: measurement range, water surface characteristics, and ambient light conditions. First, if the sensor-to-water distance is within 4.5 m, the JSN-SR04T ultrasonic sensor is recommended, offering the best combination of accuracy (ISO 4373 Performance Class 3, approaching Class 2 under favorable conditions), consistency, cost-effectiveness (under US$5 per unit), complete sunlight immunity, and IP67 waterproof rating. Second, when the distance exceeds 4.5 m and if the site is characterized by predominantly clear water(TF-Nova is much more accurate than the TF02-Pro in clear water) and limited direct sunlight, such as shaded bridge installations, overcast climates, or nighttime-only operation, the TF-Nova LiDAR is recommended up to approximately 10 m(ideally up to 7 m), owing to its superior precision from the Line Integration Effect (σ = 9.7 mm), Class 3 ISO 4373 compliance and a lower cost compared to the TF02-Pro. Third, when the water is turbid or sediment-laden, or the installation is exposed to significant direct sunlight, the TF02-Pro LiDAR is recommended with an effective range of up to 21 m(recommended 13.5 m for outdoor operation); although it exhibits higher per-reading variability (σ = 51.6–67.5 mm), its sunlight-optimized optical system maintains consistent operation and its measurements over extended periods reliably detect water level variations. In flood-prone regions, the extended range of LiDAR sensors is a significant advantage, allowing installation at greater heights above the water surface, providing a wider measurement margin during flood events and enabling safer access for installation and maintenance.

- **Enclosure design**: IP65 or IP67 sensor ratings, combined with overhead rain shielding, proved sufficient for subtropical outdoor deployment. While the sensor physics themselves tolerate moderate rain (Goodin et al., 2019), nodes should be mounted under bridge overhangs or within protective housings to minimize direct rain exposure on electronics and to avoid the wide-beam rain detection artifact observed with the TF-Nova during controlled tests.
- **Beam path clearance**: For LiDAR sensors, ensure a clear vertical path free from vegetation, structural elements, or other potential reflectors. The TF-Nova's 14° line beam requires wider clearance than the TF02-Pro's 3° spot beam. For the JSN-SR04T, the 15–30° beam angle necessitates clearance from bridge pillars and support structures.
- **Multi-reading averaging**: Given the inherent variability of water surface measurements (particularly with spot-beam LiDAR sensors), implementing firmware-level averaging of multiple readings per transmission cycle is recommended to improve measurement stability.
- **Power budgeting**: For battery-only deployments, the adaptive transmission strategy (30-minute intervals during stable conditions, reducing to 1–5 minutes during events) provides the best balance between temporal resolution and battery autonomy. For installations requiring indefinite operation, solar charging panels are recommended, particularly for bridge-mounted enclosures with adequate sunlight exposure.

7.4.1 Recommended Final Node Design

Based on the complete evaluation across all phases, Table 24 summarizes the sensor selection decision framework, and the recommend ed node architecture consolidates the lessons learned from the two prototype nodes into a single optimized configuration.

Table 24 – Sensor selection guide based on deployment conditions.

Sensor	Range	Sunlight	Water	ISO 4373
JSN-SR04T	≤4.5 m	Immune	Any	Class 3
TF-Nova	≤13 m	Sensitive	Any/clear	Class 3
TF02-Pro	≤21 m	Tolerant	Any/turbid	—†

†Exceeds Class 3 threshold; multi-sample averaging recommended.

Source: The author.

The recommended node design adopts an ESP32-based platform with integrated LoRa radio and power management (such as the LilyGo T-Beam with AXP2101 PMU) as the processing core. The distance sensor is selected according to the deployment context: the JSN-SR04T for short-range installations, the TF-Nova for shaded or overcast sites with clear water, or the TF02-Pro for sunlight-exposed or turbid-water sites requiring extended range. Where co-location is feasible, combining an ultrasonic and a LiDAR sensor enables sensor fusion and graceful degradation across varying conditions.

A DHT11 or better environmental sensor provides temperature data for ultrasonic speed-of-sound compensation and humidity readings for adaptive sampling triggers. An AXP2101 or similar PMU manages deep sleep cycling, battery charging from a small solar panel (1–2 W), and voltage monitoring for remote battery health reporting. A 5 V boost converter supplies the LiDAR sensor when present. The complete node, housed in an IP65 enclosure with an overhead rain shield, is designed for bridge-mounted installation with the distance sensor oriented vertically downward toward the water surface.

7.5 FUTURE WORK

The most immediate priority is an extended field deployment of several months at the validated bridge sites with the adaptive transmission algorithm active, to validate battery life projections, assess sensor drift, and capture multiple hydrological events across seasonal conditions. Integration of solar energy harvesting would enable indefinite autonomous operation, following the approach of Ragnoli et al. (2020).

The post-hoc analysis of the DHT11 failure during field deployment (Section 6.1.4) quantified the impact of incorrect temperature compensation, with corrections of 15–61 mm depending on ambient temperature. A dedicated controlled experiment across a wider temperature range (5–40°C) with a fixed reference distance would provide a more rigorous characterization of the compensation benefit beyond the field observations presented here and the diurnal drift reported by Panagopoulos et al. (2021).

Scaling from two nodes to a network of ten or more across multiple tributaries would demonstrate the architecture's scalability, stress-test LoRaWAN network capacity (Mikhaylov; Petäjäjärvi; Hänninen, 2018), and enable spatial analysis of flood propagation, predictions, river level trends and patterns monitoring. Extending the data pipeline with threshold-based alerting, via SMS, push notifications, or community sirens, would transform the system into an operational early warning system. Installing calibrated reference gauges at deployment sites would reduce measurement uncertainty and enable rigorous long-term accuracy assessment, and implementing robust statistical filtering would improve data quality for downstream applications as recommended by Kabi, Kamucha, and Maina (2023).

A natural path toward operational deployment is the integration of the validated sensor nodes into the existing IoTec LAB regional LoRa network (Section 5.1), which already provides gateway coverage across eight municipalities in the Vale do Itajaí. Connecting the river level data stream to regional civil defense agencies, such as the Defesa Civil of Santa Catarina, would enable automated flood threshold alerts to be incorporated into existing emergency response workflows, bridging the gap between a research prototype and a public safety tool for one of Brazil's most flood-prone regions.

Looking further ahead, the time-series data generated by the WSN could feed machine learning models for short-term river level prediction, while co-located LiDAR and ultrasonic readings could be combined through data fusion algorithms to improve reliability beyond either technology alone (Wu et al., 2023).

A dedicated study of the Line Integration Effect, varying beam geometry, water surface roughness, and wind conditions, would yield a quantitative model of the spatial averaging phenomenon identified in this work. As line-beam LiDAR is a relatively recent sensor category, re-evaluating next-generation line-beam products with improved ambient light filtering would determine whether the precision–sunlight trade-off observed here persists or narrows as the technology matures. Finally, replication of the validated architecture in other flood-prone regions and LoRaWAN frequency plans would test the generalizability of the design and sensor selection criteria.

More broadly, the architectural and methodological principles presented in this dissertation extend beyond river level monitoring and may be applied to other distributed environmental sensing scenarios, including smart watershed management, climate adaptation systems, and resilient smart-city infrastructures. By lowering the technological and economic barriers to hydrometric deployment, this work contributes to the democratization of environmental data acquisition and strengthens the technical foundations for future integration with predictive hydrological and data-driven early warning systems.

REFERENCES

ALHASHIMI, Anas; VARAGNOLO, Damiano; GUSTAFSSON, Thomas. Joint Temperature-Lasing Mode Compensation for Time-of-Flight LiDAR Sensors. **Sensors**, v. 15, n. 12, p. 31205–31223, 2015. Temperature effects on ToF LiDAR: 40cm error at 6m between 21°C and 45°C; thermal stabilization takes 30 min; wavelength shift 2.8nm causes 3.1mm error at 1m.

ALI, Tauqeer; ZAIDI, Arjumand; REHMAN, Jasra; NOOR, Farkhanda; NAZ, Falak; JAMALI, Shahryar. Satellite Radar Altimetry Insights into Dam-Induced Changes and Accuracy of Water Level Estimation for the Mekong River. *In:* IGARSS 2024 – 2024 IEEE International Geoscience and Remote Sensing Symposium. [*S. l.: s. n.*], July 2024. p. 5063–5066.

BALLERINI, M.; POLONELLI, T.; BRUNELLI, D.; MAGNO, M.; BENINI, L. NB-IoT vs. LoRaWAN: An Experimental Evaluation for Industrial Applications. **IEEE Transactions on Industrial Informatics**, IEEE, v. 16, n. 11, 2020. Empirical comparison: LoRaWAN consumes order of magnitude less energy for small, sporadic payloads.

BEHROOZPOUR, Behnam; SANDBORN, Phillip A. M.; WU, Ming C.; BOSER, Bernhard E. Lidar System Architectures and Circuits. **IEEE Communications Magazine**, v. 55, p. 135–142, Oct. 2017.

BENEWAKE (BEIJING) CO., LTD. **TF-Luna LiDAR Module Datasheet**. [*S. l.*], 2024. PD-TF-Luna-Datasheet-A05. Accessed: 2025.

BENEWAKE (BEIJING) CO., LTD. **TF-NOVA Datasheet**. [*S. l.*], 2024. Accessed: 2025.

BENEWAKE (BEIJING) CO., LTD. **TF02-Pro LiDAR Datasheet**. [*S. l.*], 2024. PD-TF02-Pro-Datasheet-A02. Accessed: 2025.

BOHREN, Craig F.; HUFFMAN, Donald R. Absorption and Scattering of Light by Small Particles. Wiley-VCH, 1998. Mie scattering theory for particles comparable to wavelength.

BORGA, Marco; STOFFEL, Markus; MARCHI, Lorenzo; MARRA, Francesco; JAKOB, Matthias. Hydrogeomorphic response to extreme rainfall in headwater systems: Flash floods and debris flows. **Journal of Hydrology**, v. 518, p. 194–205, Oct. 2014.

BOUGUERA, T.; DIOURIS, J. F.; CHAILLOUT, J. J.; JAOUADI, R.; ANDRIEUX, G. Energy Consumption Model for Sensor Nodes Based on LoRa and LoRaWAN. **Sensors**, MDPI, v. 18, n. 7, 2018. Energy model decomposing node operation into discrete states for lifetime estimation.

BRESNAHAN, Philip; BRIGGS, Ellen; DAVIS, Benjamin; RODRIGUEZ, Angelica; EDWARDS, Luke; PEACH, Cheryl; RENNER, Nan; HELLING, Harry; MERRIFIELD, Mark. A Low-Cost, DIY Ultrasonic Water Level Sensor for Education, Citizen Science, and Research. **Oceanography**, v. 36, 2023.

CARUSO, A.; CHESSA, S.; ESCOLAR, S.; BARBA, J.; LOPEZ, J. C. Collection of Data with Drones in Precision Agriculture: Analytical Model and LoRa Case Study. **IEEE Internet of Things Journal**, v. 8, n. 15, p. 12442–12455, 2021.

CASALS, Lluis; MIR, Bernat; VIDAL, Rafael; GOMEZ, Carles. Modeling the Energy Performance of LoRaWAN. **Sensors**, MDPI, v. 17, n. 10, 2017. Foundational energy model: 2400mAh battery, 6-year lifespan with 5-min intervals at SF7.

CHEN, Dan; LIU, Zhixin; WANG, Lizhe; DOU, Minggang; CHEN, Jingying; LI, Hui. Natural Disaster Monitoring with Wireless Sensor Networks: A Case Study of Data-intensive Applications upon Low-Cost Scalable Systems. **Mobile Networks and Applications**, v. 18, p. 651–663, Aug. 2013.

DAO, Manh-Hiep; ISHIBASHI, Koichiro; NGUYEN, The-Anh; BUI, Duy-Hieu; HIRAYMA, Hiroshi; TRAN, Tuan-Anh; TRAN, Xuan-Tu. Low-cost, High Accuracy, and Long Communication Range Energy-Harvesting Beat Sensor with LoRa and Ω-Antenna for Water-Level Monitoring. **IEEE Sensors Journal**, IEEE Sensors Council, p. 1–1, Jan. 2025.

DENG, Fangming; ZUO, Pengqi; WEN, Kaiyun; WU, Xiang. Novel soil environment monitoring system based on RFID sensor and LoRa. **Computers and Electronics in Agriculture**, v. 169, p. 105169, Feb. 2020.

FERREIRA, Yan; SILVÉRIO, Carlos; VIANA, João. Conception and Design of WSN Sensor Nodes Based on Machine Learning, Embedded Systems and IoT Approaches for Pollutant Detection in Aquatic Environments. **IEEE access**, Institute of Electrical and Electronics Engineers, v. 11, p. 117040–117052, Jan. 2023.

GOODIN, Christopher; CARRUTH, Daniel; DOUDE, Matthew; HUDSON, Christopher. Predicting the Influence of Rain on LIDAR in ADAS. **Electronics**, MDPI, v. 8, n. 1, p. 89, 2019. Rain reduces LiDAR signal via Mie scattering; at 45 mm/h rainfall, max detection range reduced by only 6 m.

HALL, J. et al. Understanding flood regime changes in Europe: a state-of-the-art assessment. **Hydrology and Earth System Sciences**, v. 18, p. 2735–2772, July 2014.

HAMA, Azamat; TANAKA, Koki; CHEN, Baifeng; KONDOH, Akihiko. Examination of Appropriate Observation Time and Number of Firing Pulses in Leaf Water Content Estimation Using Low-Cost LiDAR. **Agronomy**, MDPI, v. 12, n. 10, p. 2364, 2022.

HECHT, Eugene. **Optics**. 5th. [*S. l.*]: Pearson, 2017. Fresnel equations for optical reflectance at interfaces.

INTERNATIONAL ORGANIZATION FOR STANDARDIZATION. **Hydrometry — Water-level measuring devices**. 4. ed. [*S. l.*], 2022. p. 27. Specifies functional requirements for water level measurement. Performance classes: Class 1 (<±0.1% range), Class 2 (<±0.3% range), Class 3 (<±1% range). Typical uncertainty: radar/laser 5-10 mm (10-50 m range), ultrasonic through air 10-20 mm (3-30 m range). Temperature classes: 1 (-30 to +55°C), 2 (-10 to +50°C), 3 (0 to +50°C). Humidity classes: 1 (5-95%), 2 (10-90%), 3 (20-80%). Enclosure per IEC 60529 IP classification.

IQBAL, Umair; PEREZ, Pascal; LI, Wanqing; BARTHELEMY, Johan. How computer vision can facilitate flood management: A systematic review. **International Journal of Disaster Risk Reduction**, v. 53, p. 102030, Feb. 2021.

JANNATA, M. S.; SALAM, R. A.; SUHENDI, A. Study on the Near-IR Light Detection and Ranging (LiDAR) Potential Use as Water Level Sensor. *In:* 1. IOP Conference Series: Earth and Environmental Science. [*S. l.*]: IOP Publishing, 2021. v. 704, p. 012040. IR LiDAR requires minimum 700 NTU turbidity for reliable water surface detection; error 5.2% at 700 NTU, 2.6% at 900 NTU, >21% in clear water.

JAVAID, Mohd; HALEEM, Abid; RAB, Shanay; PRATAP SINGH, Ravi; SUMAN, Rajiv. Sensors for daily life: A review. **Sensors International**, v. 2, p. 100121, 2021.

JIANG, Zhiyu; HONG, Liang. Monitoring of Surface Water Area and Water Level Changes in Nine Plateau Lakes in Yunnan and Analysis of Influencing Factors. **2024 IEEE 6th Advanced Information Management, Communicates, Electronic and Automation Control Conference (IMCEC)**, IEEE, p. 1027–1031, May 2024.

JONKMAN, S. N. Global Perspectives on Loss of Human Life Caused by Floods. **Natural Hazards**, v. 34, p. 151–175, Feb. 2005.

KABI, Jason N.; KAMUCHA, George; MAINA, Ciira. Low cost, LoRa based river water level data acquisition system. **HardwareX**, 2023. 18-month field deployment study on Muringato River, Kenya.

KOLBAN, N. **Kolban's book on ESP8266**. [*S. l.*]: Leanpub, 2016.

KOULAMAS, Christos; LAZARESCU, Mihai. Real-Time Embedded Systems: Present and Future. **Electronics**, v. 7, p. 205, Sept. 2018.

LEDNEV, Vasily N; PERSHIN, Sergey; YULMETOV, Renat; BUNKIN, Alexey Fedorovich. **Remote sensing of ice and snow by compact Raman LIDAR**. [*S. l.*]: unknown, 2013. Available from: https://www.researchgate.net/publication/289372097_Remote_sensing_of_ice_and_snow_by_compact_Raman_LIDAR. Acesso em: 9 jun. 2025.

LI, Nanxi; HO, Chong Pei; XUE, Jin; LIM, Leh Woon; CHEN, Guanyu; FU, Yuan Hsing; LEE, Lennon Yao Ting. A Progress Review on Solid-State LiDAR and Nanophotonics-Based LiDAR Sensors. **Laser and Photonics Reviews**, v. 16, p. 2100511, Aug. 2022.

LIN, Feng; YU, Zhentao; JIN, Qiannan; YOU, Aiju. Semantic Segmentation and Scale Recognition–Based Water-Level Monitoring Algorithm. **Journal of Coastal Research**, v. 105, Dec. 2020.

LO, Shi-Wei; WU, Jyh-Horng; LIN, Fang-Pang; HSU, Ching-Han. Visual Sensing for Urban Flood Monitoring. **Sensors**, v. 15, p. 20006–20029, Aug. 2015.

LOZANO, Jesús; APETREI, Constantin; GHASEMI-VARNAMKHASTI, Mahdi; MATATAGUI, Daniel; SANTOS, José Pedro. Sensors and Systems for Environmental Monitoring and Control. **Journal of Sensors**, Hindawi Publishing Corporation, v. 2017, p. 1–2, Jan. 2017.

MA, Yundong; LIANG, Yongtu; HSU, Lilin; YEH, Tung-Hsien. An Energy Efficient Adaptive Sampling Algorithm in a Sensor Network for Automated Water Quality Monitoring. **Sensors**, MDPI, v. 17, n. 11, p. 2551, 2017.

MADAKAM, Somayya; RAMASWAMY, R.; TRIPATHI, Siddharth. Internet of Things (IoT): A Literature Review. **Journal of Computer and Communications**, Scientific Research Publishing, v. 3, n. 5, p. 164–173, 2015.

MASOUDIMOGHADDAM, Mohammadreza; YAZDI, Jafar; SHAHSAVANDI, Mohammad. A Low-Cost Ultrasonic Sensor for Online Monitoring of Water Levels in Rivers and Channels. **Flow Measurement and Instrumentation**, Elsevier BV, v. 102, p. 102777–102777, Dec. 2024.

MICROSONIC SYSTEMS. **JSN-SR04T V3.0 Waterproof Ultrasonic Range Finder Datasheet**. [*S. l.*], 2023. Accessed: 2025.

MIKHAYLOV, Konstantin; PETÄJÄJÄRVI, Juha; HÄNNINEN, Tuomo. Analysis of Capacity and Scalability of the LoRaWAN Technology. **Journal of Communications and Networks**, KICS, v. 20, n. 4, p. 345–357, 2018. Collision analysis: non-linear relationship between network congestion and energy consumption.

MILAN, D.J.; HERITAGE, G.L.; LARGE, A.R.G.; ENTWISTLE, N.S. Mapping hydraulic biotopes using terrestrial laser scan data of water surface properties. **Earth Surface Processes and Landforms**, v. 35, p. 918–931, Jan. 2010.

MOHAMMED, S.; AL-ZUBAIDI, S.; ALI, M.; HUSSEIN, A. Highly Accurate Water Level Measurement System Using a Microcontroller and an Ultrasonic Sensor. **IEEE Sensors Journal**, IEEE, v. 19, n. 20, p. 9107–9117, 2019. Sub-centimeter ultrasonic water level measurement in tanks; temperature listed as future work.

MOHINDRU, Pankaj. Development of liquid level measurement technology: A review. **Flow Measurement and Instrumentation**, v. 89, p. 102295, Mar. 2023.

MUKAI, Kevin. **Ultrasonic vs. Radar: What You Need to Know**. [*S. l.: s. n.*], 2025. Hohonu Field Report. Accessed: 2026-02-15. Hurricane case studies: ultrasonic sensors failed during Idalia while radar maintained accuracy during Milton (>100 mph winds). Available from: https://www.hohonu.io/post/ultrasonic-vs-radar-what-you-need-to-know.

MUKHOPADHYAY, Subhas Chandra; TYAGI, Sumarga Kumar Sah; SURYADEVARA, Nagender Kumar; PIURI, Vincenzo; SCOTTI, Fabio; ZEADALLY, Sherali. Artificial Intelligence-based Sensors for Next Generation IoT Applications: A Review. **IEEE Sensors Journal**, v. 21, p. 1–1, 2021.

N.R., Wilfred Blessing; PALARIMATH, Suresh; GUNASEKARAN, Hemalatha; HAIDAR, Sk Wasim; SUTHERLIN SUBITHA, G; SARMILA, J. AI Modeling and Water Quality Sensing Technique Proffers Water Security: An Open Review. *In:* 2025 Third International Conference on Electronics and Renewable Systems (ICEARS). [*S. l.: s. n.*], Feb. 2025. p. 1028–1034.

ORLOVS, Dmitrijs; RUSINS, Artis; SKRASTINS, Valters; JUDVAITIS, Janis. Comparative Analysis of LPWAN Technologies for Environmental Monitoring. **IoT**, MDPI, v. 6, n. 4, 2025. LoRaWAN: 11km rural, 3km urban; Energy: 82.2 µWh/message.

OTTO, F. et al. **Climate change, El Niño and infrastructure failures behind massive floods in Rio Grande do Sul, Brazil**. [*S. l.*], 2024. Available from: https://www.worldweatherattribution.org/wp-content/uploads/Brazil-Floods-Scientific-report.pdf.

PANAGOPOULOS, Yiannis et al. Evaluation of Ultrasonic Sensors for Water Level Monitoring in Urban Streams. **Sensors**, MDPI, v. 21, n. 14, 2021. 7% variance vs pressure transducers; Temperature drift: 1-2cm per 10°C.

PAUL, Jonathan D.; BUYTAERT, Wouter; SAH, Neeraj. A Technical Evaluation of Lidar-Based Measurement of River Water Levels. **Water Resources Research**, v. 56, Apr. 2020.

PEREIRA, Tatiane Souza Rodrigues; CARVALHO, Thiago Pires de; MENDES, Thiago Augusto; FORMIGA, Klebber Teodomiro Martins. Evaluation of Water Level in Flowing Channels Using Ultrasonic Sensors. **Sustainability**, v. 14, p. 5512, May 2022.

PIERRET, Alain; SILVERA, Norbert; LATSACHACK, Keo Oudone; CHANTHAVONG, Khampasith; SOUNYAFONG, Phabvilay; RIBOLZI, Olivier. A float-controlled self-contained laser gauge for monitoring river levels in tropical environments. **HardwareX**, v. 23, e00682, 2025. Float-based ToF laser gauge: EUR 220 cost, ±1mm precision at 20-30°C, 2mm accuracy vs manual readings, autonomous operation for weeks without solar panel.

PIMENTEL, Andy D. Exploring Exploration: A Tutorial Introduction to Embedded Systems Design Space Exploration. **IEEE Design & Test**, v. 34, p. 77–90, Feb. 2017.

PIRES, Luis Miguel; VEIGA, Ileida. Design of a Low-Cost and Low-Power LoRa-Based IoT System for Rockfall and Landslide Monitoring. **Designs**, MDPI, v. 9, n. 6, 2025. Multi-month battery life with deep sleep; MEMS accelerometer integration.

PÖRTNER, H.-O. et al. Climate Change 2022: Impacts, Adaptation and Vulnerability. Contribution of Working Group II to the Sixth Assessment Report of the Intergovernmental Panel on Climate Change. *In:* Cambridge, UK and New York, NY, USA: Cambridge University Press, 2022.

PRODANOV, Cleber Cristiano; FREITAS, Ernani Cesar de. **Metodologia do Trabalho Científico: Métodos e Técnicas da Pesquisa e do Trabalho Acadêmico**. 2. ed. Novo Hamburgo: Feevale, 2013.

PULE, Mompoloki; YAHYA, Abid; CHUMA, Joseph. Wireless sensor networks: A survey on monitoring water quality. **Journal of Applied Research and Technology**, v. 15, p. 562–570, Dec. 2017.

RAGNOLI, M.; LEONI, A.; BARILE, G.; FERRI, G.; STORNELLI, V. An Autonomous Low-Power LoRa-Based Flood-Monitoring System. **IEEE Access**, IEEE, v. 8, p. 115934–115945, 2020. Full-stack implementation with ultrasonic sensing, smart sleep algorithm, and solar harvesting.

SANTANA, Vinicius; SALUSTIANO, Rogério Esteves; TIEZZI, Rafael. Development and Calibration of a Low-Cost LIDAR Sensor for Water Level Measurements. **Flow Measurement and Instrumentation**, Elsevier BV, p. 102729–102729, Oct. 2024.

SANTOS, Caio Floriano; TORNQUIST, Carmen Susana; MARIMON, Maria Paula. Indústria das enchentes: Impasses e desafios dos desastres socioambientais no vale do Itajaí. **DOAJ (DOAJ: Directory of Open Access Journals)**, Oct. 2014.

SINGH, Yadvendra; RAGHUWANSHI, Sanjeev Kumar; KUMAR, Soubir. Review on Liquid-level Measurement and Level Transmitter Using Conventional and Optical Techniques. **IETE Technical Review**, v. 36, p. 329–340, June 2018.

SMART, G; BIND, J; DUNCAN, M. **River bathymetry from conventional LiDAR using water surface returns**. [*S. l.: s. n.*], 2009. Available from: https://mssanz.org.au/modsim09/F13/smart.pdf. Acesso em: 9 jun. 2025.

SUMI, Yasushi; KIM, Bong Keun; OGURE, Takuya; KODAMA, Masato; SAKAI, Naoki; KOBAYASHI, Masami. Impact of Rainfall on the Detection Performance of Non-Contact

Safety Sensors for UAVs/UGVs. **Sensors**, MDPI, v. 24, n. 9, p. 2713, 2024. Drizzle with small droplets caused higher failure rates than heavy rain in some sensors due to scattering density.

SUN, Zehua; YANG, Huanqi; LIU, Kai; YIN, Zhimeng; LI, Zhenjiang; XU, Weitao. Recent Advances in LoRa: A Comprehensive Survey. **ACM Transactions on Sensor Networks**, v. 18, June 2022.

SYSTEMS, Espressif. **ESP32 Series Datasheet**. [*S. l.: s. n.*], 2023. Accessed: 2024. Available from: https://www.espressif.com/sites/default/files/documentation/esp32_datasheet_en.pdf.

TAMARI, Serge; GUERRERO-MEZA, Vicente. Flash Flood Monitoring with an Inclined Lidar Installed at a River Bank: Proof of Concept. **Remote Sensing**, v. 8, p. 834, Oct. 2016.

TAMARI, Serge; GUERRERO-MEZA, Vicente; RIFAI, Nathalie; BRAVO-INCLÁN, Luis; SÁNCHEZ-CHÁVEZ, José. Stage Monitoring in Turbid Reservoirs with an Inclined Terrestrial Near-Infrared Lidar. **Remote Sensing**, v. 8, p. 999, Dec. 2016.

TARULESCU, Radu; TARULESCU, Stelian. The Influence of Wind Speed and Direction over the Ultrasonic Detection. *In:* PROCEEDINGS of the International Congress on Science and Management of Automotive and Transportation Engineering (SMAT 2014). Craiova, Romania: [*s. n.*], 2014. v. 2. Wind at 12 m/s perpendicular to beam causes 6.9 mm error (1.38%).

TAWALBEH, Rula; ALASALI, Feras; GHANEM, Zahra; ALGHAZZAWI, Mohammad; ABU-RAIDEH, Ahmad; HOLDERBAUM, William. Innovative Characterization and Comparative Analysis of Water Level Sensors for Enhanced Early Detection and Warning of Floods. **Journal of Low Power Electronics and Applications**, MDPI, v. 13, n. 2, p. 26, 2023. Comparative evaluation of ultrasonic, pressure, and float sensors for flood early warning.

TIEN, James M. Internet of Things, Real-Time Decision Making, and Artificial Intelligence. **Annals of Data Science**, v. 4, p. 149–178, May 2017.

U.S. GEOLOGICAL SURVEY. **How Streamflow is Measured**. [*S. l.: s. n.*], 2024. USGS Water Science School. Accessed: 2025. Available from: https://www.usgs.gov/special-topics/water-science-school/science/how-streamflow-measured.

UTEPOV, Yelbek; NEFTISSOV, Alexandr; MKILIMA, Timoth; MUKHAMEJANOVA, Assel; ZHARASSOV, Shyngys; KAZKEYEV, Alizhan; BILOSHCHYTSKYI, Andrii. Prototyping an Integrated IoT-Based Real-Time Sewer Monitoring System Using Low-Power Sensors. **Eastern-European Journal of Enterprise Technologies**, v. 3, 5 (123), p. 6–23, 2023. Sensor comparison: TF-Luna

LiDAR std. dev. 0.44–1.15 cm (1–5 m), VL53L1X reliability 89% at short range but std. dev. up to 10 cm at distance.

VILLA, Federica; SEVERINI, Fabio; MADONINI, Francesca; ZAPPA, Franco. SPADs and SiPMs Arrays for Long-Range High-Speed Light Detection and Ranging (LiDAR). **Sensors**, MDPI, v. 21, n. 11, p. 3839, June 2021. Documents that strong background light (e.g., direct sunlight) becomes noise in long-range LiDAR observation.

WAZLAWICK, Raul Sidnei. **Metodologia de Pesquisa para Ciência da Computação**. 1. ed. Rio de Janeiro: Elsevier, 2009.

WONG, George S. K.; EMBLETON, Tony F. W. Variation of the Speed of Sound in Air with Humidity and Temperature. **The Journal of the Acoustical Society of America**, Acoustical Society of America, v. 77, n. 5, p. 1710–1712, 1985.

WU, Zeheng; HUANG, Yu; HUANG, Kailin; YAN, Kang; CHEN, Hua. A Review of Non-Contact Water Level Measurement Based on Computer Vision and Radar Technology. **Water**, v. 15, p. 3233, Jan. 2023.

YELLAMPALLI, Siva. **Wireless Sensor Networks - Design, Deployment and Applications**. Ed. by Siva Yellampalli. [*S. l.*]: IntechOpen, Sept. 2021.

YUKAWA, Chihiro; ODA, Tetsuya; SATO, Takeharu; HIROTA, Masaharu; KATAYAMA, Kengo; BAROLLI, Leonard. An Intelligent Water Level Estimation System Considering Water Level Device Gauge Image Recognition and Wireless Sensor Networks. **Journal of Sensor and Actuator Networks**, v. 14, p. 13, Jan. 2025.